Graz University of Technology

Master Thesis

Carrier Phase-based Ranging for Smart Car Access Systems

conducted at the
Signal Processing and Speech Communications Laboratory
Graz University of Technology, Austria

in co-operation with
NXP Semiconductors Austria GmbH
Gratkorn, Austria

by
Johanna Kerber, MA, 00873120

Supervisors:
Assoc.Prof. Dipl.-Ing. Dr. Klaus Witrisal
Dipl.-Ing. Alexander Venus

Graz, June 21, 2020

Statutory Declaration

I declare that I have authored this thesis independently, that I have not used other than the declared sources/resources, and that I have explicitly marked all material which has been quoted either literally or by content from the used sources.

date	(signature)

Abstract

Modern vehicles are equipped with Passive Keyless Entry & Start Systems (PKES), which enable passive access and the ability to comfortably start the car with the car key in your pocket. While in conventional systems, localization is realized by measuring the field strength of a low-frequency magnetic field, new approaches attempt to estimate the distance between car and key by time-of-flight measurements via high frequency electromagnetic fields.
This thesis aims at evaluating so-called *carrier phase-based ranging*, specifically considering Bluetooth (BT) as a potential radio frequency technology. According to the BT standard, narrow-band signals are sent in the ISM band from 2.402 to 2.480 GHz with their magnitude and phase measured at the receiver. Range estimation methods known from the field of array signal processing are implemented and tested on their applicability, including beamforming algorithms, like the Bartlett and the Capon beamformer, as well as parametric methods, such as the maximum likelihood estimator, the MUSIC algorithm, Root-MUSIC and ESPRIT. These methods are compared in terms of different parameters and channel properties. A reference case with a signal model consisting of only one component (line-of-sight) as well as various multipath scenarios are discussed. Special focus lies in estimating the time-of-flight by a single measurement using *smoothing*.
The evaluation yields significantly more accurate results for parametric methods when multipath propagation is considered, where the limitations of beamforming methods are primarily caused by the low BT bandwidth. The results of the statistical simulation already show high deviations of the beamforming methods for one reflected multipath component at a relatively large distance of more than three meters from the LOS component. Parametric methods, which benefit from exploiting the structure of the covariance matrix, stand out due to *super resolution* and estimate the LOS component almost unaffected by reflections. However, the knowledge of the number of signal components is a relevant condition that is taken into consideration in the last chapter. With the validation of the algorithms using VNA measurements, high deviations are unveiled for parametric methods, when the number of signal components is chosen incorrectly.

Kurzfassung

Moderne Fahrzeuge verfügen über sogenannte Passive Keyless Entry & Start Systems (PKES), welche dem Besitzer passiven Zutritt sowie ein komfortables Starten „mit dem Schlüssel in der Tasche“ ermöglichen. Während Lokalisierung in herkömmlichen Systemen über die Feldstärkemessung eines niederfrequenten Magnetfelds realisiert wird, wird in neuen Ansätzen die Ermittlung der Distanz zwischen Fahrzeug und Schlüssel mithilfe von Laufzeitmessung mittels hochfrequenter elektromagnetischer Felder erwogen.
Das Ziel dieser Arbeit besteht darin, sogenanntes *Carrier phase-based ranging* im Speziellen mittels Bluetooth (BT) zu evaluieren. Dem BT Standard entsprechend werden hierbei schmalbandige Signale in dem BT ISM Band von 2.402 bis 2.480 GHz gesendet und Betrag und Phase am Empfänger ermittelt. Zur Schätzung der Distanz werden verschiedene Array Signal Processing Methoden implementiert und auf Anwendbarkeit getestet, wobei sowohl Beamforming Methoden, wie der Bartlett und der Capon Beamformer, als auch parametrische Methoden, darunter der Maximum Likelihood Schätzer, der MUSIC Algorithmus, Root-MUSIC und ESPRIT, behandelt werden. Diese werden in Hinsicht auf verschiedene Parameter und unterschiedliche Kanaleigenschaften verglichen. Diskutiert werden ein Referenzfall mit nur einer Komponente (LOS) sowie verschiedene Multipath Szenarien. Spezieller Fokus liegt auf der Schätzung der Laufzeit durch nur eine einzelne Messung mithilfe von *Smoothing*.
Die Evaluierung zeigt deutlich präzisere Ergebnisse für parametrische Methoden, sobald Mehrwegausbreitung beachtet wird, wobei sich die Einschränkungen bei den Beamforming Algorithmen vordergründig durch die geringe BT Bandbreite ergeben. Die Ergebnisse der statistischen Simulation demonstrieren hohe Abweichungen der Beamforming Methoden bereits bei einer reflektierenden Signalkomponente in relativ weitem Abstand von über drei Metern zur LOS Komponente. Sogenannte *Super resolution* Methoden weisen durch Miteinbeziehung der Datenstruktur erhebliche Vorteile gegenüber Fourier-basierten Methoden auf, wodurch sie auch bei Reflexionen die LOS Komponente nahezu unbeeinflusst schätzen. Voraussetzung dafür ist jedoch die Kenntnis über die Anzahl der Signalkomponenten, welche im letzten Teil der Arbeit bei der Validierung der Algorithmen mit VNA Messungen thematisiert wird. Hierbei zeigen sich deutliche Abweichungen bei parametrischen Methoden, wenn die Anzahl der Signalkomponenten nicht korrekt geschätzt wird.

Contents

1 Introduction **7**

2 Problem statement **9**
2.1 Concept . . . 9
2.2 Multi-path propagation . . . 11
2.3 Impairments . . . 11

3 Signal Model **12**

4 Estimation methods **16**
4.1 Beamforming techniques . . . 16
4.1.1 The Bartlett beamformer . . . 17
4.1.2 The Capon beamformer . . . 19
4.2 Parametric approaches . . . 20
4.2.1 The MUSIC method . . . 20
4.2.2 Root-MUSIC . . . 22
4.2.3 The ESPRIT method . . . 23
4.2.4 The Maximum Likelihood estimator . . . 25

5 Simulation **27**
5.1 Parameters . . . 27
5.1.1 Basic parameters . . . 27
5.1.2 Signal parameters . . . 28
5.1.3 Grid parameters . . . 29
5.1.4 Additional parameters . . . 29
5.2 Scenario 1 - Single component: Variation of SNR . . . 30
5.2.1 Single realization evaluation . . . 30
5.2.1.1 Characteristic of the Bartlett spectrum . . . 30
5.2.1.2 Characteristic of the Capon spectrum . . . 32
5.2.1.3 Characteristic of the MUSIC pseudospectrum . . . 33
5.2.2 Statistical evaluation . . . 34
5.2.3 Smoothing . . . 36
5.2.4 Properties of Estimates . . . 38
5.2.4.1 Bias . . . 38
5.2.4.2 Variance . . . 39
5.2.4.3 Cramer-Rao lower bound . . . 39
5.2.5 Evaluation of bias and standard deviation . . . 40
5.2.5.1 Performance of Bartlett . . . 42
5.2.5.2 Performance of Capon . . . 43
5.2.5.3 Performance of MUSIC . . . 44
5.2.5.4 ROOT-Music and ESPRIT . . . 45
5.3 Scenario 2 - Two components: Variation of SNR . . . 46
5.3.1 Separation of components in spectrum-forming methods . . . 46
5.3.2 Bias and standard deviation . . . 49
5.3.3 Model order . . . 50
5.3.4 The choice of the smoothing factor . . . 50
5.4 Scenario 3 - Two components: Variation of inter-component distance . . . 53
5.4.1 Evaluation in dependency of $d_{\Delta 12}$ . . . 55

5.5 Scenario 4 - Two components: Variation of the LOS gain . . . 57
5.5.1 The peak searching approach . . . 57
5.5.2 Bias and standard deviation . . . 58
5.5.3 Pertinence of the peak searching approach . . . 60
5.6 Scenario 5 - Diffuse Multipath . . . 62

6 Testing with measurements **65**
6.1 Evaluation using full VNA specifications . . . 66
6.1.1 Positions 1 and 5 . . . 67
6.1.2 Positions 16 and 20 . . . 69
6.1.3 The choice of the model order . . . 71
6.1.4 Estimation error in dependency of the model order . . . 73
6.2 Evaluation using BT specifications . . . 74

7 Conclusion and Outlook **78**

8 Appendix and Bibliography **81**
8.1 Acronyms . . . 81

1 Introduction

Traditionally, remote access to cars was provided by pressing a button on its key fob. While unlocking the car from a distance was omnipresent, a physical key and lock system was still a requirement for the authorization to drive.
Now modern cars offer Passive Keyless Entry and Start (PKES) systems for communication between the users and the car without actively using the key fob. As the name implies, PKES enables the user to access the vehicle completely *passively*, by gaining ranging information between device and car. Based on passive authentication of the corresponding key in a certain range, it assures a comfortable user experience. PKES unlocks when the car owner carries the key and approaches the car, no matter if the key is in his hands or placed in his pocket. While no action from the user is needed, the only requirement is the presence of the key in the communication range of the belonging car. Moreover, PKES also allows starting the car while still having the car keys in a bag or in the pocket.

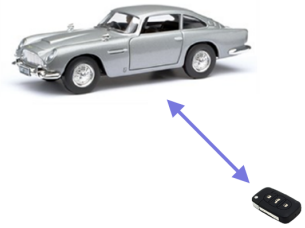

Figure 1.1: A view illustrating the application of carrier phase-based ranging

Beyond doubt PKES systems are highly convenient for the user as searching for the key when approaching the car isn't necessary anymore. Even though it promises an elevated user experience, it is necessary to ensure accurate ranging techniques in order to achieve high functionality. To guarantee safe use, PKES systems must be able to detect the key within regions inside and outside of the vehicle. As a relevant condition, starting the engine is only enabled when locating the key fob inside the car.
To identify the location of the key, conventional systems use a low-frequency magnetic field. The ranging is simply done by measuring the received field strength [1]. The method obtains accurate results, especially benefiting from the fact that environmental factors do not disturb the magnetic field significantly.

Existing systems are nowadays frequently replaced by radio frequency (RF) technologies due to the rise of smart devices and the shift towards smart car access systems. Especially Bluetooth (BT) is considered as a potential RF technology since it its widely available in smart devices. Instead of sending a RF pulse at a fixed frequency and measuring in time domain, BT operates with many different frequencies in the ISM band from 2.402 to 2.480 GHz. The band is divided

into individual channels and allows BT to transmit signals by changing the frequency, a so-called frequency-hopping technique.

While time-based approaches require a large signal bandwidth for gaining correct results in estimation, in this master thesis the so-called carrier phase-based ranging will be discussed, facilitating comparable bandwidth by stacking together single−tone measurements at different channels. More specifically, this thesis aims at implementing and validating different estimation methods known from the field of array signal processing [2], which can leverage the intrinsic structure of the data to achieve *super resolution*, i.e. to be able to obtain a ranging accuracy beyond the Fourier limit.

2

Problem statement

2.1 Concept

Carrier phase-based ranging describes a method to determine the distance between an anchor and a tag from the phase offset of a continuous-wave (CW) signal. The signal is sent by a sender antenna TX and detected by a receiver RX.

The CW signal at the sender $x_s(t, f)$ with phase ϕ is defined as

$$x_s(t, f) = \cos(2\pi f t + \phi). \tag{2.1}$$

The received signal $x_r(t, f)$ after a time delay τ is

$$x_r(t, f) = A x_s(t - \tau, f) \tag{2.2}$$
$$= A\cos(2\pi f(t - \tau) + \phi), \tag{2.3}$$

with a magnitude A, which represents the attenuation of the signal due to the channel (see section 2.3).
Both times, at the sender as well as at the receiver, the phase is estimated by some appropriate method, and we obtain a phase shift θ at the received signal induced by propagation.

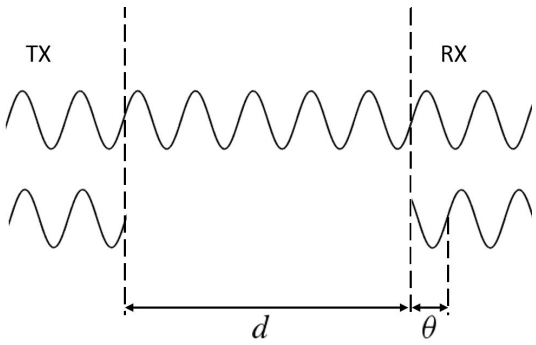

Figure 2.1: A CW signal is sent from TX, inducing a phase shift θ at RX

In principle, the phase shift θ corresponds to the time delay τ, also named time of flight (ToF), as over the relation:

$$\theta = 2\pi f \tau \tag{2.4}$$

We wish to determine the distance d, where

$$d = c\tau\,, \tag{2.5}$$

and c denotes the speed of light.[1]

However, the 2π-periodicity of a CW signal causes the so-called ambiguity problem. As the distance is usually larger than the wave length, we obtain for the measured phase

$$\theta = 2\pi f\frac{d}{c} - 2\pi L\,, \tag{2.6}$$

with L describing the number of waves which fit into the frequency range.
Consequently, a unique solution cannot be obtained as L and d are unknown.

The ambiguity problem can theoretically be solved by measuring the phase at two or more different frequencies f_1 and f_2 (dual-frequency radar [4]).

$$\theta_1 = 2\pi f_1\frac{d}{c} - 2\pi L_1 \tag{2.7}$$

$$\theta_2 = 2\pi f_2\frac{d}{c} - 2\pi L_2 \tag{2.8}$$

Now the phase shift $\Delta\theta$ can be calculated as

$$\Delta\theta = \theta_1 - \theta_2 = 2\pi\Delta f\frac{d}{c} - 2\pi(L_1 - L_2) \tag{2.9}$$

Then, the distance d is proportional to the phase shift $\Delta\theta$ and depends on the frequency step Δf:

$$\begin{aligned} d &= \frac{c}{2\pi\Delta f}\left(\Delta\theta - 2\pi\left(L_1 - L_2\right)\right) \\ d &= \frac{c}{2\pi\Delta f}\Delta\theta - \frac{c}{\Delta f}\left(L_1 - L_2\right) \end{aligned} \tag{2.10}$$

However, as can be obtained from equation 2.10, this approach only works under the condition that Δf is small enough, meaning that $L_1 = L_2$, which leads to

$$d = \frac{c}{2\pi\Delta f}\Delta\theta \tag{2.11}$$

Considering the BT protocol, we operate in a frequency range from 2.402 to 2.480 GHz, so that, regarding to the dual-frequency method, we receive the maximum unambiguous distance d_{max} by inserting $\Delta\phi = 2\pi$

$$d_{max} = \frac{c}{\Delta f}\,, \tag{2.12}$$

[1] Note that for the case of two-way ranging d is defined as $d = c\tau/2$.
While one-way ranging uses synchronized clocks in the initiator and the target, two-way ranging avoids the need of clock synchronization [3]. For two-way ranging, the signal is reflected by the tag and sent back to the transmitter, with the phase measured at the initiator instead.

thus for $\Delta f = f_{max} - f_{min} = 78MHz$ the ambiguity occurs at a distance $d_{max} = 3.84m$, which is practically not useable. Reducing the frequency range enlarges d_{max} but also reduces the temporal resolution, which is already critically low with respect to the problem at hand.

2.2 Multi-path propagation

In contrast to the ideal system described in the previous chapter, in real propagation channels we have to deal with *multi-path propagation*. This is, the receiver does not only measure the direct signal but also reflections caused by the environment, hence not only the Line-of-sight (LOS), but a certain number of multi-path components are sensed at the receiver antenna. Thus, in real channels, reducing the frequency range does not only impair the robustness against noise, but also increases the effect of multi path onto the estimate.

A solution to gain a sufficiently small Δf and to enable unbiased results through carrier phase-based ranging, is to determine the distance d by providing measurements at K frequencies across the Bluetooth 2.4 GHz ISM band.

2.3 Impairments

In a real system, several influences can make it rather difficult to determine the time of flight accurately.
The estimation result can be affected by various factors stated below:

- Multi-path propagation
- Diffraction
- Attenuation
- Scattering
- Noise

As mentioned before, we have to face multi-path propagation.
Considering the impact of reflective components, we deal with multi-path components which are summed up in the signal model which will be introduced in section 3. Hence the environmental situation has a high impact on the estimation.

Additionally, diffraction, attenuation and scattering [5, Ch. 2] can hinder the accurate detection of the LOS.
Considering attenuation, it is often the user himself who might influence the sent signal. For instance, *backpocketing* describes the case when the user has his key in the back pocket of his jeans. Thus the gain of the direct signal is reduced by the influence of the human body, for what reason it is often called a *human body effect*.

To conclude, it is indeed reasonable to consider range estimation methods which exploit the intrinsic structure of the data and thus achieve super resolution. In this thesis various algorithms for estimation are implemented and discussed. The aim is to compare limitations and advantages of the considered methods and thereby evaluate their suitability.

3 Signal Model

At first we only consider a single signal component. The time delayed receiver signal with a magnitude A and phase ϕ can be defined according to section 2.1 as

$$x_r(t,f) = A\cos\left(2\pi f\left(t-\tau\right)+\phi\right) \tag{3.1}$$

Again the time delay τ corresponds to the desired distance d by the relation $\tau = d/c$.

We can convert $x_r(t,f)$ to its complex baseband representation, knowing that any bandpass signal $x_b(t)$ with carrier frequency f_0 can be expressed as

$$\begin{aligned} x_b(t) &= \mathrm{Re}\left[\left(x_p(t)+jx_q(t)\right)\left(\cos 2\pi f_0 t + j\sin 2\pi f_0 t\right)\right] &(3.2)\\ &= \mathrm{Re}\left[x_c(t)\,\mathrm{e}^{j2\pi f_0 t}\right] &(3.3)\end{aligned}$$

where

$$x_c(t) = x_p(t) + jx_q(t) \tag{3.4}$$

is called the complex envelope of the original bandpass signal

$$x_b(t) = x_p(t)\cos 2\pi f_0 t - jx_q(t)\sin 2\pi f_0 t. \tag{3.5}$$

Considering the unmodulated carrier signal $x_r(t,f)$ in (3.1) with $f_0 = f$, we view the constant and time-invariant complex baseband representation $x_{r,\mathrm{CBB}}(f)$ of $x_r(t,f)$ as

$$x_{r,\mathrm{CBB}}(f) = A\mathrm{e}^{j(2\pi f\tau+\phi)} = \alpha\mathrm{e}^{j2\pi f\tau} \qquad \text{with} \quad \alpha = A\mathrm{e}^{j\phi}, \tag{3.6}$$

and we name $x_{r,\mathrm{CBB}}(f)$ the *single-component signal model*.

Operating with the complex baseband representation of a signal convinces by its simplicity for modulation and communication signal processing. The spectrum of a bandpass signals is supposed to be bandlimited around a carrier frequency f_0, and even though in realistic conditions, strictly bandlimited signals do not exist, bandpass signals benefit from very low energy outside a band of bandwidth B_0 [6, p. 696-699].
Taking into consideration the bandpass characteristics, one can observe that the information of a transmitted signal is not contained in the carrier frequency itself, but the modulation on the carrier contains the required information. To gain the complex baseband representation of a signal we map its frequency content from $[f_0 - B_0/2, f_0 + B_0/2]$ to $[-B_0/2, +B_0/2]$. The resulting spectrum is then bandlimited around zero and, as indicated by the name, complex.

For multi-path propagation, we consider M multi path components (MPCs). We describe the

impulse response of linear time-invariant channel as

$$h(t) = \sum_{m=1}^{M} \alpha_m \delta(t - \tau_m) \tag{3.7}$$

with τ_m being the M time delays of interest and

$$\alpha_m = A_m \mathrm{e}^{j\phi_m} \tag{3.8}$$

Thus, each signal component is sensed at the receiver antenna with the corresponding time delay τ_m and complex gain α_m. The signal model can now be defined as the convolution of the impulse response $h(t)$ with the shape of the sent pulse (2.1) as

$$x_{r,\mathrm{M,\ CBB}}(f) = \sum_{m=1}^{M} \alpha_m \mathrm{e}^{-j2\pi f \tau_m} \tag{3.9}$$

To be more precise, we effectively wish to detect τ_1, standing for the LOS component, which is the first signal component detected at the receiver.

Furthermore, we can write

$$\begin{aligned} x_{r,\mathrm{M,\ CBB}}(f) &= \sum_{m=1}^{M} \alpha_m \mathrm{e}^{-j2\pi f \tau_m} \\ &= \boldsymbol{b}(\boldsymbol{\tau})^{\mathrm{T}} \boldsymbol{s} \end{aligned} \tag{3.10}$$

and define $\boldsymbol{b}(\boldsymbol{\tau})$ as a multi-path vector as

$$\boldsymbol{b}(\boldsymbol{\tau}) = \left[\mathrm{e}^{-j2\pi\tau f \tau_1} \quad \mathrm{e}^{-j2\pi f \tau_2} \quad \dots \quad \mathrm{e}^{-j2\pi f \tau_M}\right]^{\mathrm{T}}, \tag{3.11}$$

with

$$\boldsymbol{\tau} = [\tau_1 \quad \dots \quad \tau_M]^{\mathrm{T}}. \tag{3.12}$$

In contrast, we call $\boldsymbol{s}$ the gain vector, containing the complex gains α_m of each signal component

$$\boldsymbol{s} = [\alpha_1 \quad \dots \quad \alpha_M]^{\mathrm{T}} \tag{3.13}$$

Furthermore, from now on we discretize our signal model and define f to be uniformly sampled at multiple frequencies

$$\boldsymbol{f} = \left[\left(-\frac{K}{2}\right)\Delta f \quad \left(-\frac{K}{2}+1\right)\Delta f \quad \dots \quad \left(\frac{K}{2}-1\right)\Delta f\right]^{\mathrm{T}}, \tag{3.14}$$

with

$$\Delta f = \frac{B_0}{K-1}. \tag{3.15}$$

The measurement frequencies correspond to CW signals sensed at the receiver and conform to pulse-like measurements in the frequency domain. The pulses in the frequency domain add up to a rectangular spectrum, as shown in figure 3.1.

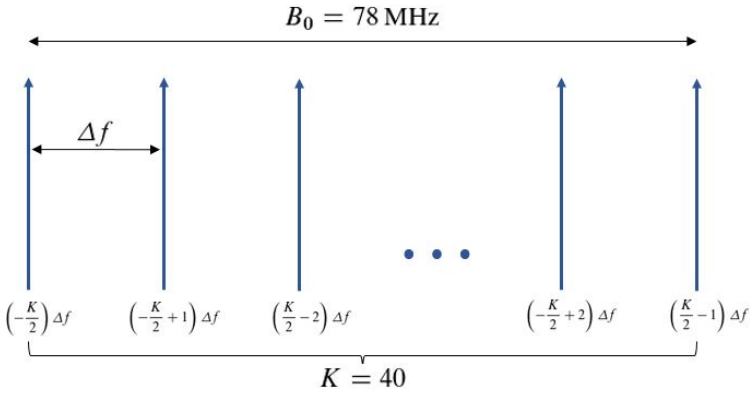

Figure 3.1: K frequencies span a rectangular shaped spectrum in the frequency domain

Taking into consideration that we operate with a number of K measurement frequencies $\boldsymbol{f}$, we form a matrix of dimension $K \times M$:

$$\boldsymbol{B}(\boldsymbol{\tau}) = \begin{bmatrix} \mathrm{e}^{-j2\pi\left(-\frac{K}{2}\right)\Delta f\tau_1} & \mathrm{e}^{-j2\pi\left(-\frac{K}{2}\right)\Delta f\tau_2} & \dots & \mathrm{e}^{-j2\pi\left(-\frac{K}{2}\right)\Delta f\tau_M} \\ \mathrm{e}^{-j2\pi\left(-\frac{K}{2}+1\right)\Delta f\tau_1} & \mathrm{e}^{-j2\pi\left(-\frac{K}{2}+1\right)\Delta f\tau_2} & \dots & \mathrm{e}^{-j2\pi\left(-\frac{K}{2}+1\right)\Delta f\tau_M} \\ \vdots & \ddots & \ddots & \vdots \\ \mathrm{e}^{-j2\pi\left(\frac{K}{2}-1\right)\Delta f\tau_1} & \mathrm{e}^{-j2\pi\left(\frac{K}{2}-1\right)\Delta f\tau_2} & \dots & \mathrm{e}^{-j2\pi\left(\frac{K}{2}-1\right)\Delta f\tau_M} \end{bmatrix} \tag{3.16}$$

$$= \begin{bmatrix} \boldsymbol{b}(\tau_1) & \boldsymbol{b}(\tau_2) & \dots & \boldsymbol{b}(\tau_M) \end{bmatrix} \tag{3.17}$$

with the response vector $\boldsymbol{b}(\tau)$

$$\boldsymbol{b}(\tau) = \begin{bmatrix} \mathrm{e}^{-j2\pi\left(-\frac{K}{2}\right)\Delta f\tau} & \mathrm{e}^{-j2\pi\left(-\frac{K}{2}+1\right)\Delta f\tau} & \dots & \mathrm{e}^{-j2\pi\left(\frac{K}{2}-1\right)\Delta f\tau} \end{bmatrix}^{\mathrm{T}} \tag{3.18}$$

where $\tau \in \{\tau_1, \dots, \tau_M\}$ in (3.18). Note that the response vector $\boldsymbol{b}(\tau)$ expands over different frequencies $\boldsymbol{f}$ and is not equal to the multi-path vector $\boldsymbol{b}(\boldsymbol{\tau})$ defined in (3.11).

We can now define $x_{r,\mathrm{M,\ CBB}}(f)$ to be our signal vector $\boldsymbol{x}_{\mathrm{sig}}$ and write

$$\boldsymbol{x}_{\mathrm{sig}} = \boldsymbol{B}(\boldsymbol{\tau})\,\boldsymbol{s} \tag{3.19}$$

with $\boldsymbol{x}_{\mathrm{sig}}$ having dimension $K \times 1$.

Finally, considering the presence of noise in the signal model, we obtain the vector $\boldsymbol{x}$, containing both signal and noise information, as

$$\boldsymbol{x} = \boldsymbol{x}_{\mathrm{sig}} + \boldsymbol{n}, \tag{3.20}$$

where $\boldsymbol{n}$ is defined to be additive white circular-symmetric complex Gaussian noise (AWCGN) [7, p. 517] with variance $\sigma^2\boldsymbol{I}$ and its specified characteristic to be zero-mean

$$\boldsymbol{n} \sim \mathcal{CN}\left(\boldsymbol{0}, \sigma^2\boldsymbol{I}\right) \tag{3.21}$$

Additionally the variance σ^2 can be defined using the *input* Signal-To-Noise Ratio in dB (further referred to as SNR) as

$$\sigma^2 = \frac{|\alpha_1|^2}{10^{\frac{\mathrm{SNR}}{10}}} \tag{3.22}$$

Note that the SNR is defined as the ratio of the equivalent discrete energy sent from the sender antenna E_{SD} to the power of discretized noise P_{ND}, neglecting any influences of the channel.This means, that reflections are not considered in the signal energy.
The reason is that reflections come from the environment and are part of the channel characteristic. In our case, the channel shall not be part of the Signal-To-Noise Ratio (SNR) definition. For describing the SNR, only the energy of the sender signal with gain α_1 and the noise power P_{ND} are considered.

$$\mathrm{SNR} = \frac{E_{\mathrm{SD}}}{P_{\mathrm{ND}}} \tag{3.23}$$

$$= \frac{|\alpha_1|^2 \|\boldsymbol{b}(\tau)\|^2 \frac{1}{K}}{\frac{1}{N}\mathbb{E}\left[\|\boldsymbol{n}\|^2\right]} \qquad \text{with} \quad \|\boldsymbol{b}(\tau)\|^2 = \sum 1 = K \tag{3.24}$$

$$= \frac{|\alpha_1|^2}{\sigma^2} \tag{3.25}$$

Lastly, the *complete signal model* can be simply written as

$$\boldsymbol{x} = \boldsymbol{B}\left(\boldsymbol{\tau}\right)\boldsymbol{s} + \boldsymbol{n} \tag{3.26}$$

4 Estimation methods

In this chapter we introduce the estimation methods to be evaluated in this thesis.
In general, estimation methods are classified into two main categories: spectral-based approaches and parametric approaches.
Spectral-based estimation methods proceed by forming a spectrum-like function of the parameter of interest. Thus spectral-based approaches also require a reasonable interpretation of the obtained spectrum.
In our case, the spectrum is a function of the time delay τ, defined to be our parameter of interest. By multiplication with the speed of light c we can further look at a spectrum as a function of the desired distance. In the obtained spectrum the highest peak indicates the position of the most output power. Therefore, its position usually is treated to be the estimate of the parameter of interest. Further occurring peaks of the spectrum usually correspond to signals sensed at other distances, like reflections. Nevertheless, since in practical situations the direct signal can be attenuated, the true distance does not necessarily correspond to the maximum peak in our case. This makes *peak searching* another important issue to consider, and it will be addressed in section 5.5.
In contrast to spectral-based methods, parametric approaches do not operate with a spectrum but instead estimate the parameter of interest by making assumptions on the signal model. The basic idea is to consider a model with its functional form based on certain assumptions and estimate the time delay τ in the assumed model.
The remaining section is organized as follows. First, deal with spectral-based approaches and discuss two rather popular beamforming techniques, the Bartlett beamformer and the Capon beamformer. Second, we have a closer look at parametric approaches.

4.1 Beamforming techniques

The basic idea of beamforming techniques is to maximize the output power of a linear combination of the input signal. The estimate is obtained as the time delay which leads to the maximum output power.
In classical literature [2], the signal is obtained spatially, using a sensor array, i.e. a certain number of receiving antennas which sample the space. For distance estimation, the method is adopted from the spatial filtering approach to a temporally obtained signal.

To maximize the output power, we wish to define a temporal filter, which allows a signal with delay τ to pass undistorted. At the same time the filter also minimizes the power of the remaining interference.

The output of this temporal filter is described as

$$\boldsymbol{y}(\boldsymbol{f}, \boldsymbol{w}) = \boldsymbol{w}^{\mathrm{H}} \boldsymbol{x} \tag{4.1}$$

where $\boldsymbol{w}$ is the so-called *weight vector*, which is defined to solve the declared optimization problem.
Further the output power of the filter is

$$P(\boldsymbol{w}) = \mathbb{E}\left[|\boldsymbol{y}(\boldsymbol{f}, \boldsymbol{w})|^2\right] = \boldsymbol{w}^{\mathrm{H}} \boldsymbol{R} \boldsymbol{w} \tag{4.2}$$

The covariance matrix $\boldsymbol{R}$ of $\boldsymbol{x}$ is determined from the data input vector $\boldsymbol{x}$ as

$$\boldsymbol{R} = \mathbb{E}\left[\boldsymbol{x}\boldsymbol{x}^{\mathrm{H}}\right] \tag{4.3}$$

While $\boldsymbol{R}$ contains the information of the sensed signal, the weight vector $\boldsymbol{w}$ describes the desired filter. The choice of the weighting vector $\boldsymbol{w}$ depends on the beamforming technique used.

4.1.1 The Bartlett beamformer

First, we consider the Bartlett beamformer [6, p. 592-593], [2, p. 72-73], [8, p. 49-50], also known as the conventional beamformer. As many classical estimation methods, the Bartlett beamformer is based on the Fourier transform.
The basic idea of the Bartlett beamformer is to maximize the power of the beamforming output for a certain time delay τ_m. Additionally, we use the assumption that the measurement of the received signal is corrupted by AWCGN.
Therefore, we describe the interference

$$I_B(\boldsymbol{w}) = \mathbb{E}\left[|\boldsymbol{w}^{\mathrm{H}} \boldsymbol{n}|^2\right] , \tag{4.4}$$

with $\boldsymbol{n}$ defined as zero mean, temporarilly white and with all variances being equal.
Assuming that inference $I_B(\boldsymbol{w})$ is caused by Gaussian white noise also implies

$$\mathbb{E}\left[\boldsymbol{n}\right] = \boldsymbol{0} \qquad \text{and} \qquad \mathbb{E}\left[\boldsymbol{n}\boldsymbol{n}^{\mathrm{H}}\right] = \sigma^2 \boldsymbol{I} , \tag{4.5}$$

which exactly corresponds to the assumption made in the signal model.

The interference $I_B(\boldsymbol{w})$ can now be written as

$$I_B(\boldsymbol{w}) = \mathbb{E}\left[|\boldsymbol{w}^{\mathrm{H}} \boldsymbol{n}|^2\right] = \sigma^2 \boldsymbol{w}^{\mathrm{H}} \boldsymbol{I} \boldsymbol{w} = \sigma^2 |\boldsymbol{w}|^2 , \tag{4.6}$$

and we further obtain for the generic problem of minimizing the power of the interference

$$\boldsymbol{w}_B = \min_{\boldsymbol{w}} \sigma^2 |\boldsymbol{w}|^2 \tag{4.7}$$

To find the weight vector $\boldsymbol{w}$ and solve the optimization problem we consider a constraint which enables a signal with delay τ to pass the filter undistorted. As mentioned in section 4.1, the above weight vector operates like a spatial filter, which has been matched to the received signal.

$$\begin{aligned} \boldsymbol{w}^{\mathrm{H}} \boldsymbol{b}(\tau) \boldsymbol{s} &= \boldsymbol{s} \\ \boldsymbol{w}^{\mathrm{H}} \boldsymbol{b}(\tau) &= 1 \\ \boldsymbol{w}^{\mathrm{H}} \boldsymbol{b}(\tau) - 1 &= 0 \end{aligned} \tag{4.8}$$

Considering the constraint above we use the Lagrangian multiplier

$$L_{\mathrm{B}}(w,\lambda) = \sigma^2 \boldsymbol{w}^{\mathrm{H}}\boldsymbol{w} + \lambda_{Re}\,\mathrm{Re}\left\{\boldsymbol{w}^{\mathrm{H}}\boldsymbol{b}(\tau) - 1\right\} + \lambda_{Im}\,\mathrm{Im}\left\{\boldsymbol{w}^{\mathrm{H}}\boldsymbol{b}(\tau) - 1\right\} \tag{4.9}$$

$$= \sigma^2 \boldsymbol{w}^{\mathrm{H}}\boldsymbol{w} + \mathrm{Re}\left\{\lambda^*\left[\boldsymbol{w}^{\mathrm{H}}\boldsymbol{b}(\boldsymbol{\tau}) - 1\right]\right\}\,, \tag{4.10}$$

to solve the optimization, and we finally receive the weight vector $\boldsymbol{w}$:

$$\boldsymbol{w}_B = \|\boldsymbol{b}(\tau)\|^{-2}\boldsymbol{b}(\tau) \tag{4.11}$$

When inserting the weight vector into (4.2), we obtain the classical spectrum of the Bartlett beamformer:

$$P_{\mathrm{B}}(\tau) = \frac{\boldsymbol{b}(\tau)^{\mathrm{H}}\boldsymbol{R}\boldsymbol{b}(\tau)}{\|\boldsymbol{b}(\tau)\|^4} \tag{4.12}$$

By rearranging the equation of the Bartlett spectrum, one can now see that the Bartlett beamformer is an improved version of the classical periodogram estimate [6, p. 585-593], [8, p. 22]. We consider the covariance matrix $\boldsymbol{R}$ to be estimated as

$$\boldsymbol{R} = \frac{1}{N}\sum_{\forall n} \boldsymbol{x}_n \boldsymbol{x}_n^{\mathrm{H}}\,, \tag{4.13}$$

where $\boldsymbol{x}_n$ are realizations of $\boldsymbol{x}$ at different times $t = n\Delta t$, where Δt is a long period of time.

Then, we can rewrite the output power to

$$\begin{aligned} P_{\mathrm{B}}(\tau) &= \frac{\boldsymbol{b}(\tau)^{\mathrm{H}}\boldsymbol{R}\boldsymbol{b}(\tau)}{\|\boldsymbol{b}(\tau)\|^4} \\ &= \frac{1}{N}\sum_{n=1}^{N}\frac{1}{K^2}\left|\boldsymbol{b}(\tau)^{\mathrm{H}}\boldsymbol{x}_n\right|^2 \\ &= \frac{1}{K}\left[\frac{1}{N}\sum_{n=1}^{N}\frac{1}{K}\left|\sum_{k=1}^{K}\left[\boldsymbol{x}_n\right]_k \mathrm{e}^{-j2\pi f_k \tau}\right|^2\right] \end{aligned} \tag{4.14}$$

The output power can be interpreted as a data vector $\boldsymbol{x}_n$ multiplied with the response vector, squared and summed up over K measurement frequencies and averaged over a certain number of realizations N.
Therefore, the Bartlett method can also be interpreted as a procedure of averaging periodograms, operating on a number of N data segments of length K, considering that

$$P_{\boldsymbol{x}_n}(\tau) = \frac{1}{K}\left|\sum_{k=1}^{K}\left[\boldsymbol{x}_n\right]_k \mathrm{e}^{-j2\pi f_k \tau}\right|^2 \tag{4.15}$$

is the periodogram [6, p. 586-587] of $\boldsymbol{x}_n$.

Since the definition of the periodogram fits the functional form of a squared Fourier transform, we further conclude that the Bartlett method mathematically corresponds to a squared Fourier transform.

4.1.2 The Capon beamformer

The Capon beamformer [2, p. 73-74] is also known as the Minimum Variance Distorsionless (MVD) beamformer.
Its basic idea is to minimize the power contributed by any possible interference, including noise, which does not correspond to the wanted time delay. At the same time, a fixed gain is kept for the direct wave component, which we also call the LOS component. Like many other methods as well, the Capon beamformer was proposed in attempt to minimize the limitations of the Bartlett beamformer, especially its difficulty to resolve closely-spaced components.

The principal difference to the Bartlett beamformer is Capon's attempt to consider correlation, stating that interference assumed in the design can be caused by any signal. In contrast, the Bartlett beamformer assumes interference to be only caused by white gaussian noise.
Therefore, interference is now defined as

$$I_C(\boldsymbol{w}) = \mathbb{E}\left[|y(\boldsymbol{f}, \boldsymbol{w})|^2\right] = \boldsymbol{w}^{\mathrm{H}} \boldsymbol{R} \boldsymbol{w} \tag{4.16}$$

The optimization problem was then stated by Capon as

$$\min_{\boldsymbol{w}} I_C(\boldsymbol{w}) = \min_{\boldsymbol{w}} \boldsymbol{w}^{\mathrm{H}} \boldsymbol{R} \boldsymbol{w} \tag{4.17}$$

$$= \min_{\boldsymbol{w}} P(\boldsymbol{w}) \tag{4.18}$$

Further, we find the optimal weight vector $\boldsymbol{w}$ by applying the technique of Langrange multipliers:

$$L_{\mathrm{C}}(w, \lambda) = w^{\mathrm{H}} \boldsymbol{R} w + \mathrm{Re}\left\{\lambda^* \left[\boldsymbol{w}^{\mathrm{H}} \boldsymbol{b}(\boldsymbol{\tau}) - 1\right]\right\} \tag{4.19}$$

We obtain the Capon weight vector $\boldsymbol{w}_C$ by optimization of the above term as

$$\boldsymbol{w}_C = \frac{1}{\boldsymbol{b}(\tau)^{\mathrm{H}} \boldsymbol{R}^{-1} \boldsymbol{b}(\tau)} \boldsymbol{R}^{-1} \boldsymbol{b}(\tau) \tag{4.20}$$

We can clearly see the influence, that, in contrast to the Bartlett method, the weight vector also includes the covariance matrix $\boldsymbol{R}$ and therefore the signal data information. This is, as stated above, due to the assumption of interference being additionally caused by any signal and hence the consideration of correlation.

Inserting $\boldsymbol{w}_C$ into (4.2), we obtain the spectrum of the Capon beamformer:

$$P_{\mathrm{C}}(\boldsymbol{\tau}) = \frac{1}{\boldsymbol{b}(\tau)^{\mathrm{H}} \boldsymbol{R}^{-1} \boldsymbol{b}(\tau)} \tag{4.21}$$

4.2 Parametric approaches

As discussed in the previous chapter, spectral-based methods basically operate without making any assumptions on the signal, except for its stationarity. In contrast, parametric or so-called model-based methods [2, p. 76] exploit the underlying data model. This means, that they assume that the signal satisfies a specified model with known functional form. The parameter of interest is further estimated using the assumed model.

4.2.1 The MUSIC method

MUSIC [6, p. 615-630], [2, p. 74-75], standing for Multiple Signal Classification, is a method which exploits the parametric structure of the covariance matrix $\boldsymbol{R}$, and therefore is usually classified as a parametric method. Though it is often denoted as spectral-based method as well, as it generates a so-called *pseudospectrum* for estimation.
Specifically, MUSIC is a subspace-based approach, as its main idea is based on the eigenvalue decomposition of $\boldsymbol{R}$. The consideration of the eigen-structure of the covariance matrix $\boldsymbol{R}$ was a significant achievement in the process of developing estimation techniques. Involving the intrinsic properties of $\boldsymbol{R}$ for solving an estimation problem clearly improved the possibilities of estimation.

The method assumes that the complex signal amplitudes are realizations of a stochastic process $\boldsymbol{s}$ as

$$\mathbb{E}\left[\boldsymbol{s}\right] = \boldsymbol{0} \qquad \text{and} \qquad \mathbb{E}\left[\boldsymbol{s}\boldsymbol{s}^{\mathrm{H}}\right] = \boldsymbol{P}\,, \tag{4.22}$$

where $\boldsymbol{P}$ is the so-called source covariance matrix.
With this assumption the parametric structure of the covariance matrix is defined as

$$\boldsymbol{R} = \mathbb{E}\left[\boldsymbol{x}\boldsymbol{x}^{\mathrm{H}}\right] = \boldsymbol{B}(\boldsymbol{\tau})\boldsymbol{P}\boldsymbol{B}(\boldsymbol{\tau})^{\mathrm{H}} + \sigma^2\boldsymbol{I} \tag{4.23}$$

We assume that the source covariance matrix $\boldsymbol{P}$ has full rank M:

$$r\left(\boldsymbol{P}\right) = M, \tag{4.24}$$

and therefore, as $\boldsymbol{P}$ and $\boldsymbol{B}(\boldsymbol{\tau})\boldsymbol{P}\boldsymbol{B}(\boldsymbol{\tau})$ are *similar* matrices, we know

$$r\left(\boldsymbol{B}(\boldsymbol{\tau})\boldsymbol{P}\boldsymbol{B}(\boldsymbol{\tau})^{\mathrm{H}}\right) = M, \tag{4.25}$$

representing the *signal part* of the covariance matrix $\boldsymbol{R}$. We will now view that the method relies on the eigenvalue decomposition of $\boldsymbol{R}$, splitting the covariance matrix into a signal part and a noise part.

Applying eigenvalue decomposition means that the covariance matrix is split up into a diagonal matrix containing the eigenvalues multiplied with the corresponding eigenvector matrices, for the eigenvalue decomposition of the signal part $\boldsymbol{B}(\boldsymbol{\tau})\boldsymbol{P}\boldsymbol{B}(\boldsymbol{\tau})$ it further means that

$$\boldsymbol{B}(\boldsymbol{\tau})\boldsymbol{P}\boldsymbol{B}(\boldsymbol{\tau})^{\mathrm{H}} = \boldsymbol{U}\boldsymbol{\Lambda}_{\boldsymbol{o}}\boldsymbol{U}^{\mathrm{H}}, \tag{4.26}$$

where

$$\boldsymbol{U}\boldsymbol{U}^{\mathrm{H}} = \boldsymbol{U}^{\mathrm{H}}\boldsymbol{U} = \boldsymbol{I} \tag{4.27}$$

and $\boldsymbol{\Lambda}_o$ stands for the diagonal matrix of eigenvalues

$$\boldsymbol{\Lambda}_o = \mathrm{diag}\{\underbrace{\lambda_1, \ldots, \lambda_M}_{M\text{eigenvalues}}, \underbrace{0, \ldots, 0}_{K-M\text{zeros}}\}, \tag{4.28}$$

due to equation (4.25).
Furthermore, we rewrite the parametric structure of the covariance matrix as

$$\begin{aligned} \boldsymbol{R} &= \boldsymbol{B}(\boldsymbol{\tau})\boldsymbol{P}\boldsymbol{B}(\boldsymbol{\tau})^{\mathrm{H}} + \sigma^2\boldsymbol{I} && (4.29)\\ &= \boldsymbol{U}\left[\boldsymbol{\Lambda}_o + \sigma^2\boldsymbol{I}\right]\boldsymbol{U}^{\mathrm{H}} && (4.30)\\ &= \boldsymbol{U}\boldsymbol{\Lambda}\boldsymbol{U}^{\mathrm{H}}, \qquad \text{with} \quad \boldsymbol{\Lambda} = \boldsymbol{\Lambda}_o + \sigma^2\boldsymbol{I} && (4.31) \end{aligned}$$

where $\boldsymbol{\Lambda}$ contains both signal and noise eigenvalues

$$\boldsymbol{\Lambda} = \begin{bmatrix} \boldsymbol{\Lambda}_s & \boldsymbol{0} \\ \boldsymbol{0} & \boldsymbol{\Lambda}_n \end{bmatrix} \tag{4.32}$$

and $\boldsymbol{U}$ consists of the corresponding eigenvectors

$$\boldsymbol{U} = \begin{bmatrix} \boldsymbol{U}_s & \boldsymbol{U}_n \end{bmatrix}. \tag{4.33}$$

Hence $\boldsymbol{R}$ can further be split up to

$$\boldsymbol{R} = \boldsymbol{U}_s\boldsymbol{\Lambda}_s\boldsymbol{U}_s^{\mathrm{H}} + \boldsymbol{U}_n\boldsymbol{\Lambda}_n\boldsymbol{U}_n^{\mathrm{H}} \tag{4.34}$$

We now list the obtained eigenvalue and eigenvector matrices for a better understanding:

Matrix of M signal eigenvectors	$\boldsymbol{U}_{\mathbf{s}} = [\boldsymbol{u}_1, \ldots, \boldsymbol{u}_M]$
Matrix of K-M noise eigenvectors	$\boldsymbol{U}_{\mathbf{n}} = [\boldsymbol{u}_{M+1}, \ldots, \boldsymbol{u}_K]$
Diagonal matrix of M signal eigenvalues	$\boldsymbol{\Lambda}_{\mathrm{n}} = \mathrm{diag}\left\{\lambda_1 + \sigma^2, \ldots, \lambda_M + \sigma^2\right\}$
Diagonal matrix of K-M noise eigenvalues	$\boldsymbol{\Lambda}_{\mathbf{s}} = \mathrm{diag}\{\sigma^2, \ldots, \sigma^2\}$

Next, we find the corresponding subspaces to the signal and noise eigenvectors.
The signal eigenvectors lie in a subspace which we call *signal subspace*, containing the information about the signal components. Likewise, the noise subspace contains the noise eigenvectors and is orthogonal to the signal subspace.
It can be shown that the eigenvectors of $\boldsymbol{U}_{\mathbf{n}}$ are orthogonal to the $\boldsymbol{B}(\boldsymbol{\tau})$ matrix and we can write

$$\boldsymbol{B}(\boldsymbol{\tau})^{\mathrm{H}}\boldsymbol{U}_n = \boldsymbol{0} \tag{4.35}$$

For subspace-based methods, we can form a projection matrix $\boldsymbol{P}_s$ for the signal subspace

$$\boldsymbol{P}_s = \boldsymbol{U}_s\boldsymbol{U}_s^{\mathrm{H}} \tag{4.36}$$

In a similar way, a projection for the noise subspace can be determined.

$$\boldsymbol{P}_n = \boldsymbol{U}_n \boldsymbol{U}_n^{\mathrm{H}} = \boldsymbol{I} - \boldsymbol{P}_s \tag{4.37}$$

Now for the MUSIC method specifically, the squared magnitude of the projection of $\boldsymbol{b}(\tau)$ onto the noise subspace is used:

$$\boldsymbol{b}(\tau)^{\mathrm{H}} \boldsymbol{P}_n \boldsymbol{b}(\tau) = \boldsymbol{b}(\tau)^{\mathrm{H}} \boldsymbol{U}_n \boldsymbol{U}_n^{\mathrm{H}} \boldsymbol{b}(\tau) = \boldsymbol{b}(\tau)^{\mathrm{H}} \boldsymbol{U}_n \boldsymbol{U}_n^{\mathrm{H}} \boldsymbol{U}_n^{\mathrm{H}} \boldsymbol{U}_n \boldsymbol{b}(\tau) = \| \boldsymbol{U}_n \boldsymbol{U}_n^{\mathrm{H}} \boldsymbol{b}(\tau) \|^2 \tag{4.38}$$

From the orthogonality consideration in (4.35) we know that

$$\boldsymbol{b}(\tau)^{\mathrm{H}} \boldsymbol{U}_n = \boldsymbol{0} \tag{4.39}$$

$$\| \boldsymbol{b}(\tau)^{\mathrm{H}} \boldsymbol{U}_n \|^2 = 0 \tag{4.40}$$

$$\boldsymbol{b}(\tau)^{\mathrm{H}} \boldsymbol{U}_n \boldsymbol{U}_n^{\mathrm{H}} \boldsymbol{b}(\tau) = 0 \tag{4.41}$$

Taking into consideration that each of the signal components of $\boldsymbol{s}$ is orthogonal to the noise subspace, it is apparent that $\boldsymbol{b}(\tau)^{\mathrm{H}} \boldsymbol{U}_n \boldsymbol{U}_n^{\mathrm{H}} \boldsymbol{b}(\tau)$ is zero only if $\tau \in \{\tau_1, \ldots, \tau_M\}$. We further recognize that $\tau \in \{\tau_1, \ldots, \tau_M\}$ are the only possible solutions to the equation above.
From this insight, it follows that

$$P_{\mathrm{M}}(\tau) = \frac{1}{\boldsymbol{b}(\tau)^{\mathrm{H}} \boldsymbol{U}_n \boldsymbol{U}_n^{\mathrm{H}} \boldsymbol{b}(\tau)} \tag{4.42}$$

displays peaks at time delays τ, which is now defined to be the MUSIC pseudospectrum.

The pseudospectrum can be seen as spectral representation of the estimation result, basically expressing the distance between the two subspaces.

For the implementation of the MUSIC method in practice, the eigenvectors of the covariance matrix are separated into the signal and noise eigenvectors and sorted in relation to the corresponding eigenvalues.
The largest eigenvalues are then identified to be the eigenvalues of the signal subspace, with the remaining eigenvalues belonging to the noise subspace. It is very important to notice that the method expects the number of signal components M to be known.

4.2.2 Root-MUSIC

Next, we introduce an extension to MUSIC, the so-called Root-MUSIC method [6, p. 627-628], [2, p. 80]. As the name implies, it can be described as a polynomial-rooting variation of the subspace-based MUSIC approach.

From the previous chapter we know that the denominator goes to zero for $\tau_m \in \{\tau_1, \ldots, \tau_M\}$.

It follows that the denominator polynomial

$$\widehat{p}(z) = \widehat{\boldsymbol{b}}(z)^{\mathrm{H}} \boldsymbol{U}_n \boldsymbol{U}_n^{\mathrm{H}} \widehat{\boldsymbol{b}}(z)\,, \tag{4.43}$$

has M of its roots occurring on the unit circle, with

$$\widehat{\boldsymbol{b}}\,(z) = \begin{bmatrix} 1 & z & \ldots & z^{K-1} \end{bmatrix} \qquad \text{where} \quad \widehat{\boldsymbol{b}}\,(z) = \widehat{\boldsymbol{b}}\left(\mathrm{e}^{j\tau}\right) = \boldsymbol{b}\,(\tau) \tag{4.44}$$

The M roots on the unit circle are of interest for the estimation as they correspond to the delays of the signal components.

Therefore, we use $\widehat{\boldsymbol{b}}\left(z^{-1}\right)^{\mathrm{T}}$ for $\widehat{\boldsymbol{b}}\left(z\right)$ and define the Root-MUSIC polynomial $p(z)$ as

$$p(z) = \boldsymbol{b}\left(z^{-1}\right)^{\mathrm{T}} \boldsymbol{U}_n \boldsymbol{U}_n^{\mathrm{H}} \boldsymbol{b}\left(z\right) , \tag{4.45}$$

since $\boldsymbol{b}\left(z^{-1}\right)^{\mathrm{T}}$ Keep in mind that we now know that the roots of $\widehat{p}(z)$ are also roots of $p(z)$. These M roots are double roots, with

$$z^{-1} = z^{*} \tag{4.46}$$

The observation that the polynomial is conjugate symmetric

$$p\left(z\right) = p^{*}\left(\frac{1}{z^{*}}\right) , \tag{4.47}$$

as

$$\begin{aligned} p^{*}\left(\frac{1}{z^{*}}\right) &= \widehat{\boldsymbol{b}}\left(\frac{1}{z^{*}}\right)^{\mathrm{H}} \boldsymbol{U}_n \boldsymbol{U}_n^{\mathrm{H}} \widehat{\boldsymbol{b}}\left(\frac{1}{z^{*}}\right) \\ &= \widehat{\boldsymbol{b}}\left(\frac{1}{z^{-1}}\right)^{\mathrm{H}} \boldsymbol{U}_n \boldsymbol{U}_n^{\mathrm{H}} \widehat{\boldsymbol{b}}\left(\frac{1}{z^{-1}}\right) \\ &= \widehat{\boldsymbol{b}}\left(z\right)^{\mathrm{H}} \boldsymbol{U}_n \boldsymbol{U}_n^{\mathrm{H}} \widehat{\boldsymbol{b}}\left(z\right) \\ &= p(z) \end{aligned}$$

shows us, that if z is a root, $1/z^{*}$ is a root as well.
Therefore, by searching only for roots z_r with $|z_r| < 1$ and selecting the M roots with the largest magnitudes we obtain the estimates τ.

4.2.3 The ESPRIT method

Additional to MUSIC and Root-MUSIC, we discuss another parametric approach called ESPRIT [6, p. 638-649], [2, p. 80-81]. The name ESPRIT stands for Estimation of Signal Parameters via Rotational Invariance Techniques. ESPRIT belongs to the subspace-based methods and was especially inspired by MUSIC, though the concept is slightly different.
As implied by the name, ESPRIT makes use of the rotational invariance of subspaces. The mentioned invariance principle exists naturally for uniformly sampled sequences. Another difference is that, while MUSIC works with an estimate of the noise subspace, ESPRIT operates with the signal subspace.

For a better understanding of the ESPRIT method, we consider our signal model

$$\boldsymbol{x} = \boldsymbol{B}^{\mathrm{T}}\left(\boldsymbol{\tau}\right) \boldsymbol{s} + \boldsymbol{n}$$

with $\boldsymbol{x}$ consisting of K data samples, and start by sorting the data samples into two groups. Thus we define the two subvectors $\boldsymbol{x}_1$ and $\boldsymbol{x}_2$ by deleting the first and accordingly the last

sample, resulting into two vectors, each containing (K–1) data samples.

$$\boldsymbol{x} \doteq \begin{bmatrix} \boldsymbol{x}_1 \\ x\,[K] \end{bmatrix} = \begin{bmatrix} x\,[1] \\ \boldsymbol{x}_2 \end{bmatrix} \tag{4.48}$$

As in the MUSIC approach addressed in section 4.2.1, eigenvector decomposition is the underlying concept of subspace-based approaches and thus we have a look at the covariance matrix of $\boldsymbol{x}$. The eigenvector decomposition of the covariance matrix $\boldsymbol{R}$ was defined in (4.34) as

$$\begin{aligned} \boldsymbol{R} &= \boldsymbol{B}(\boldsymbol{\tau})\boldsymbol{P}\boldsymbol{B}(\boldsymbol{\tau})^{\mathrm{H}} + \sigma^2\boldsymbol{I} \\ &= \boldsymbol{U}_s\boldsymbol{\Lambda}_s\boldsymbol{U}_s^{\mathrm{H}} + \boldsymbol{U}_n\boldsymbol{\Lambda}_n\boldsymbol{U}_n^{\mathrm{H}} \\ &= \boldsymbol{U}_s\boldsymbol{\Lambda}_s\boldsymbol{U}_s^{\mathrm{H}} + \sigma^2\boldsymbol{U}_n\boldsymbol{U}_n^{\mathrm{H}} \end{aligned} \tag{4.49}$$

Further, the eigenvalue decomposition of the source covariance matrix $\boldsymbol{B}(\boldsymbol{\tau})\boldsymbol{P}\boldsymbol{B}(\boldsymbol{\tau})^{\mathrm{H}}$ was described as

$$\boldsymbol{B}(\boldsymbol{\tau})\boldsymbol{P}\boldsymbol{B}(\boldsymbol{\tau})^{\mathrm{H}} = \boldsymbol{U}\boldsymbol{\Lambda}_{\boldsymbol{o}}\boldsymbol{U}^{\mathrm{H}},$$

where $\boldsymbol{\Lambda}_o$ contains the noise subspace eigenvalues $\lambda_1, \ldots, \lambda_M$:

$$\boldsymbol{\Lambda}_o = \mathrm{diag}\,\{\lambda_1, \ldots, \lambda_M, 0, \ldots, 0\}.$$

As derived in section 4.2.1, the signal subspace is spanned by the columns of the matrix $\boldsymbol{B}(\boldsymbol{\tau})$. Considering that the columns of $\boldsymbol{U}_s$ and $\boldsymbol{B}(\boldsymbol{\tau})$ span the same subspace, they can be related by a certain transformation matrix $\boldsymbol{T}$ by

$$\boldsymbol{U}_s = \boldsymbol{B}(\boldsymbol{\tau})\boldsymbol{T} \tag{4.50}$$

Note that $\boldsymbol{T}$ has full rank M and is determined as shown here:

$$\begin{aligned} \boldsymbol{B}(\boldsymbol{\tau})\boldsymbol{P}\boldsymbol{B}(\boldsymbol{\tau})^{\mathrm{H}} &= \boldsymbol{U}_{\boldsymbol{s}}\widehat{\boldsymbol{\Lambda}}_{\boldsymbol{o}}\boldsymbol{U}_{\boldsymbol{s}}^{\mathrm{H}} \\ \boldsymbol{B}(\boldsymbol{\tau})\boldsymbol{P}\boldsymbol{B}(\boldsymbol{\tau})^{\mathrm{H}}\boldsymbol{U}_{\boldsymbol{s}}\widehat{\boldsymbol{\Lambda}}_{\boldsymbol{o}}^{-1} &= \boldsymbol{U}_{\boldsymbol{s}}, \\ \boldsymbol{B}(\boldsymbol{\tau})\boldsymbol{T} = \boldsymbol{U}_s \qquad &\text{so that} \quad \boldsymbol{T} = \boldsymbol{P}\boldsymbol{B}(\boldsymbol{\tau})^{\mathrm{H}}\boldsymbol{U}_{\boldsymbol{s}}\widehat{\boldsymbol{\Lambda}}_{\boldsymbol{o}}^{-1}, \end{aligned} \tag{4.51}$$

where $\widehat{\boldsymbol{\Lambda}}_{\boldsymbol{o}}$ now is

$$\widehat{\boldsymbol{\Lambda}}_{\boldsymbol{o}} = \mathrm{diag}\,\{\lambda_1, \ldots, \lambda_M\}. \tag{4.52}$$

Furthermore, we define two subarrays of the response matrix $\boldsymbol{B}(\boldsymbol{\tau})$, similar as in (4.48). By deleting the first and last row of $\boldsymbol{B}(\boldsymbol{\tau})$ we obtain the sub-matrices $\boldsymbol{B}_1(\boldsymbol{\tau})$ and $\boldsymbol{B}_2(\boldsymbol{\tau})$

$$\boldsymbol{B}(\boldsymbol{\tau}) = \begin{bmatrix} \boldsymbol{B}_1(\boldsymbol{\tau}) \\ B^{(K)}(\boldsymbol{\tau}) \end{bmatrix} = \begin{bmatrix} B^{(1)}(\boldsymbol{\tau}) \\ \boldsymbol{B}_2(\boldsymbol{\tau}) \end{bmatrix} \tag{4.53}$$

Due to the rotational invariance principle, the relation between the subspace response matrices $\boldsymbol{B}_1(\boldsymbol{\tau})$ and $\boldsymbol{B}_2(\boldsymbol{\tau})$ can be expressed by

$$\boldsymbol{B}_2(\boldsymbol{\tau}) = \boldsymbol{B}_1(\boldsymbol{\tau})\boldsymbol{D}(\boldsymbol{\tau}), \tag{4.54}$$

with $\boldsymbol{D}(\boldsymbol{\tau})$ being a unitary matrix performing a rotation of the individual column vectors of $\boldsymbol{B}_1(\boldsymbol{\tau})$.

Now specifically looking at the signal subspace vectors associated with the recently found response matrices $\boldsymbol{B}_1(\boldsymbol{\tau})$ and $\boldsymbol{B}_2(\boldsymbol{\tau})$, we get

$$\boldsymbol{U}_{s1} = \boldsymbol{B}_1(\boldsymbol{\tau})\boldsymbol{T} \qquad \text{and} \quad \boldsymbol{U}_{s2} = \boldsymbol{B}_2(\boldsymbol{\tau})\boldsymbol{T} \tag{4.55}$$

Combining it with the relation from (4.54) we obtain

$$\begin{aligned} \boldsymbol{U}_{s2}(\boldsymbol{\tau}) &= \boldsymbol{U}_{s1}(\boldsymbol{\tau})\boldsymbol{C}(\boldsymbol{\tau}) \\ \boldsymbol{B}_2(\boldsymbol{\tau})\boldsymbol{T} &= \boldsymbol{B}_1(\boldsymbol{\tau})\boldsymbol{T}\boldsymbol{C}(\boldsymbol{\tau}) \\ \boldsymbol{B}_1(\boldsymbol{\tau})\boldsymbol{D}(\boldsymbol{\tau})\boldsymbol{T} &= \boldsymbol{B}_1(\boldsymbol{\tau})\boldsymbol{T}\boldsymbol{C}(\boldsymbol{\tau}) \\ \boldsymbol{D}(\boldsymbol{\tau})\boldsymbol{T} &= \boldsymbol{T}\boldsymbol{C}(\boldsymbol{\tau}) \end{aligned}$$

so that

$$\boldsymbol{C}(\boldsymbol{\tau}) = \boldsymbol{T}^{-1}\boldsymbol{D}(\boldsymbol{\tau})\boldsymbol{T} \tag{4.56}$$

with $\boldsymbol{C}(\boldsymbol{\tau})$ and $\boldsymbol{D}(\boldsymbol{\tau})$ occurring to be *similar* matrices and thus sharing the same eigenvalues.

Consequently, the estimation problem can be compressed to solving $\boldsymbol{U}_{s2}(\boldsymbol{\tau}) = \boldsymbol{U}_{s1}(\boldsymbol{\tau})\boldsymbol{C}(\boldsymbol{\tau})$. The estimates are obtained by computing the eigenvalues of $\boldsymbol{C}(\boldsymbol{\tau})$ and selecting the M largest ones.

4.2.4 The Maximum Likelihood estimator

Lastly, we consider the maximum-likelihood (ML) estimator [2, p. 76-77], which is probably the most well known model-based approach. Note that we consider the deterministic ML estimator in this work.
For the derivation of the ML estimator, we take into consideration our signal model from (3.26), where the noise $\boldsymbol{n}$ is defined to be a circularly symmetric and temporally white Gaussian random process, with

$$\mathbb{E}[\boldsymbol{n}] = \boldsymbol{0} \qquad \text{and} \qquad \mathbb{E}\left[\boldsymbol{n}\boldsymbol{n}^{\mathrm{H}}\right] = \sigma^2\boldsymbol{I} \tag{4.57}$$

As $\boldsymbol{x}$ is a complex normal distributed vector, with mean $\boldsymbol{B}(\boldsymbol{\tau})\,\boldsymbol{s}$

$$\boldsymbol{x} \sim \mathcal{CN}\left(\boldsymbol{B}(\boldsymbol{\tau})\,\boldsymbol{s}, \sigma^2\boldsymbol{I}\right) \tag{4.58}$$

we can write down the *likelihood function* [7, p. 29]

$$f_{\mathrm{x}}\left(\boldsymbol{x}; \boldsymbol{\tau}, \boldsymbol{s}, \sigma^2\right) = \prod_{i=1}^{N} \frac{1}{\left(\pi\sigma^2\right)^M} \mathrm{e}^{-\frac{\|\boldsymbol{x_i} - \boldsymbol{B}^{\mathrm{T}}(\boldsymbol{\tau})\boldsymbol{s}\|^2}{\sigma^2}}, \tag{4.59}$$

with the probability density function (PDF) $f_{\mathrm{x}}\left(\boldsymbol{x}; \boldsymbol{\tau}, \boldsymbol{s}, \sigma^2\right)$ [9, p. 147].

We must consider three unknown parameters which are the signal parameter $\boldsymbol{\tau}$, two complex amplitudes $\boldsymbol{s}$ and the noise variance σ^2.

The maximum likelihood estimate is defined as the value that maximizes the likelihood function as

$$\widehat{\boldsymbol{\tau}} = \arg\max_{\boldsymbol{\tau}} f_{\mathrm{x}}\left(\boldsymbol{x};\boldsymbol{\tau},\boldsymbol{s},\sigma^2\right) = \arg\max_{\boldsymbol{\tau}} \prod_{i=1}^{N} \frac{1}{\left(\pi\sigma^2\right)^M} \mathrm{e}^{-\frac{\|\boldsymbol{x_i}-\boldsymbol{B}^{\mathrm{T}}(\boldsymbol{\tau})\boldsymbol{s}\|^2}{\sigma^2}} \tag{4.60}$$

We obtain the maximum of the *log likelihood function* as

$$\arg\max_{\boldsymbol{\tau}} L_{\mathrm{x}}\left(\boldsymbol{x};\boldsymbol{\tau},\boldsymbol{s},\sigma^2\right) = \arg\max_{\boldsymbol{\tau}} \ln\left(f_{\mathrm{x}}\left(\boldsymbol{x};\boldsymbol{\tau},\boldsymbol{s},\sigma^2\right)\right) \tag{4.61}$$

Since the deterministic ML estimator maximizes the likelihood function, we can neglect the term $\ln(\pi)$, and we normalize by N, so that we get

$$\arg\max_{\boldsymbol{\tau}} L_{\mathrm{x}}\left(\boldsymbol{x};\boldsymbol{\tau},\boldsymbol{s},\sigma^2\right) = \arg\max_{\boldsymbol{\tau}} L_{\mathrm{x}}\left\{M\ln\left(\sigma^2\right) - \frac{1}{\sigma^2 N}\sum_{i=1}^{N}\left\|\boldsymbol{x_i} - \boldsymbol{B}^{\mathrm{T}}\left(\boldsymbol{\tau}\right)\boldsymbol{s}\right\|^2\right\} \tag{4.62}$$

We wish to find the estimates $\left(\widehat{\boldsymbol{\tau}},\widehat{\boldsymbol{s}},\widehat{\sigma}^2\right)$ of the unknown parameters $\left(\boldsymbol{\tau},\boldsymbol{s},\sigma^2\right)$, wherefore we take the derivative with respect to the unknown parameters and set it to zero. In our case, we first solve the equation for $\boldsymbol{s}$, keeping $\boldsymbol{\tau}$ and σ^2 fixed. As discussed more detailed in [2, p. 76-77], we receive the estimate $\widehat{\boldsymbol{s}}$ as

$$\widehat{\boldsymbol{s}}(\boldsymbol{\tau}) = \boldsymbol{B}(\boldsymbol{\tau})^{\dagger}\boldsymbol{x} \tag{4.63}$$

with $\boldsymbol{B}(\boldsymbol{\tau})^{\dagger}$ being the pseudo-inverse of $\boldsymbol{B}(\boldsymbol{\tau})$ as

$$\boldsymbol{B}(\boldsymbol{\tau})^{\dagger} = \left[\boldsymbol{B}(\boldsymbol{\tau})^{\mathrm{H}}\boldsymbol{B}(\boldsymbol{\tau})\right]^{-1}\boldsymbol{B}(\boldsymbol{\tau})^{\mathrm{H}} \tag{4.64}$$

Solving for σ^2 in the next step with fixed $\boldsymbol{\tau}$, and further inserting $\widehat{\boldsymbol{s}}(\boldsymbol{\tau})$ results into the estimate $\widehat{\sigma}^2$ to be

$$\widehat{\sigma}^2(\boldsymbol{\tau}) = \frac{1}{M}\,\mathrm{tr}\left\{\Pi^{\perp}_{B(\tau)}\boldsymbol{R}\right\} \tag{4.65}$$

Considering a subspace spanned by the columns of $\boldsymbol{B}(\boldsymbol{\tau})$, $\Pi_{B(\tau)}$ is the orthogonal projection on this subspace. Thus $\Pi^{\perp}_{B(\tau)}$ is the orthogonal projector on the subspace of $\boldsymbol{B}(\boldsymbol{\tau})^{\mathrm{H}}$.
Finally we insert the results of $\widehat{\boldsymbol{s}}(\boldsymbol{\tau})$ and $\widehat{\sigma}^2(\boldsymbol{\tau})$ into the log likelihood function in equation (4.62) and obtain the estimate

$$\widehat{\boldsymbol{\tau}} = \arg\max_{\boldsymbol{\tau}} L_{\mathrm{x}}\left(\boldsymbol{x};\boldsymbol{\tau},\boldsymbol{s},\sigma^2\right) = \arg\min \mathrm{tr}\left\{\Pi^{\perp}_{B(\tau)}\boldsymbol{R}\right\} \tag{4.66}$$

5 Simulation

In this thesis, the aim to evaluate different estimation methods for carrier phase-based ranging was primarily accomplished by the use of simulations.
The discussed estimation methods were implemented in the programming language Matlab, and a theoretical measurement signal suitable to test various estimation scenarios was generated. Therefore, the signal model introduced in chapter 3 was applied. The signal model was implemented to define the measurement signal from a set of parameters, where the parameters can be adjusted to simulate different situation scenarios.
The considered scenarios were chosen to imitate real life situations and were structured into five main scenarios.

- Single component
  - Variation of SNR (scenario 1)
- Two components
  - Variation of SNR (scenario 2)
  - Variation of inter-component distance (scenario 3)
  - Variation of the LOS gain (scenario 4)
- Diffuse Multipath (scenario 5)

For each scenario, the estimation methods were statistically evaluated over a certain number of random noise realizations. Additionally, the phase is randomly generated for each realization, which is further explained in the following section 5.1. The results of the different estimation methods were compared with respect to the influence of certain parameters.

5.1 Parameters

A Matlab script named *getParameters* sets the relevant parameters for the purpose of simulation. A short description of the most important parameters follows below. Additionally, the parameter values used by default are summarized in table 5.1. For all estimation scenarios, the parameters headed in table 5.1 are used unless explicitly specified.

5.1.1 Basic parameters

First, we introduce the so-called basic parameters, the bandwidth B_0, the number of frequencies K and the number of measurements per frequency N.

Parameters	Symbol	Default value
Bandwidth	B_0	78 MHz
Number of frequencies	K	40
Number of measurements per frequency	N	1
Number of signal components	M	2
Distance of LOS component	d_1	10 m
Distance of reflected component	d_2	12 m
Distance between components	$d_{\Delta 12}$	2 m
Magnitude of LOS component	A_1	1
Magnitude of reflected component	A_2	0.75
Phase of LOS component	ϕ_1	$\in [-\pi; \pi]$
Phase of reflected component	ϕ_2	$\in [-\pi; \pi]$
Signal-to-noise ratio	SNR	40 dB
Minimum distance	d_{min}	0 m
Maximum distance	d_{max}	70 m
Distance step size	Δd	0.014 m
Number of realizations	N_R	10000
Smoothing factor	K_s	20

Table 5.1: Parameters used for simulation by default

As mentioned in chapter 1, the specific aim is to find a robust estimation method adaptable for Bluetooth. BT is seen as a potential RF technology suitable for practical purpose and therefore also generally used as standard for the evaluation in this thesis. The frequency range of BT goes from 2.402 GHz to 2.480 GHz, hence the bandwidth of 78 MHz was used by default in every simulation scenario.

Considering our signal model in section 3, we operate with K measurement frequencies within the available frequency range. For the simulation the number of measurement frequencies K was set to 40 according to the BT standard.

Additionally, N indicates the number of measurements per frequency K. Note that N is specifically set to 1 in this work.
Since we deal we the BT standard, the ISM band is divided into individual channels, as introduced in chapter 1. However, measuring at K frequencies in the ISM band produces a large overhead, wherefore, $N = 1$ is chosen for time efficiency reasons. In other words, the choice of $N = 1$ is considered to be most convenient explicitly for the pratical use of BT. Note that for $N = 1$ smoothing needs to be taken into consideration (see section 5.2.3).

5.1.2 Signal parameters

Next, an insight is given on the signal parameters used for generating the signal vector $\boldsymbol{x}$.
As explained in section 3, the signal $\boldsymbol{x}$ can be split up into a noise part $\boldsymbol{n}$ and a signal part $\boldsymbol{x}_{\text{sig}}$, the latter containing information about the exponential signal components. For the signal part, we choose the magnitudes A_m for the purpose of simulation.
Further, we assume the phases ϕ_m to be uniformly distributed between $-\pi$ and π and thus operate with a random phase for each realization. Note that the phases ϕ_m are *randomly* generated

in the interval $[-\pi; \pi]$.
The magnitudes A_m and phases ϕ_m are included in the complex gains α_m as defined in the signal model in (3.8).
As defined in the signal model (3.25), the noise part of the signal is defined to be AWCGN by default, with different SNR values to be chosen in dB.

Additionally, for the simulation we choose the distance d between sender and receiver to be estimated. As introduced in (2.5), the parameter of interest τ relates to the distance d as $\tau = \frac{d}{c}$.
For purposes of simulation it is convenient to set the distance vector d in m, and further transform its value to the time delay for generating the signal vector $\boldsymbol{x}$.
For the default case we define a distance of 10 m considering the LOS component. Additionally, a reflective component is simulated, which is assumed to have a longer time delay than the LOS component, as reflections are sensed at the receiver after the direct signal. For the reflective component a time delay τ is generated corresponding to a distance d_2 of 12 m. Therefore, the distance between the LOS component and the reflection $d_{\Delta 12}$ is 2 m for our standardized case. However, $d_{\Delta 12}$ will vary in different scenarios.

5.1.3 Grid parameters

Since spectral-based estimation methods proceed by forming a spectrum-like function, they require a reasonable interpretation of the obtained spectrum.
A possible approach is a *grid-based* evaluation combined with peak finding approaches. However, since MUSIC forms a pseudospectrum to estimate the parameter of interest, grid based evaluation and peak finding is applied as well.
Therefore, in this work we refer to Bartlett, Capon and MUSIC as spectrum-*forming* methods for the reason of interpretation, even though MUSIC of course is a model-based approach. Note that in contrast the beamforming methods Bartlett and Capon are classified to be spectral-*based* in section 4.1.
For a grid-based evaluation, we define the minimum distance d_{min} and the maximum distance d_{max}. As discussed in section 5.2.1.1, oversampling is applied with a step size Δd of 0.014 m.

5.1.4 Additional parameters

Additional parameters for simulation are the number of realizations N_R for statistical evaluation and the smoothing factor K_s. The smoothing factor K_s will be discussed in section 5.3.4.

5.2 Scenario 1 - Single component: Variation of SNR

For every estimation method, the SNR has a significant impact on its performance. As noise is always present in real life scenarios and highly dependent on the hardware implementation, it is essential to know which SNR is needed to meet system specifications.
Consequently, for the evaluation of different estimation methods, simulated tests in relation to various SNR values remain indispensable. First of all, we consider a so-called basic scenario for validating the implementation of the algorithms. In this case we assume that there is only one exponential signal component in AWCGN, without any reflective components added. The signal parameters used for scenario 1 are stated in table 5.2. For one signal component in AWCGN, neglecting any other influence, each method should yield accurate results for a sufficient SNR.

This test represents real life situation with no or negligible small reflections from the environment, but is further considered to prove the accuracy of the implementated algorithms.

Parameters	Symbol	Scenario 1
Number of signal components	M	1
Distance of LOS component	d_1	10 m
Magnitude of LOS component	A_1	1
Signal-to-noise ratio	SNR	to be varied

Table 5.2: Signal parameters for scenario 1

First of all, single tests of the spectrum-forming methods considering one random noise realization $N_R = 1$ are presented. The following results already provide an insight into the influence of SNR on the estimation methods. Moreover, they reveal important characteristics of the Bartlett, the Capon and the MUSIC spectrum.

5.2.1 Single realization evaluation

5.2.1.1 Characteristic of the Bartlett spectrum

In scenario 1, we wish to estimate the true distance $d_1 = 10m$ and therefore expect the peak of the spectrum to be detected at 10 m.
In figure 5.1 the LOS component marked in black demonstrates the true distance. In this figure Bartlett spectra of different SNR values are presented, gained using a single random noise realization.

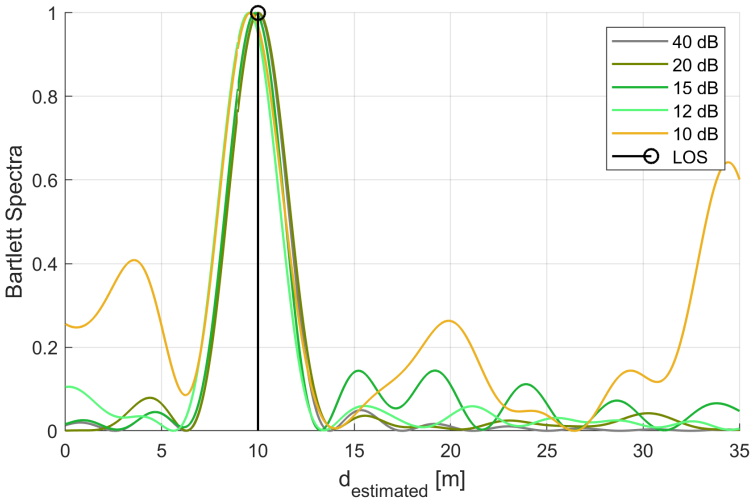

Figure 5.1: Bartlett Spectra for different SNRs, $N_R = 1$

As mentioned in section 4.1.1, the Bartlett method mathematically corresponds to a squared Fourier transform. Hence the Bartlett spectrum contains side lobes showing a characteristic of the Dirichlet Kernel, due to the rectangular shape of the function in the frequency domain. As viewed in figure 3.1, the rectangular shape originates from the K measurement frequencies which correspond to CW signals sensed at the receiver and conform to pulse-like measurements in the frequency domain.

Considering different choices of the SNR in figure 5.1, we observe that the side lobes become rather dominant for low SNR values of less than 20 dB, especially visible at an SNR as low as 10 dB.
Dominant side lobes are caused by superposition with noise and can hinder accurate peak detection. The difficulties of peak detection will be discussed later in section 5.5.

Note that oversampling is applied to improve the sample rate of the Bartlett spectrum in the time domain. As stated in [2, p. 773], the minimum step size of the Bartlett spectrum is limited by the bandwidth.
Equivalent to the FFT, the limitation can be determined by the bin size. In our case, $K = 40$ frequency sample points correspond to the FFT bins. Considering the BT standard with a bandwidth of 78 MHz minimum time step Δt is

$$\Delta t = \frac{1}{K\Delta f} \approx \frac{1}{B_0} \tag{5.1}$$

Furthermore, the minimum Δd can be determined as

$$\Delta d = \frac{c}{K\Delta f} = 3.84 \text{ m} \tag{5.2}$$

Without oversampling, the LOS component can be estimated correctly if its position exactly corresponds to one sample of the FFT grid. Practically this is only possible if we assume that the signal is critically and synchronously sampled, which of course is not the case in general.

However, oversampling allows to interpolate the function in the time domain equivalent to zero-padding [8, p. 27].

By adding zeros, it is assumed that additional samples of the spectrum effectively are zero. In our case, we consider a sampled function in the frequency domain. As the K measurement frequencies correspond to periodic signals in the time domain and the number of measurements is clearly restricted, our initial rectangular function is indeed bandlimited (see figure 3.1).
Hence the assumption of all additional samples being zero is fulfilled, and we receive accurate interpolation in the time domain. Oversampling can be applied without issues in our case for a smaller step size Δd.
In figure 5.2(a) and 5.2(b) we compare the Bartlett spectrum considering an SNR of 40 dB with and without oversampling. In figure 5.2(a) we can see that the sample points of the spectrum correspond to the determined Δd of 3.84 m.

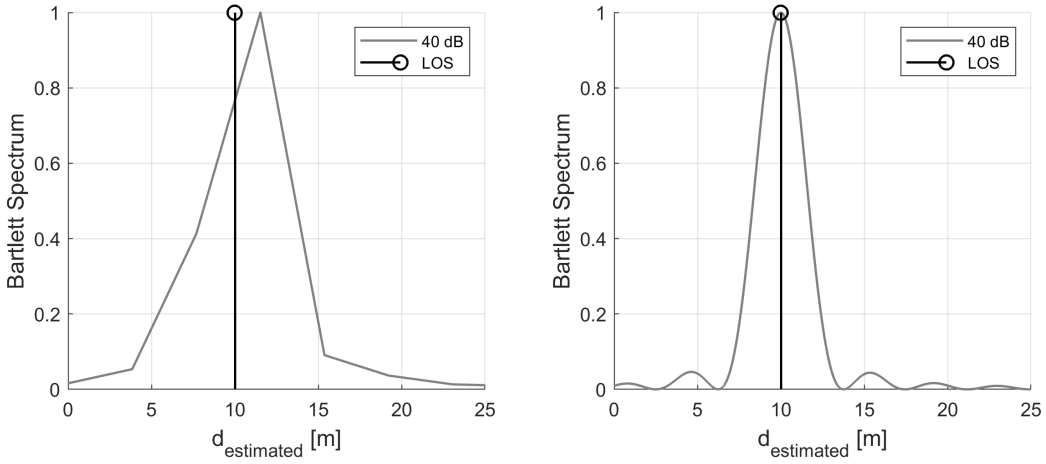

(a) without oversampling (b) with oversampling

Figure 5.2: Bartlett spectrum, SNR = 40 dB

5.2.1.2 Characteristic of the Capon spectrum

Next, we view the different characteristics of the Bartlett spectrum and the Capon spectrum. Considering the spectrum formed by the Capon beamformer, we expect a more narrow main lobe as discussed f.e. in [2]. The Capon method was developed with the aim to improve Bartlett's significant limitation of separating closely-spaced signal components due to its broad main lobe characteristic [2, p. 73-74].

In figure 5.3, the main lobes of Capon spectra sre indeed narrow in contrast to the Bartlett spectra shown in the previous section.
However, the Capon method requires smoothing of the covariance matrix as $N = 1$ in our case. In figure 5.3 a smoothing factor K_s of 20 is chosen. We will deal with smoothing in section 5.2.3 and have a closer look at its effects.

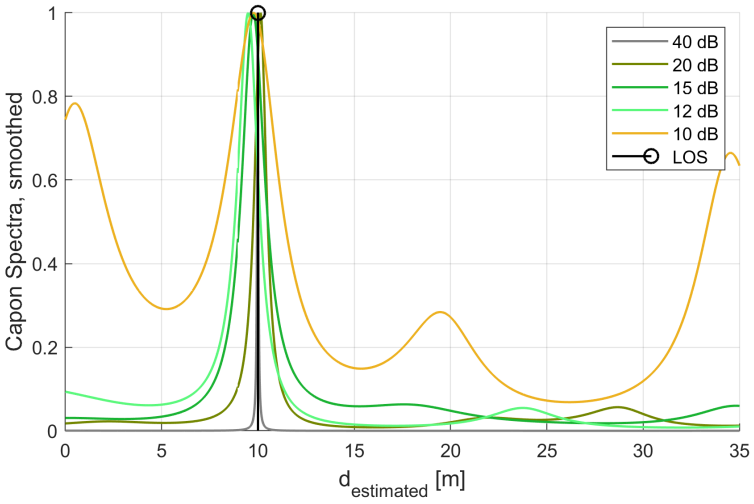

Figure 5.3: Capon Spectra for different SNR, $N_R = 1$

5.2.1.3 Characteristic of the MUSIC pseudospectrum

Comparing the MUSIC pseudospectrum to the spectra of the beamforming methods in figure 5.1 and figure 5.3 provides an insight into the advantages of subspace-based methods.

In figure 5.4, we observe that the influence of the noise floor is less significant in the MUSIC pseudospectrum. Due to the differentiation of the noise and the signal subspace, noise can be suppressed significantly.
Side lobes which could complicate peak detection are generally not part of the characteristic of the MUSIC spectrum.

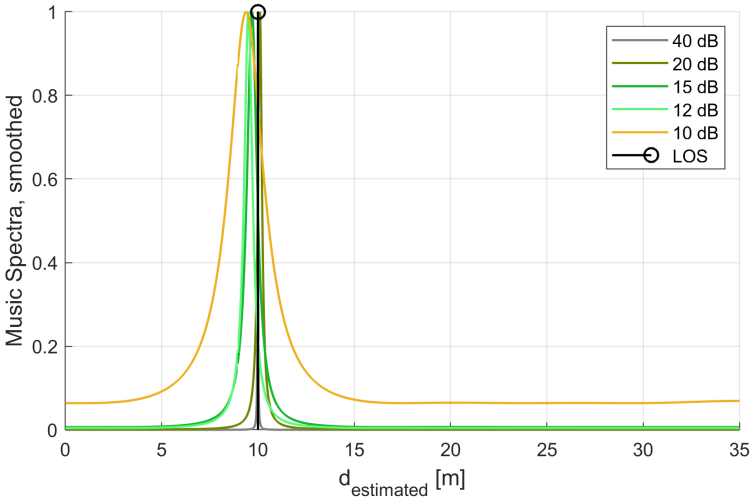

Figure 5.4: MUSIC Spectra for different SNR, $N_R = 1$

However, as mentioned in section 4.2.1, we need to consider that the method expects the number of signal components M to be known. In this context, the number of signal components is often referred to as the *model order* and appears to be an issue for all considered model-based methods MUSIC, Root-MUSIC and ESPRIT.

In simulation the number of signal components is effectively known from the simulated signal vector $\boldsymbol{x}$, so that the MUSIC method can perform accurately.

Nevertheless, in real life situations the model order is unknown, and additional peaks can occur in the MUSIC pseudospectrum as well, usually from a model order chosen higher than M as seen in figure 5.5. The choice of the model order will be dicussed later in section 5.3.3.

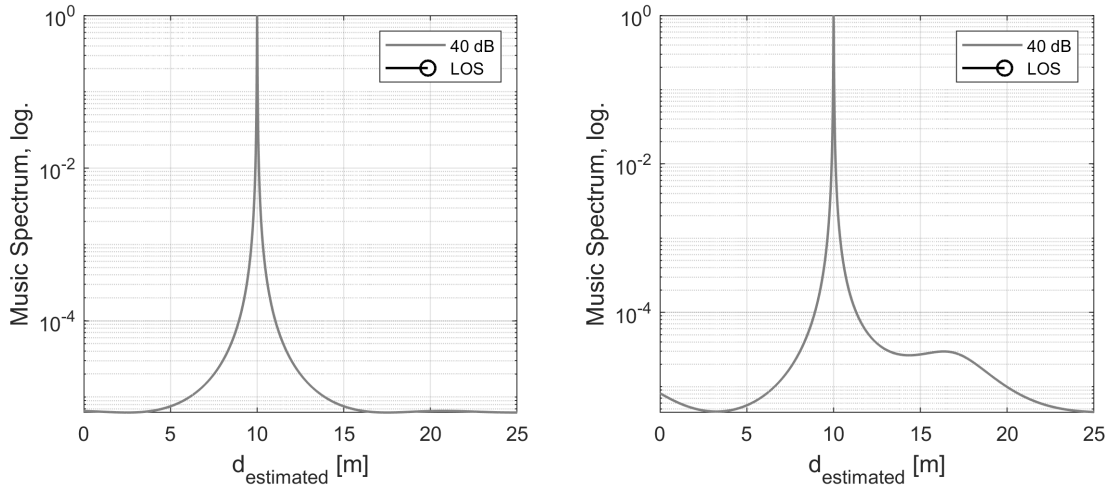

(a) Model order chosen equal to M

(b) Model order chosen $> M$

Figure 5.5: MUSIC spectrum, SNR = 40 dB

Additionally, the main lobe is narrow-shaped and therefore promises good results for cases of more signal components. In contrast, the rather broad main lobe of the Bartlett spectrum might hinder the separation of closely-spaced signal components in its spectrum. We will evaluate ability of separating closely-spaced signals in following scenarios.
In figure 5.4 smoothing was applied with the same smoothing factor $K_s = 20$ as chosen for the Capon beamformer.

5.2.2 Statistical evaluation

However, for reliable results, estimation methods must be evaluated statistically.
In this section, the spectra of the Bartlett and the Capon method are averaged and plotted in figure 5.6 and figure 5.7.

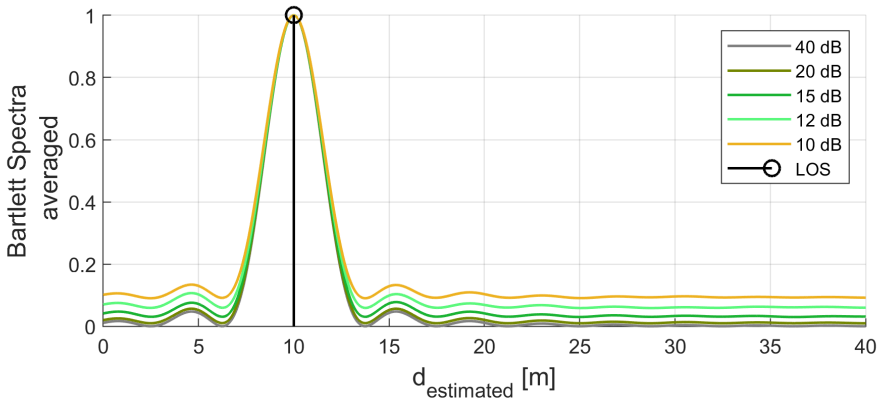

Figure 5.6: Bartlett Spectra for different SNR (averaged, $N_R = 10000$)

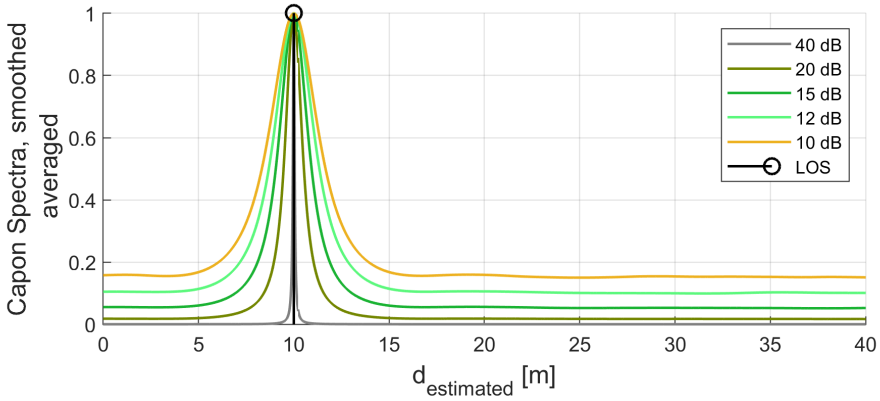

Figure 5.7: Capon Spectra for different SNR (averaged, $N_R = 10000$)

We observe a similar trend as discussed in section 5.2.1.2. The Bartlett spectrum shows a broad main lobe in general, as well as a distinctive impact of noise on the side lobes. In contrast, the main lobe of the Capon spectrum is influenced by noise too, and can be narrowed significantly for high SNR.
Additionally, averaged pseudospectra of MUSIC are shown in figure 5.8. The suppression of the noise floor is clearly visible as the model order is chosen suitable in the simulation.

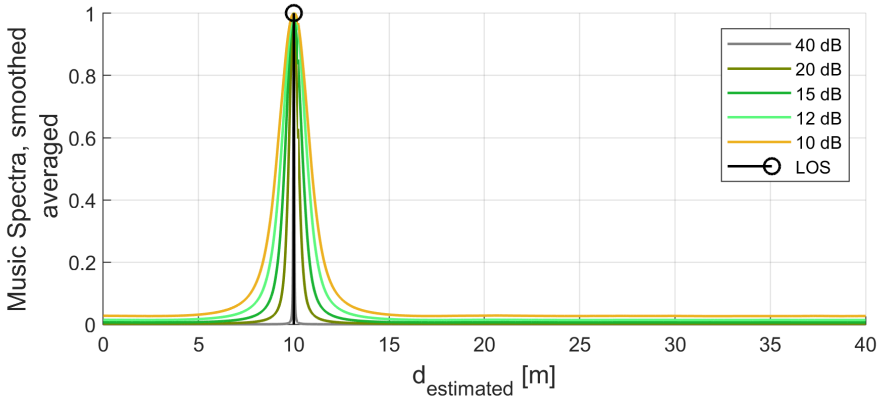

Figure 5.8: MUSIC Spectra for different SNR, smoothed (averaged, $N_R = 10000$)

It is noticeable that the true distance of 10 m is statistically determined correctly in this scenario 1, as the peak of the averaged spectra equals the LOS component even for low SNR values of 12 or 10 dB.
It verifies that results are unbiased considering a statistical evaluation of noise realizations, as noise is defined to be AWCGN and thus zero-mean.

The remaining model-based approaches Root-MUSIC and ESPRIT are included in figure 5.9, where all methods are averaged for an SNR of 20 dB.

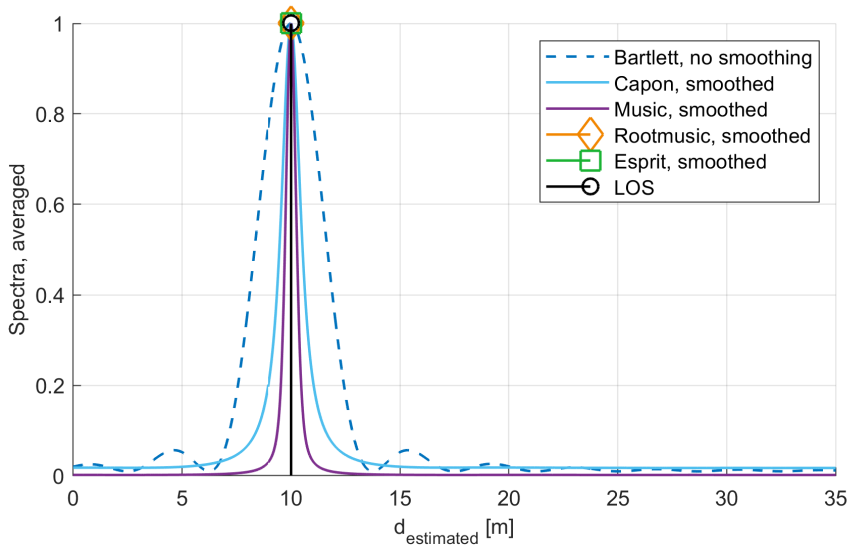

Figure 5.9: Estimation results for $SNR = 20dB$ (averaged, $N_R = 10000$)

Again, the plot shows the different spectrum characteristics of Bartlett, Capon and MUSIC, but further presents statistically unbiased results of Root-MUSIC and ESPRIT.
However, an interpretation of the latter methods is rather difficult, as Root-MUSIC and ESPRIT do not form a spectrum. Instead, both methods provide the result of the estimated parameter as a scalar. In figure 5.9, the mean value of the results of Root-MUSIC and ESPRIT are plotted in orange and green, and equal the LOS component. For a better understanding of their performance, the evaluation of bias and standard deviation is considered starting from section 5.2.5.

Note that the Bartlett spectrum is plotted with a dashed line implying that the method was applied without smoothing. We discuss smoothing and its impact on different methods in the following section.

5.2.3 Smoothing

As mentioned in section 5.2.1.2, smoothing [2, p. 75-76], [8, p. 168-170] is required for the Capon method, but also for MUSIC, Root-MUSIC and ESPRIT.
For estimation, we consider the covariance matrix estimate $\boldsymbol{R}$ from (4.13) with N realizations of $\boldsymbol{x}$. Hence, the covariance matrix $\boldsymbol{R}$ contains the signal information and shows the correlation of the measurement data. For $N = 1$ specifically, the covariance matrix $\boldsymbol{R}$ is rank deficient. Thus smoothing is indispensable for the above mentioned methods, as a decorrelated covariance matrix is essential to gain satisfying results.

To eliminate the correlation of the elements of the covariance matrix, smoothing is applied. The procedure of smoothing can be described as averaging of matrix elements. In other words, smoothing describes an approach to decorrelate $\boldsymbol{R}$.
For smoothing, we consider the smoothing factor K_s and a number of subarrays P which are related by

$$P = K–K_s + 1 \tag{5.3}$$

While $\boldsymbol{R}$ has dimensions $K \times K$, the smoothed covariance matrix has the dimensions $K_s \times K_s$. The smoothing factor K_s has to be chosen so that $K_s > M$.

Firstly, *forward smoothing* refers to the process of splitting the covariance matrix into P subarrays, which are averaged. P subarray matrices are summed up and divided by P as further explained in [2, p. 75-76].

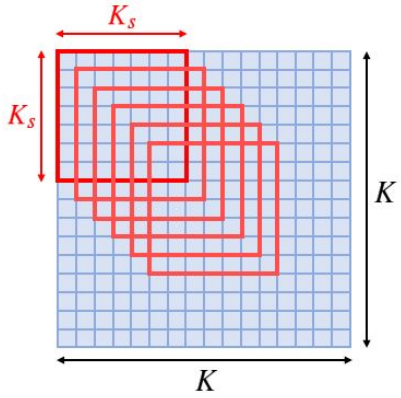

Figure 5.10: Subarray matrices (red) of dimension $K_s \times K_s$ to be averaged

Additionally, *backward smoothing* is applied as another kind of averaging elements of the matrix $\boldsymbol{R}$.
Backward smoothing is based on the assumption that we deal with a uniform linear area geometry. However, the condition is fulfilled as our signal data is sampled continuously with a constant interval Δf as defined in (3.14)

For backward smoothing, we exploit the persymmetrical structure of $\boldsymbol{R}$. A square matrix is called persymmetrical if its elements are mirrored along the northeast-to-southwest diagonal.

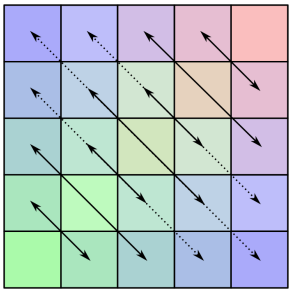

Figure 5.11: Demonstration of the symmetry of a persymmetrical matrix [10]

Taking into account the fact that the mirrored elements are supposed to be the same, we can take advantage of this specific structure. Hence we average these elements for backward smoothing, so that each mirrored pair is summed up and divided by two.
For a detailed description consider [2, p. 75-76] or [8, p. 168-170].

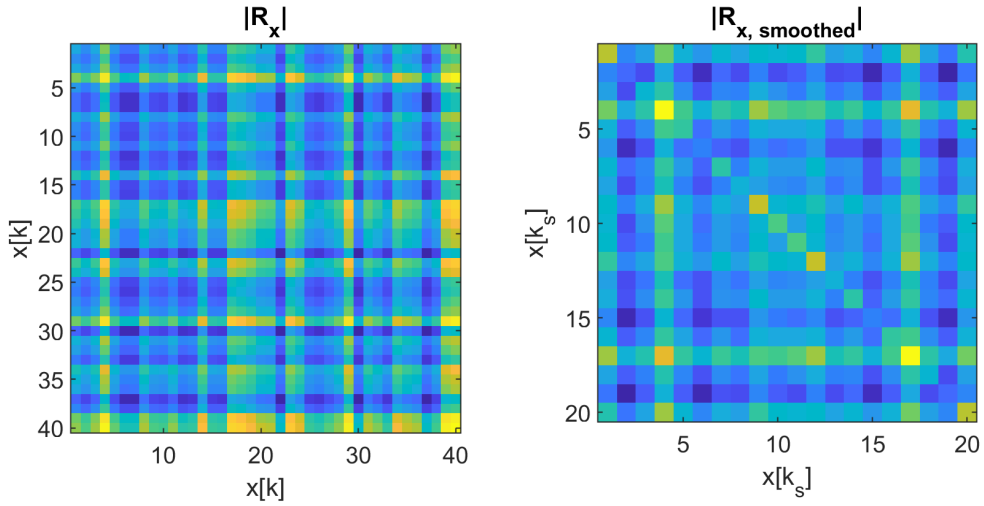

(a) without smoothing (b) with smoothing

Figure 5.12: Covariance matrix $\boldsymbol{R}$, $N_R = 1$, scenario 1

In figure 5.12, the covariance matrix $\boldsymbol{R}$ of one realization of scenario 1 is plotted with and without smoothing. We observe that considering the smoothed covariance matrix figure 5.12(b) covariance elements of the matrix are suppressed so that the main diagonal appears better visible. Additionally, the persymmetrical structure of backward smoothing is visible as well.
The effects of applying or omitting smoothing for different methods will be shown in the following section.

5.2.4 Properties of Estimates

5.2.4.1 Bias

In general, it is desired for the estimated value of any estimation method to be equal to the true value.
If this is not the case, the result is called *biased*, where the *bias* is the difference between the true value and the estimated value, and is used as relevant measure to evaluate any estimation approach.

The bias of the estimate $\widehat{\tau}$ of the parameter of interest τ [6, p. 290] is defined as

$$\widehat{b}(\tau) = \mathbb{E}\left[\widehat{\tau}\right] - \tau \tag{5.4}$$

Therefore, the estimate $\widehat{\tau}$ is *unbiased* if

$$\mathbb{E}\left[\widehat{\tau}\right] = \tau \tag{5.5}$$

Clearly, it is important to know if an estimate has a nonzero bias.

Note, that the performance of an estimator is preferably described statistically. Ideally, we would like to ensure that the estimator on the average produces the true value. In this case, we can call the estimation method unbiased.

5.2.4.2 Variance

Additionally, the *variance* is another relevant statistic measure to evaluate and further compare the performance of certain methods.
As described in [7, p. 15-18], looking for a good estimator also means to search for estimation methods with little variability.

$$var(\widehat{\tau}) = \mathbb{E}\left[\widehat{\tau}^2\right] - \mathbb{E}\left[\widehat{\tau}\right]^2 \tag{5.6}$$

If an estimate shows a high variance, it can take on a wide range of values and is not considered to be reliable for estimation. Hence a rather low variance is desired, as it implies a high probability that the estimated value will be close to the mean.

This also means, that unbiasedness alone does not necessarily guarantee a good performance of an estimator as it only ensures that on the average the true value is reached. The variation of the results could still remain high.
However, a biased estimator generally is a poor estimator as it shows a systematic error. A systematic error is strictly unrequested.
To conclude, we wish that most results of our estimation method are close to the true value. Ideally, we look for an unbiased estimator with a low variance.

5.2.4.3 Cramer-Rao lower bound

Assuming unbiasedness for now, we further wish to search for an estimator with minimum variance. A common way for estimation is to check whether there exists an estimator whose variance equals the Cramer-Rao lower bound (CRLB).
By definition, the variance of any estimator that is unbiased is greater or equal to a certain value described by the CRLB. Hence for the evaluation of various methods, it is helpful to have a look at the CRLB being the lower bound of the variance.

Therefore, we assume that the probability density function $p(\boldsymbol{x}, \tau)$ of $\boldsymbol{x}$ [7, p. 7] satisfies the following condition

$$\mathbb{E}\left[\frac{\partial \ln(p)(\boldsymbol{x}, \tau)}{\partial \tau}\right] = 0 \qquad \text{for all } \tau \tag{5.7}$$

where $\ln(p)(\boldsymbol{x}, \tau)\,\partial\tau$ is the log-likelihood function of $\boldsymbol{x}$ [7, p. 29]. We call it the *regularity condition*, a condition that ensures unbiasedness.
If the regularity condition is fulfilled, the CRLB is given by

$$var(\widehat{\tau}) \geq \frac{1}{-\mathbb{E}\left[\frac{\partial^2 \ln(p)(\boldsymbol{x}, \tau)}{\partial \tau^2}\right]} \tag{5.8}$$

where

$$-\mathbb{E}\left[\frac{\partial^2 \ln(p)\,(\boldsymbol{x},\tau)}{\partial \tau^2}\right] = I\,(\tau) \tag{5.9}$$

denotes the Fisher Information.

The definition of the CRLB allows us to compare the performance of any unbiased estimator against a reference bound. The best case is to find an estimator which always equals the CRLB, but if not, there also might be an estimator which converges to the bound under certain conditions.

To compare the performance of all delay estimation methods in relation to the SNR [dB], the Fisher Information defining the CRLB is found to be

$$I\,(\tau) = 8\pi^2\beta^2 N 10^{\frac{\mathrm{SNR}}{10}} \tag{5.10}$$

for the case of a single signal component in AWCGN, where β^2 is denoted the mean-squared bandwidth and can be obtained as

$$\beta^2 = \frac{B_0}{12} \tag{5.11}$$

For a detailed derivation of the particular case of one signal component and AWCGN leading to (5.10), we refer to [7, p. 524-531].

5.2.5 Evaluation of bias and standard deviation

To compare the performance of all methods the bias $\widehat{b}(\tau)$ is shown in dependency of the SNR in figure 5.13.
We view the standard deviation in figure 5.14, as a measure for the precision of the methods. The squared standard deviation equals the variance as

$$var(\widehat{\tau}) = \sigma^2 \tag{5.12}$$

Additionally, the CRLB is plotted in dependency of the SNR as a reference, determined from equation (5.10) as

$$\sigma_{\mathrm{CRLB}} = \sqrt{\frac{1}{8\pi^2\beta^2 N 10^{\frac{\mathrm{SNR}}{10}}}} \tag{5.13}$$

Furthermore, the prior describes the noninformative region [7, p. 332] and equals

$$\sigma_{\mathrm{prior}} = \sqrt{\frac{(d_{max} - d_{min})^2}{12}} \tag{5.14}$$

In figure 5.13 and figure 5.14 bias and standard deviation are evaluated for all estimation methods with and without smoothing. Methods applied without smoothing are indicated with dashed lines.

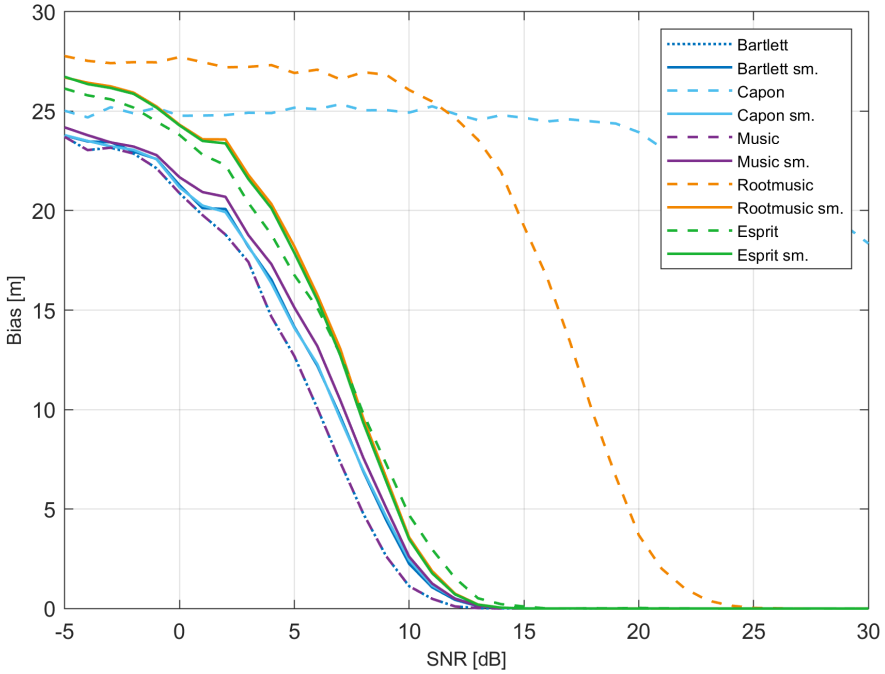

Figure 5.13: Bias of one-component-case

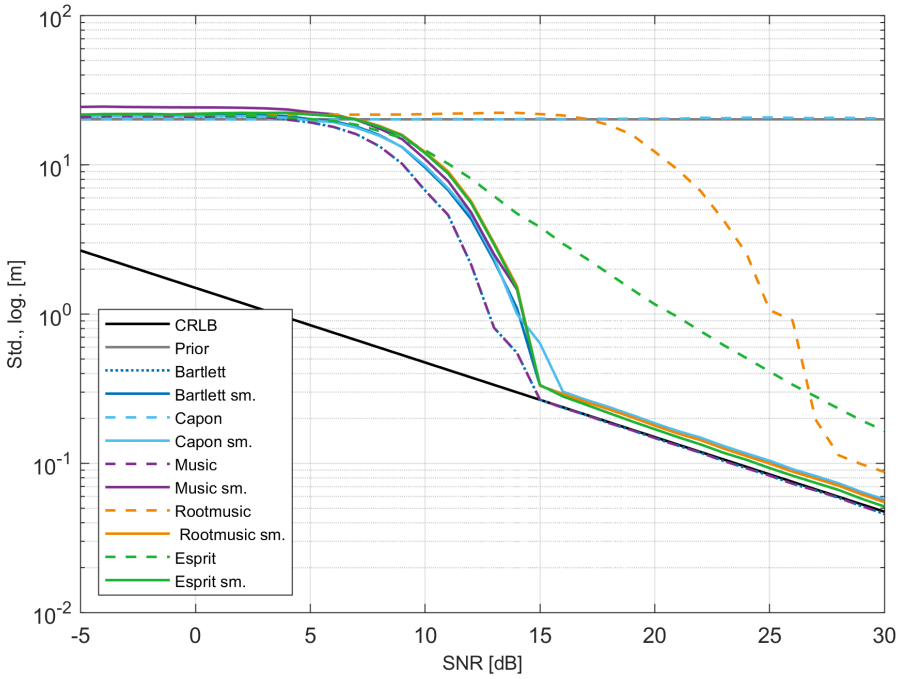

Figure 5.14: CRLB of one-component-case

For scenario 1, we generally expect estimation methods to become unbiased for high SNR in a similar manner as shown for the Bartlett and the Capon spectrum previously.
Furthermore, the standard deviation of each method should ideally reach the CRLB for high SNR.

In figure 5.13, the expectation is found to be confirmed. As discussed in section 5.2.2, this is achieved due to fact that there is no other influence present in this scenario except AWCGN. Nevertheless, there is one noticeable exception: As the Capon beamformer requires smoothing, the bias does not become zero for high SNR if applied without smoothing.
In the following section we will discuss each method separatly.

5.2.5.1 Performance of Bartlett

As shown in [6, p. 610], the Bartlett algorithm coincides with the ML estimation for the one-component case, which means that it must show the best performance considering standard deviation and therefore reach the CRLB. This can be seen in figure 5.14 for the Bartlett method when no smoothing is applied to the covariance matrix.

However, we notice that the Bartlett method with smoothing does not reach the CRLB determined from equation (5.13).
To understand this observation, note that smoothing can be interpreted as averaging over P subarrays. As discussed in section 5.2.3, it generates a matrix of smaller dimensions $K_s \times K_s$, which explains that the procedure lowers the bandwidth.
A loss of bandwidth is a negative impact specifically on the Bartlett method, as the broadness of the main lobe highly depends on the bandwidth. An extended bandwidth could narrow Bartlett's main lobe and help the approach to perform better. Contrary, a lower bandwidth causes a broader main lobe.

Moreover, as smoothing decreases the bandwidth, the CRLB from (5.13) is generally not suitable for methods applied with smoothing. As the CRLB in figure 5.14 is determined from the original bandwidth B_0 by (5.11), the CRLB for the smoothing case has to be expected as a bound slightly above the original CRLB for all methods.
This can be clearly observed in figure 5.14, which represents the standard deviation of an ideal scenario neglecting reflective components: All methods applied with smoothing do not reach the CRLB, but they do reach a conceivable limit slightly above.

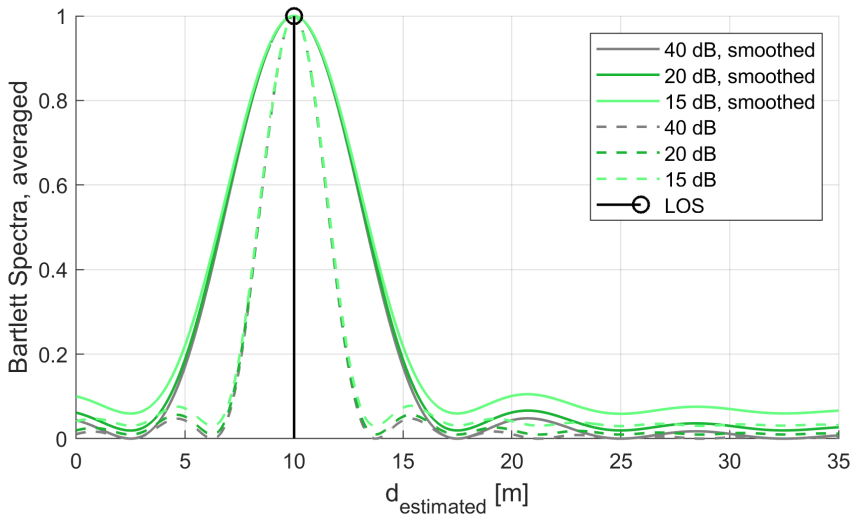

Figure 5.15: Bartlett Spectra with/without smoothing (averaged)

This clearly adds a negative aspect to the procedure of smoothing the covariance matrix. It tells us, that smoothing is not beneficial for methods which do not require smoothing necessarily, as especially for the Bartlett beamformer.

Figure 5.15 illustrates the difference of Bartlett spectra with and without smoothing, where the latter are marked with dashed lines. For smoothing, a smoothing factor K_s of 20 is chosen in figure 5.15. We see that the reduced bandwidth due to smoothing widens the main lobe significantly. This trend remains identical for different choices of the SNR.

5.2.5.2 Performance of Capon

As clearly seen in the evaluation of the bias in figure 5.13, the Capon approach requires smoothing.
The reason why smoothing is particularly essential for the Capon beamformer in our case, can be explained by its spectrum definition. The Capon spectrum is defined in equation (4.21) as

$$P_{\mathrm{C}}(\tau) = \frac{1}{\boldsymbol{b}(\tau)^{\mathrm{H}} \boldsymbol{R}^{-1} \boldsymbol{b}(\tau)}$$

The inversion of the covariance matrix leads to numerical issues in the Capon spectrum as $\boldsymbol{R}$ is rank deficient for $N = 1$ and thus cannot be inverted.

In figure 5.16, both covariance matrices from figure 5.12 were inverted. In figure 5.16(a) the original covariance matrix without smoothing is shown. In figure 5.16(b) we observe high values for variances in the main diagonal and comparably suppressed matrix elements elsewhere.

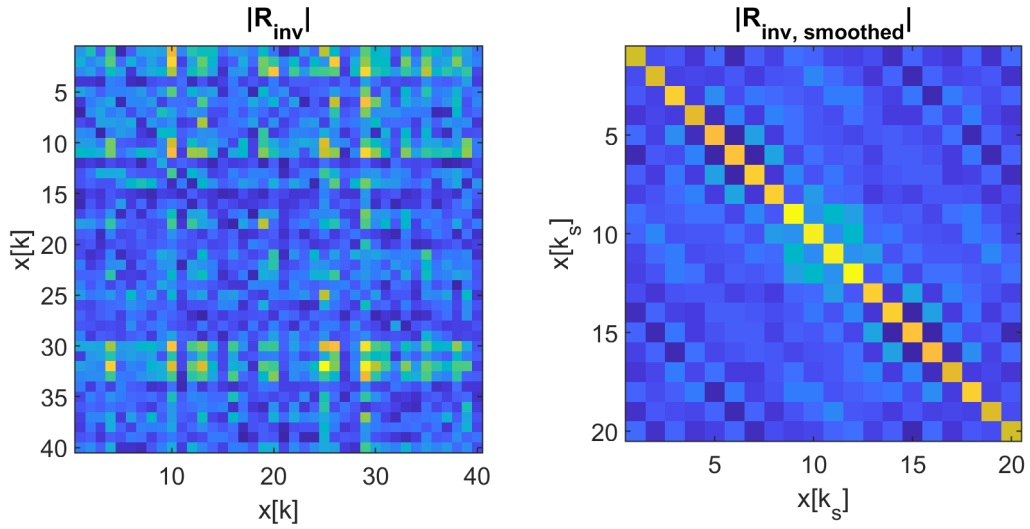

(a) without smoothing (b) with smoothing

Figure 5.16: Inverted covariance matrix $\boldsymbol{R}^{-1}$, $N_R = 1$, scenario 1

Numerical issues due to linear dependence result in random peaks arising in the spectrum. Figure 5.17 shows the Capon spectrum of the above plotted covariance matrices with and without smoothing for a high SNR of 40 dB. We clearly observe that omitting smoothing causes distinctive stability issues for the Capon beamformer.

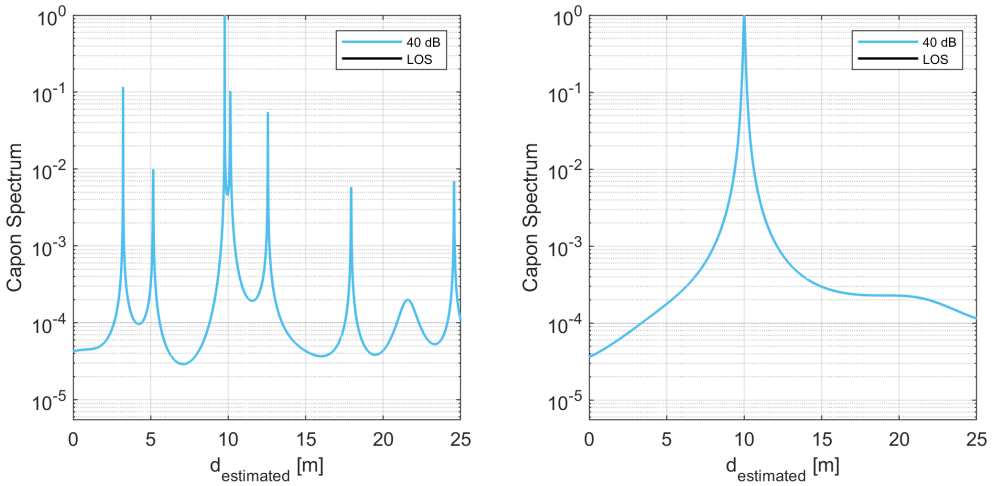

(a) without smoothing (b) with smoothing

Figure 5.17: Capon Spectra, $N_R = 1$

5.2.5.3 Performance of MUSIC

From literature [2, p. 74-76], the MUSIC approach is known for a downgraded performance in case of correlated signals. The method does not provide satisfying results for a correlated covariance matrix $\boldsymbol{R}$, thus smoothing is generally recommended.

The fact, that MUSIC also reaches the CRLB in figure 5.14 for the one-component-scenario might be surprising but can be explained due to the fact that there is only one signal component and perfectly uncorrelated noise in this scenario and $M = 1$ is perfectly selected.
For a better understanding, we also have a look at the statistically evaluated and averaged MUSIC spectrum without smoothing in comparison to the smoothed case in figure 5.8. In figure 5.18, one can obviously see the influence of smoothing considering the noise floor, but we further observe that the peak remains unbiased also without smoothing.

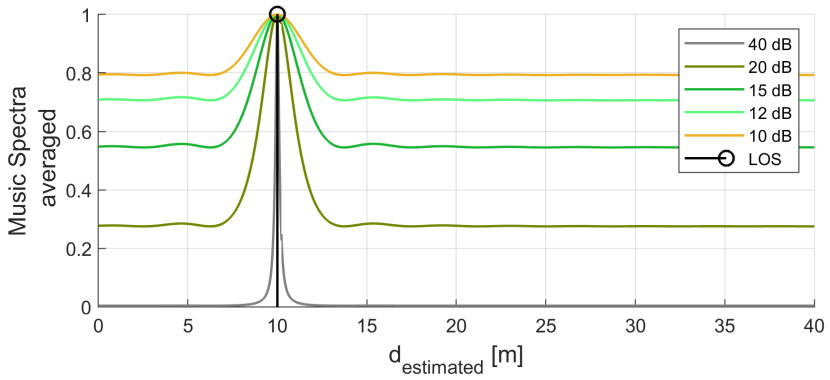

Figure 5.18: MUSIC Spectra without smoothing (averaged)

It confirms the observations in figure 5.13. The observation that the standard deviation in figure 5.14 appears to be better without smoothing for MUSIC for the rather theoretical case of

one signal component only, further is a consequence of the reduced bandwidth due to smoothing. Again, the impact of smoothing on lowering the bandwith must be taken into account.

5.2.5.4 ROOT-Music and ESPRIT

The ROOT-Music approach as well as the ESPRIT method are observed to perform significantly better when smoothing is applied to the covariance matrix. Even though ESPRIT becomes unbiased for low SNR without smoothing for the one-component case, it can be seen that both methods show worse results without smoothing considering the standard deviation.

Considering both methods with smoothing applied, we observe a slightly lower standard deviation for the ESPRIT approach.
As mentioned before, the CRLB describes a lower bound for the standard deviation, but does not correspond to the bound for methods applied with smoothing.
As clearly seen in figure 5.14, all estimators applied with smoothing converge to a bound slightly above, implying the reduced bandwidth.

5.3 Scenario 2 - Two components: Variation of SNR

In this scenario we consider two signal components.
The first signal component is defined to be the LOS component. As in scenario 1, the time delay τ_1 of the LOS component corresponds to a direct distance of 10 m. The second signal component is added as a reflected component. The time delay τ_2 of the reflected component is longer because the propagation path of the wave is longer. Therefore, τ_2 is chosen corresponding to a distance d of 12 m. Hence the distance between the LOS component and the reflection $d_{\Delta 12}$ is defined to be 2 m.
In real life situations, a reflection might be caused by a wall or other reflective objects near by.

Parameters	Symbol	Scenario 2
Signal-to-noise ratio	SNR	to be varied

Table 5.3: Parameter variation in scenario 2

From now on, we consider all methods with smoothing applied to the covariance matrix, except the Bartlett beamformer. Bartlett is handled as an exception, as smoothing is not fundamentally required for the method.
In section 5.2.3, we observed that the impact of smoothing is rather negative for the Bartlett spectrum due to the reduction of the bandwidth. Hence a consideration of the Bartlett beamformer to other methods with smoothing applied would be a rather unfair comparison.
Considering computational power, it is also beneficial that smoothing is not needed for the implementation of Bartlett beamforming.

5.3.1 Separation of components in spectrum-forming methods

In figure 5.19 a second reflective component is plotted in grey.
We consider a so-called *LOS scenario*, with a reflection of a lower gain than the LOS component. As defined in table 5.1 by default, the reflection has a gain of 0.75, while the LOS gain is 1.
In real life situations, any reflections caused by a wall or other reflective objects near by refer to a LOS scenario.

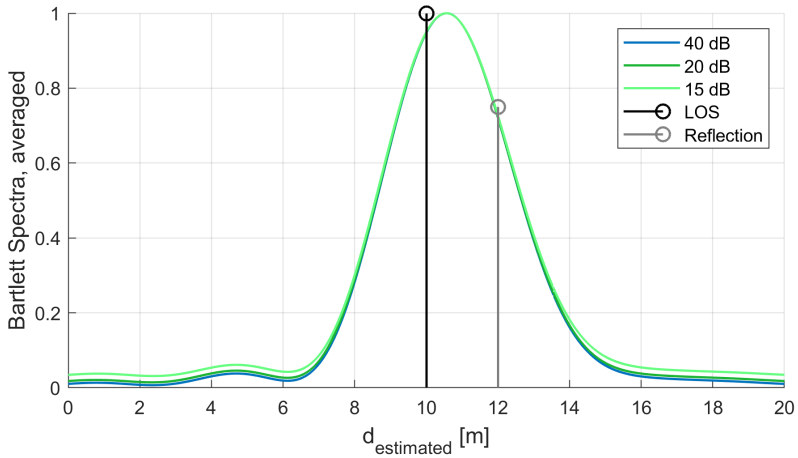

Figure 5.19: Bartlett Spectra, two components (averaged)

It is a relevant observation, that the broad main lobe of the Bartlett spectrum fails to separate the two signal components on average. The bandwidth of 78 MHz for BT is not adequate for splitting two signal sources occuring in a distance of 2 m from each other.
When dealing with a sufficient bandwidth, we expect the Bartlett spectrum to form a beam at each time delay τ. In our case, peaks should ideally be detected at 10 m and 12 m. However, superposition occurs for multiple signal components as the spectra of each component superimpose with each other. Therefore, accurate separation of single components is hindered by the broadness of the main lobe.

In contrast, we expect the Capon method to perform better considering the case of two or more signal components sensed at the receiver, due to its comparably narrow main lobe.
Plotting Capon spectra of different SNR in figure 5.20, we see the expectation confirmed. For a high SNR of 40 dB, the Capon beamformer succeeds to separate both signal components for a $d_{\Delta 12}$ of 2 m, although the method does not separate the components for a rather low SNR of 20 dB.

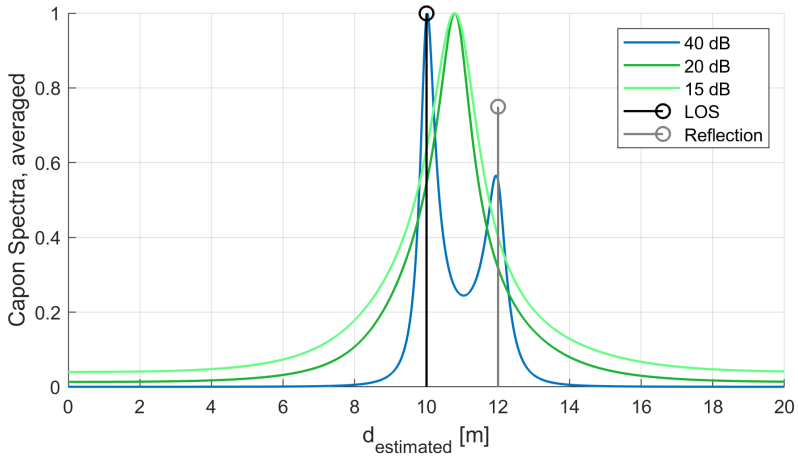

Figure 5.20: Capon Spectra, two components (averaged)

The attempt of the Capon method to alleviate the limitations of the Bartlett beamformer (see section 5.2.1.2 and [2, p. 73-74]), is achieved by considering and minimizing any other interference with the covariance matrix $\boldsymbol{R}$ included in the weight vector $\boldsymbol{w}_C$ from (4.20)

$$\boldsymbol{w}_C = \frac{1}{\boldsymbol{b}(\tau)^{\mathrm{H}} \boldsymbol{R}^{-1} \boldsymbol{b}(\tau)} \boldsymbol{R}^{-1} \boldsymbol{b}(\tau)$$

Since the covariance matrix is considered in the weight vector, the method gains a better noise suppression capability for correlation of the data. In contrast, the Bartlett method with its weight vector $\boldsymbol{w}_B$ from (4.11) does not consider the covariance matrix.

$$\boldsymbol{w}_B = \|\boldsymbol{b}(\tau)\|^{-2} \boldsymbol{b}(\tau)$$

Adding the MUSIC pseudospectrum to the comparison of all three spectrum-forming methods for a high SNR of 40 dB, we observe that both the Capon and the MUSIC method clearly outperform the Bartlett method in figure 5.21. Both spectra manage to separate the signal sources, in contrast to the Bartlett beamformer. As introduced in figure 5.14, the Bartlett spectrum is plotted with a dashed line implying that smoothing is not applied.

The results of the parametric methods ROOT-Music and ESPRIT were statistically evaluated as well. As they do not form a spectrum, the mean value of the estimated distance is plotted instead. The mean was evaluated over 10000 realizations and equals the LOS in figure 5.21. Hence both methods appear to be unbiased on average.

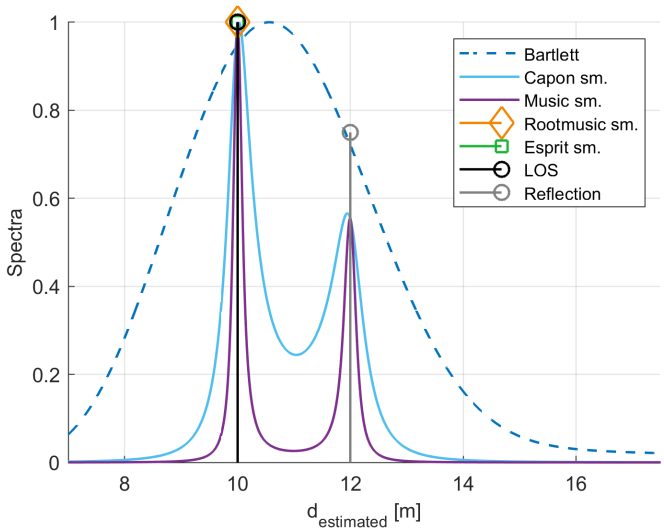

Figure 5.21: Two components, SNR = 40 dB (averaged)

Next, we compare the different estimation approaches also for lower SNR values, for instance for 25 dB in figure 5.22, and even for 20 dB respectively in figure 5.23. The plots show that Capon is biased for an SNR of 25 or 20 dB and cannot separate the signal components either.

Considering the averaged pseudospectrum of MUSIC, we further see that for an SNR of 25 dB the method shows slightly biased results. For an even lower SNR of 20 dB also MUSIC fails to distinguish both components as noise severely impacts the estimation results. The methods Root-MUSIC and ESPRIT show a bias in figure 5.23 as well.

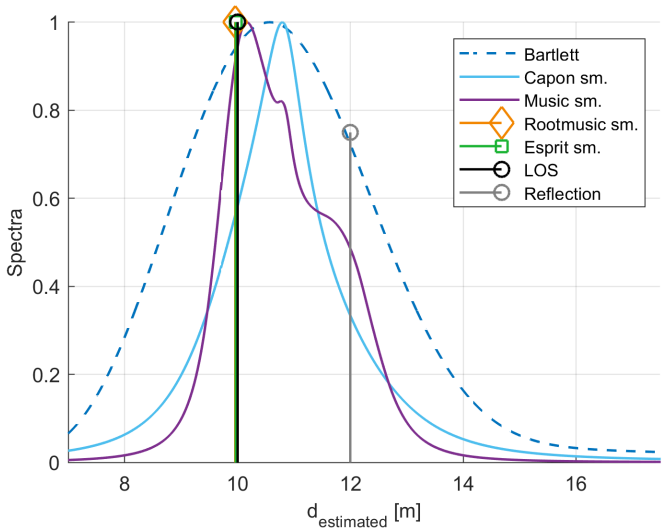

Figure 5.22: Two components, SNR = 25 dB (averaged)

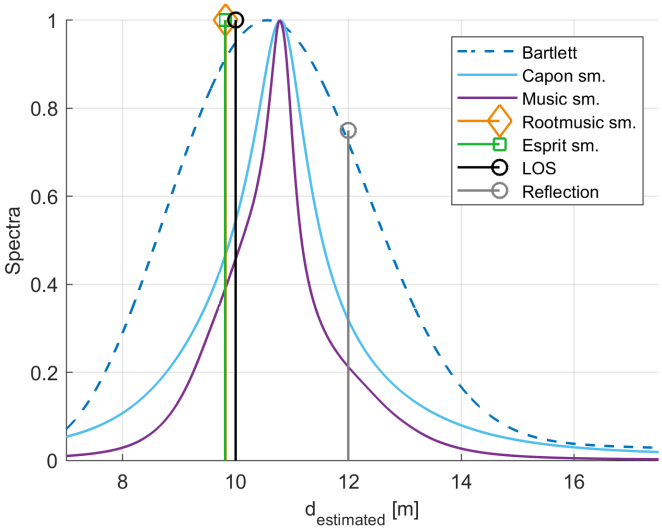

Figure 5.23: Two components, SNR = 20 dB (averaged)

5.3.2 Bias and standard deviation

In figures 5.24 and 5.25 the bias and the standard deviation are plotted for scenario 2. The results of all estimation methods are evaluated in dependency of the SNR to observe which approach reaches unbiasedness for lower SNR values. We consider SNR values from -5 to 45 dB.

Considering the bias in figure 5.24, we observe that the Bartlett method remains biased for high SNR. As seen in the figures 5.21, 5.22 and 5.23, the Bartlett spectrum fails to separate two signal components with $d_{\Delta 12} = 2m$. Instead of estimating the distance of the LOS component $d_1 = 10m$, a peak between the distance 10 m and 12 m is detected.

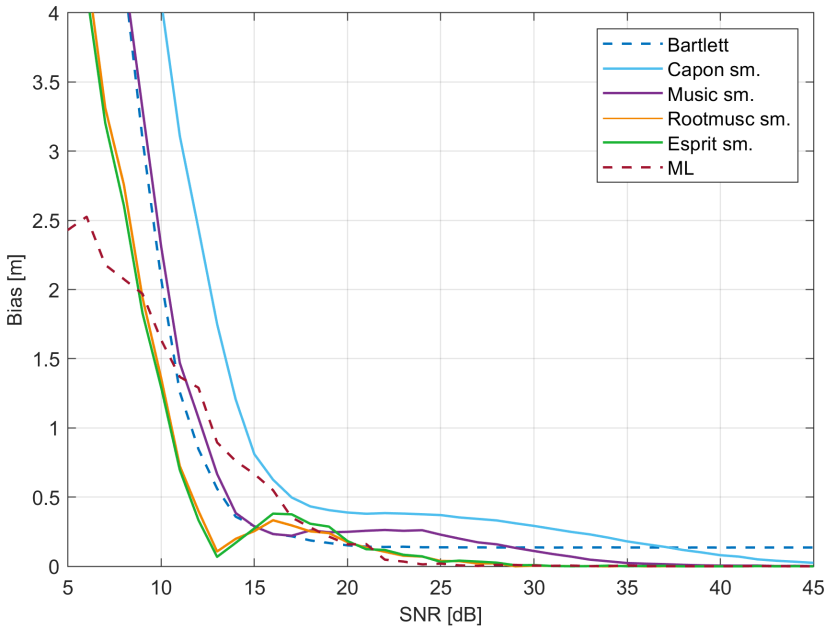

Figure 5.24: Bias of two-component-case ($d_{\Delta 12} = 2m$)

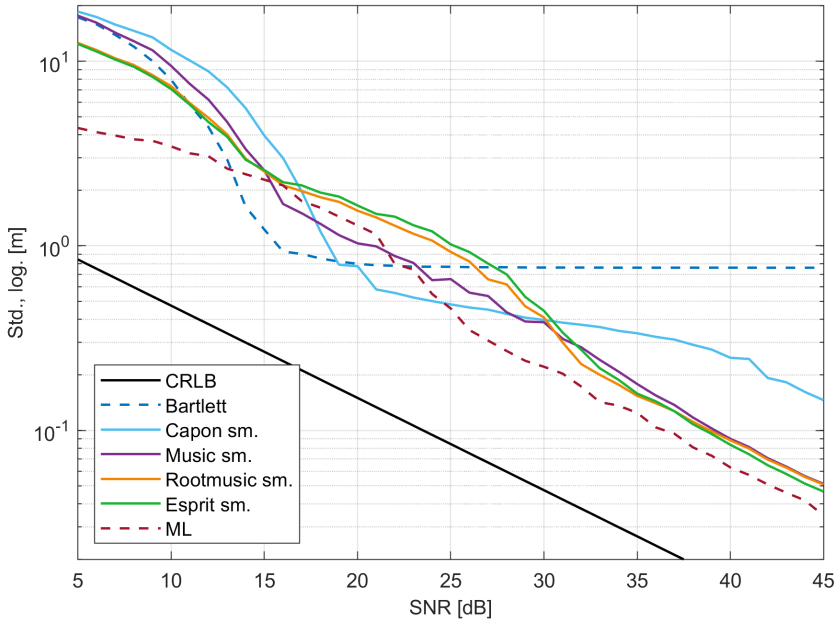

Figure 5.25: Standard deviation of two-component-case ($d_{\Delta 12} = 2m$)

5.3.3 Model order

For the evaluation of the model-based methods MUSIC, Root-MUSIC and ESPRIT, we need to consider an important matter for practical application.
As already mentioned in section 5.2.1.3, these methods require the knowledge of the model order, i.e. the number of signal components M. It is responsible for the procedure of splitting the measurement data into a signal and a noise subspace.
In other words, for the application of parametric approaches we need to know how many eigenvalues and eigenvectors actually belong to the signal subspace. In simulation, this problem is not present, as the number of signal components is known from the choice of the signal vector $\boldsymbol{x}$, and the known model order can be used appropriately for MUSIC, Root-MUSIC and ESPRIT. In real life situations, the number of signal components M depends on the environment and is unknown. The surroundings of the present situation is responsible for the occuring reflections. Therefore, the model order needs to be chosen by experience or further optimization algorithms need to be considered.

A more detailed discussion about the choice of the model order in real life situations will follow in section 6.1.3, with an evaluation of the estimation methods using test measurements.
However, the performance of model-based methods is generally highly dependent on the right choice of the model order, which needs to be considered for the simulation results in figure 5.24 and figure 5.25.

5.3.4 The choice of the smoothing factor

For smoothing, a smoothing factor of 20 was chosen in the considered estimation scenarios.
In the current scenario, the bias was also plotted in dependency of the smoothing factor. Con-

sidering a number of frequencies $K = 40$, the smoothing factor K_s was chosen in relation to K, from $K_s = 10$ to $K_s = 40$, where $K_s = K = 40$ implies that no smoothing is applied.
Figure 5.26 shows the bias plotted as a function of K_s, with the condition $K_s > M$ being fulfilled.

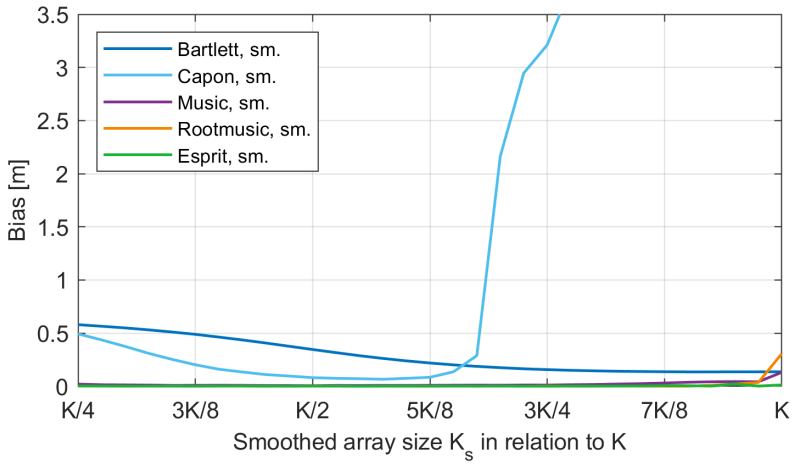

Figure 5.26: Bias in dependency of the smoothing factor K_s, SNR = 40 dB

The smoothing factor mostly impacts the Capon beamformer due to its stability issues caused by the inversion of the covariance matrix $\boldsymbol{R}$ (see section 5.2.5.2). Hence the right choice of the smoothing factor is essential for the calculation of the Capon spectrum.
It is seen that the bias of the Capon method depends strongly on the smoothing factor, with little dependence observed for all other methods.
For a bigger smoothed array size K_s, the decorrelation through smoothing is not sufficient, so that Capon remains biased. In scenario 2, this happens for $K_s > 5K/8$.
At the same time, a very small smoothed array size $K_s < 3K/8$ would also downgrade the estimation results as the bandwidth is extremly reduced in this case.

Considering the remaining methods, the choice of smoothing factor was found to have only little or no impact on the results. The dependency on the smoothing factor can be observed even better in the plot of the standard deviation in figure 5.27.

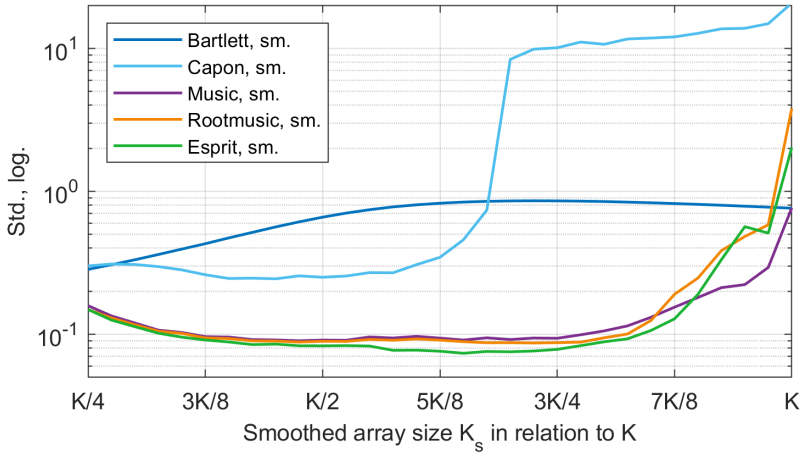

Figure 5.27: Standard deviation in dependency of the smoothing factor

To conclude, a smoothing factor in a range of about $K/2$ to $5K/8$ was found best for the considered scenario.

For the sake of completeness, the Bartlett beamformer is also evaluated with smoothing in dependency of the smoothing factor. As expected, smoothing has a worse impact on the Bartlett beamformer due to the reduction of the bandwidth. The bias of the Bartlett method increases for lower values of K_s.
However, the method does not require smoothing and hence is considered without smoothing in the simulation scenarios.

5.4 Scenario 3 - Two components: Variation of inter-component distance

In this scenario the aim is to analyze cases with two signal components in various distances to each other. Therefore, the distance $d_{\Delta 12}$ between the LOS component and the reflected component is varied.
We wish to find out for which distance limit of closely-spaced components estimation methods can still succeed in estimating the LOS.

Parameters	Symbol	Scenario 3
Number of signal components	M	2
Distance of LOS component	d_1	10 m
Distance of reflected component	d_2	to be varied
Distance between components	$d_{\Delta 12}$	to be varied

Table 5.4: Signal parameters for scenario 3

In figures 5.28 and 5.29, the bias and the standard deviation are plotted similar to scenario 2 but for inter-component distances $d_{\Delta 12}2.5m$ and $d_{\Delta 12}2.5m$. This first approach of slightly increasing and decreasing $d_{\Delta 12}$ shows a similar trend compared to the results in section 5.3.
For $d_{\Delta 12} = 1.5m$, we observe that Root-MUSIC and ESPRIT remain unbiased for an SNR of about 35 dB.
For $d_{\Delta 12} = 2.5m$, the Bartlett beamformer still remains biased. Furthermore, the reason why the Bartlett actually has a larger bias for closely-spaced signals of $d_{\Delta 12} = 2.5m$ will be discussed in section 5.4.1.

Another interesting observation is that the methods Root-MUSIC and ESPRIT seem to perform sligthly worse for rather low SNR values of about 20 dB, specifically for $d_{\Delta 12} = 1.5m$ in figure 5.28(b).
Even though the remaining methods are not unbiased, their bias is noticeably smaller for low SNR. For instance, for $SNR = 20dB$ the Bartlett method is biased in figure 5.28(b), but its bias consistently remains the same. As Bartlett gives us real representation of the signal information by transformation, the bias is always defined by the superposition of both components.
It shows us that ROOT-Music and ESPRIT are strongly influenced by the noise as well. However, the increase of their bias from 14 to 19 dB in figure 5.28(b) might also be caused by a higher standard deviation for low SNR, as seen in figure 5.29(b). Potentially, a higher number of realization might flatten the curve of their bias in figure 5.28(b).

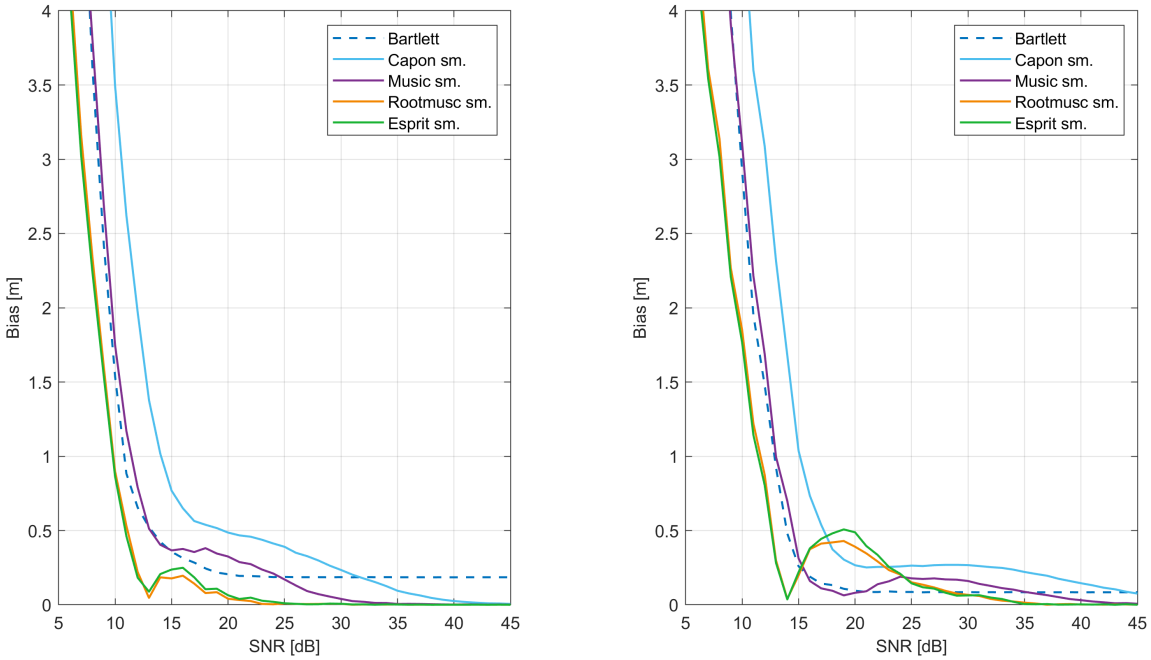

(a) $d_{\Delta 12} = 2.5m$ (b) $d_{\Delta 12} = 1.5m$

Figure 5.28: Bias for two components with different $d_{\Delta 12}$

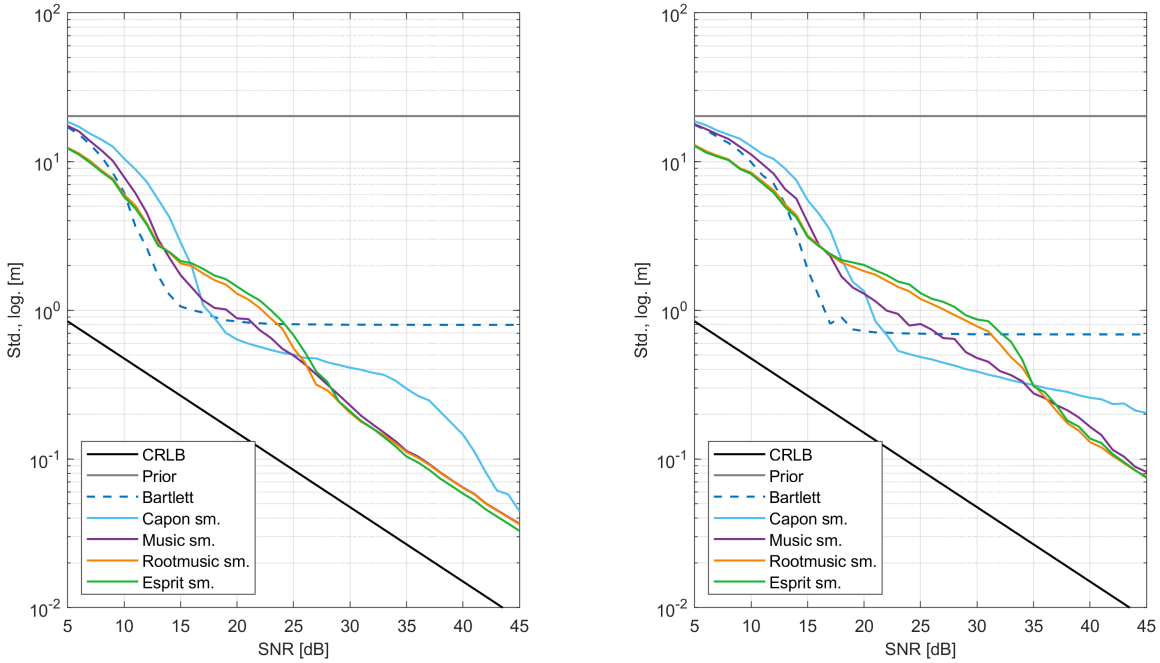

(a) $d_{\Delta 12} = 2.5m$ (b) $d_{\Delta 12} = 1.5m$

Figure 5.29: Standard deviation for two components with different $d_{\Delta 12}$

5.4.1 Evaluation in dependency of $d_{\Delta 12}$

For a better insight, the estimators are further evaluated in dependency of the distance $d_{\Delta 12}$. The results of bias and standard deviation as a function of $d_{\Delta 12}$ are plotted in figure 5.30 and 5.31, the x-axis shows values of $d_{\Delta 12}$ up to 7 m. A high SNR of 40 dB is chosen for this test. As in scenario 2, the gain of the reflective component is 75% of the LOS gain.

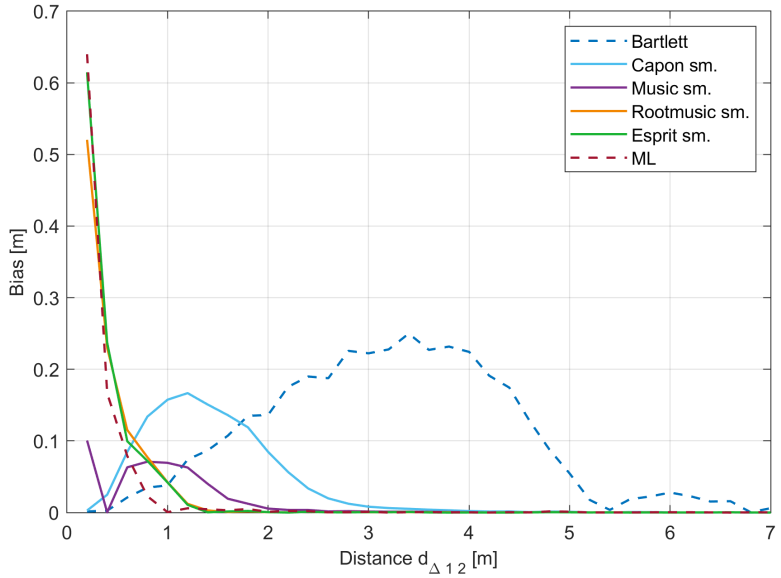

Figure 5.30: Bias in dependency of $d_{\Delta 12}$

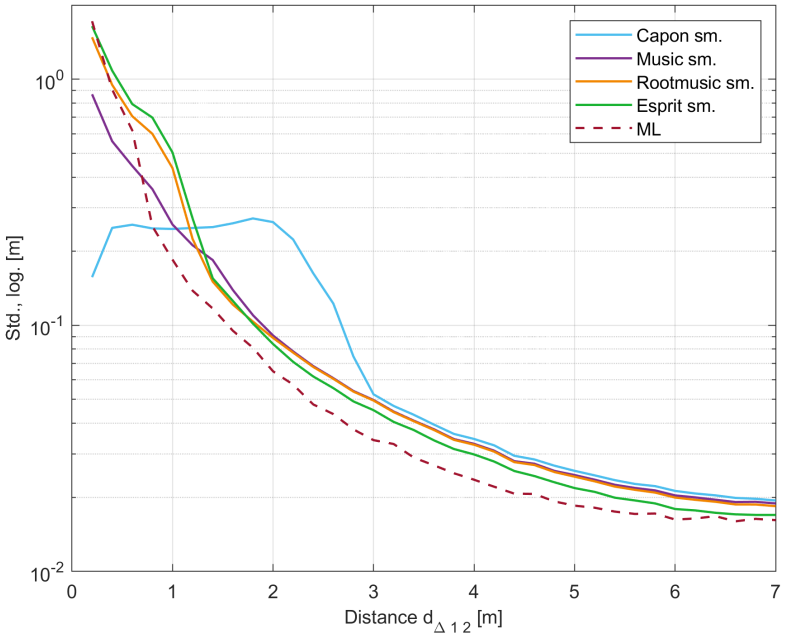

Figure 5.31: Standard deviation in dependency of $d_{\Delta 12}$

In figure 5.30, we clearly observe the outperformance of the ML estimator.

Further, Root-MUSIC and ESPRIT show a better performance than MUSIC. Both methods succeed to detect the LOS component statistically unbiased for distances $d_{\Delta 12} \leq 1.3m$. Again, ESPRIT performs slightly better considering standard deviation.

Another observation might be irritating at first, when looking at the bias in figure 5.30. In general, we would expect worse results for smaller distances $d_{\Delta 12}$, as closer spaced components influence each other. However, the smaller $d_{\Delta 12}$ gets, the more the bias increases at first, but it also decreases for even smaller $d_{\Delta 12}$ considering Bartlett, Capon and MUSIC.

The observation that the bias decreases for components close together for beamforming methods may be explained as follows.
From previous results we know, that for small $d_{\Delta 12}$ the peak is falsely detected between both signal components, as beamforming approaches fail to separate the signal components in the spectrum. Moving the components closer together results in a smaller bias, though these methods still detect a peak in between both components, instead of correctly detecting the LOS. It can be mistaken that the bias decreases, but in fact it just moves with the influence of the reflective component.
Hence both beamforming approaches cannot become unbiased in this case. For example, the bias is always present for the Capon method for $d_{\Delta 12} \leq 3m$.

It exemplarily shows the limitation of spectral-based methods to separate peaks at a certain distance $d_{\Delta 12}$. For the Bartlett beamformer, the result is biased due to the influence of the second component already for large distances $d_{\Delta 12}$. The bias increases up to the point that the influence of the reflective component is so strong that the method fails to separate both components in the spectrum and simply forms a single beam right between both components. Moving the components further and further together, the bias decreases. However the bias remains present and the peak is detected incorrectly as a peak arising from the superposition of both components.

This observation is visualized in figure 5.32 considering the Bartlett method. Averaged Bartlett spectra are plotted with reflective components in various distances $d_{\Delta 12}$ of 0.4 m, 1.2 m and 2 m from the LOS component.

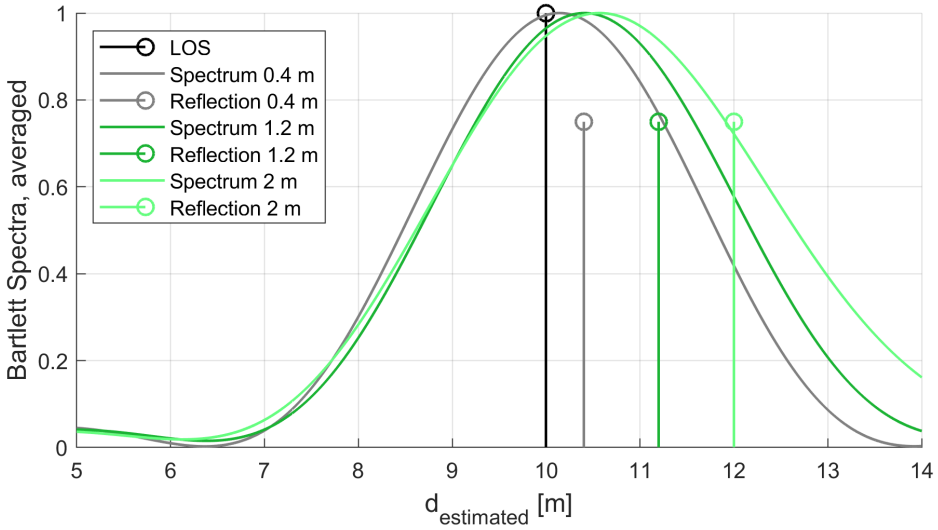

Figure 5.32: Bartlett Spectra for different $d_{\Delta 12}$ (averaged)

5.5 Scenario 4 - Two components: Variation of the LOS gain

Scenario 4 is an attempt to vary the gain of the LOS component and evaluate its influence.
In scenario 2 and 3 the gain of the reflective component was chosen to be 75% of the LOS gain, however, now we also wish to consider situations of a lower LOS gain.

Therefore, we simply decrease the gain of the LOS component in the simulations.
An example, that the LOS gain is actually lower than a reflective component is the so-called *back pocket case*. As the name implies, it refers to the situation of the user having the car key in his back pocket, so that the amplitude of the direct signal is reduced due to the impact of the human body.

Parameters	Symbol	Scenario 4
Number of signal components	M	2
Magnitude of LOS component	A_1	to be varied
Magnitude of reflected component	A_2	1

Table 5.5: Parameters for scenario 4

5.5.1 The peak searching approach

Bartlett, Capon and MUSIC require peak searching techniques to find the correct peaks of the received spectrum. In LOS scenarios with larger LOS gain it is sufficient to search for the maximum in the spectrum as the maximum peak usually corresponds to the LOS component. However, in this scenario it is not guaranteed that the LOS component automatically has the largest gain and therefore belongs to the maximum peak.
Therefore, it is more convenient to search for the *first peak*. As we wish to find the direct distance, we want to determine τ_1, which is the first sensed signal at the receiver and therefore corresponds to the first peak of the spectrum.

However, in practical application the first peak of the spectrum is often not the peak of the first beam corresponding to a signal component, but can also arise from noise or sidelobes, as well as from superposition of both. Hence a peak search technique is required which finds the first dominant peak above a so-called *noise floor*. Talking about the so-called noise floor, it is mainly dependent on the SNR but can also be influenced by side lobes of the spectrum due to superposition.
For the simulation, a peak searching method was applied which evaluates the noise floor first, multiplies it by a certain factor and from that defines a threshold.

This factor is chosen heuristically. It is needed since the evaluated noise floor increases at positions closer to signal components due to superposition with side lobes. Further, the multiplication factor is different for each method, as their spectrum characteristic is very different considering side lobes. While the Bartlett method generally forms side lobes in its spectrum, peaks in the MUSIC spectrum are not nearly as dominant.
The peak searching method searches for the maximum peak at first, but then analyzes the part of the spectrum before the maximum whether there is another peak which exceeds the threshold.

Estimation method	Smoothing	Multiplication factor for threshold
Bartlett	not applied	1e7
Capon	applied	2e4
MUSIC	applied	1.4

Table 5.6: Multiplication factors for the threshold of the peak searching approach

The peak searching technique was applied in all scenarios, though it becomes essential now for the evaluation of scenario 4.

5.5.2 Bias and standard deviation

We wish to find out whether the LOS component can be detected, if its gain A_1 is lower than the gain of the reflective component A_2.
Therefore, we define $A_{\Delta 12}$ to be the difference of the LOS gain A_1 and the gain of the second component A_2

$$A_{\Delta 12} = A_1 - A_2, \tag{5.15}$$

so that $A_{\Delta 12} > 0$ implies a larger LOS gain $A_1 > A_2$. Further, we choose the gain of the reflective component A_2 to be 1 and to be fixed while the values of A_1 are varied. The distance $d_{\Delta 12}$ between the components is 2 m for scenario 4.

For an evaluation that shows the impact of the LOS component gain A_1 for different estimation methods, the bias and the standard deviation were plotted as a function of $A_{\Delta 12}$.

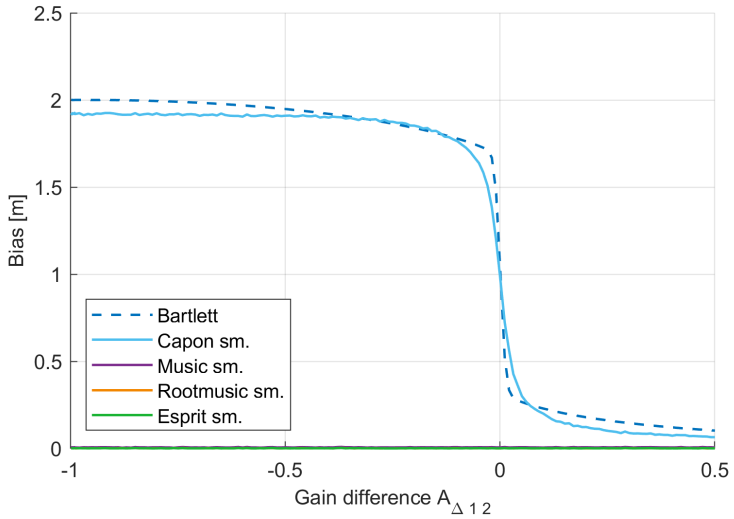

Figure 5.33: Bias in dependency of $A_{\Delta 12}$

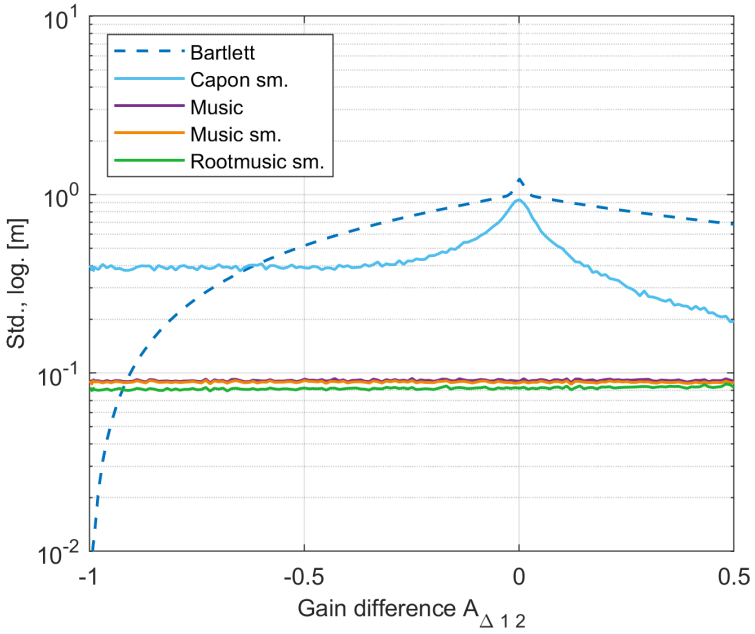

Figure 5.34: Standard deviation in dependency of $A_{\Delta 12}$

As we already know, the Bartlett beamformer fails to seperate signal components for $d_{\Delta 12} = 2m$ and remains biased. Consequently, it is not surprising that Bartlett is biased for any $A_{\Delta 12}$ in this evaluation as well.
However, the bias of the Bartlett meethod changes for a lower LOS gain. As seen in figure 5.33, the method shows a large bias for $A_{\Delta 12} < 0$, implying a LOS gain lower than the gain of the second component.

Especially for cases of $A_{\Delta 12} \leq -0.85$ the bias of the Bartlett beamformer is found to be as large as about 2 m. A gain difference of $A_{\Delta 12} = -0.85$ means the LOS gain A_1 equals 0.15, as $A_1 = A_2 + A_{\Delta 12} = 0.15$, with the gain of the reflective component being 1 in this evaluation scenario by definition.
Now considering that the LOS gain $A_{12} \leq 0.15$, we observe that the bias of 2 m equals the distance $d_{\Delta 12}$, simply implying that the Bartlett beamformer detects the second component instead of the LOS.
We further observe, that Bartlett generally detects second component with a larger gain for all $A_{\Delta 12} < 0$. As the method cannot separate both components, it detects the more dominant component. For the rather theoretical case of $A_{\Delta 12} = 0$, meaning that both components have the same gain, the bias of the Bartlett beamformer is exactly 1 m, as the spectrum forms the beam in the middle of both components. For a LOS gain larger than the reflective gain, the Bartlett beamformer shows a significantly lower bias, as the LOS component is domanint here, but still the method remains biased.
Considering the standard deviation in figure 5.34, it shows an increasing trend for the Bartlett beamformer up to $A_{\Delta 12} = 0$. The largest standard deviation occurs for $A_{\Delta 12} = 0$ due to the reason that both gains are equal and the algorithm occasionally detects peaks corresponding to the first or the second component for random noise realizations.

The second considered beamforming approach, the Capon beamformer, shows a similar tendency as Bartlett, considering its bias as well as its standard deviation. We gain optimal results from MUSIC, Root-MUSIC and ESPRIT specifically showing the lowest standard deviation.
It is not surprising that the parametric approaches show very good results for scenario 4. Ac-

tually, the issue of the model order needs a to be respected for this case as well. The optimal performance of both methods also results from the fact, that the model order is known in the simulation.

5.5.3 Pertinence of the peak searching approach

Since a high SNR of 40 dB was considered in section 5.5.2, one could expect a much better performance of the Capon method compared to Bartlett due to its narrow main lobe. The plots of averaged spectra in figure 5.35 and 5.36 provide a better insight.

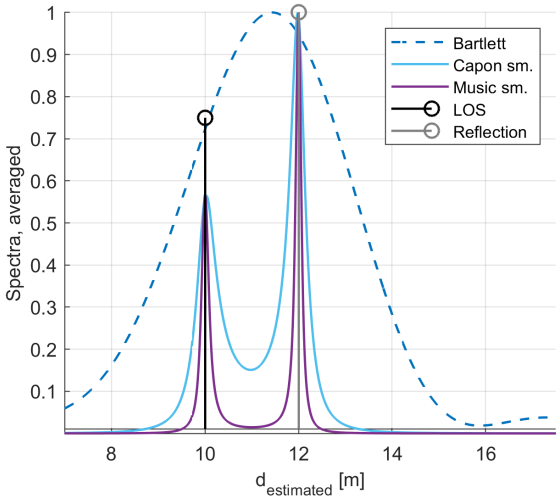

Figure 5.35: Spectra for $A_1 = 0.75$ and $A_2 = 1$

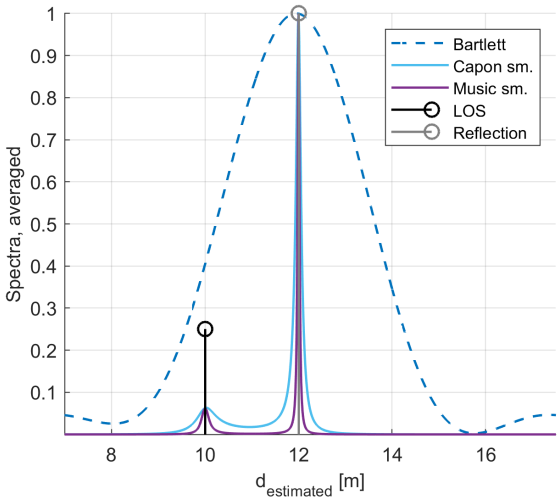

Figure 5.36: Spectra for $A_1 = 0.25$ and $A_2 = 1$

Considering the spectra in figure 5.36, we would expect the Capon algorithm to perform nearly as good as MUSIC. The main difference considering the averaged spectra in figure 5.35 and figure 5.36 compared to the results in section 5.5.2 is the impact of the peak searching method.

In figure 5.36, the averaged spectra are viewed, however, in figure 5.33 and figure 5.34, the influence of the peak detection approach is included. While for MUSIC, the peak detection operates satisfyingly in cases of very low LOS gains, the peak detection does not work as precisely for Capon.
For the Capon beamformer, the influence of the noise floor is generally higher, as seen in single realizations of the Capon and the MUSIC spectrum in section 5.2.1. Hence the threshold has to be set higher as well. Therefore, the MUSIC algorithm can evaluate lower LOS gains due to its ability to suppress the noise floor.

5.6 Scenario 5 - Diffuse Multipath

In scenario 5, we consider the *double exponential model* of the Diffuse Multipath (DM) [11, p. 3028–3037], [12]. Therefore, the signal model in section 3 is altered, thus scenario 5 must be handled as an exception in this work.

Parameters	Symbol	Scenario 5
Signal-to-interference ratio	K_{LOS}	to be varied
Rise time	γ_{rise}	5 ns
Fall time	γ_1	20 ns
Shape parameter	χ	1

Table 5.7: Parameters of the double exponential model of the DM

The DM describes the interference through multipath components and is modelled statistically. Therefore, the noise part $\boldsymbol{n}$ of the signal model in (3.26) is redefined as

$$\boldsymbol{n} = \boldsymbol{v} + \boldsymbol{w}\,, \tag{5.16}$$

where $\boldsymbol{w}$ is AWCGN, while $\boldsymbol{v}$ describes the DM, and thus is not *white*

$$\boldsymbol{n} \sim \mathcal{CN}\left(\boldsymbol{0}, \boldsymbol{C}\right) \tag{5.17}$$

with

$$\boldsymbol{C} \neq \sigma^2 \boldsymbol{I} \tag{5.18}$$

Note that reflected components are modelled as a stochastic process $\boldsymbol{v}(t)$, thus we consider only the LOS component and DM, implying that $M = 1$.
Further, $\boldsymbol{C}$ can be shown to be

$$\boldsymbol{C} = \mathbb{E}\left[\boldsymbol{n}\boldsymbol{n}^{\mathrm{H}}\right] = \int \boldsymbol{b}(\boldsymbol{\tau})\boldsymbol{b}(\boldsymbol{\tau})^{\mathrm{H}} S_v\left(\tau - \tau_1\right) d\tau + \sigma^2 \boldsymbol{I} \tag{5.19}$$

where S_v is the Power Delay Profile (PDP) of the DM.
In real life situations, DM components might occur from multiple reflections caused by the environment, f.e. in a closed room or a garage.

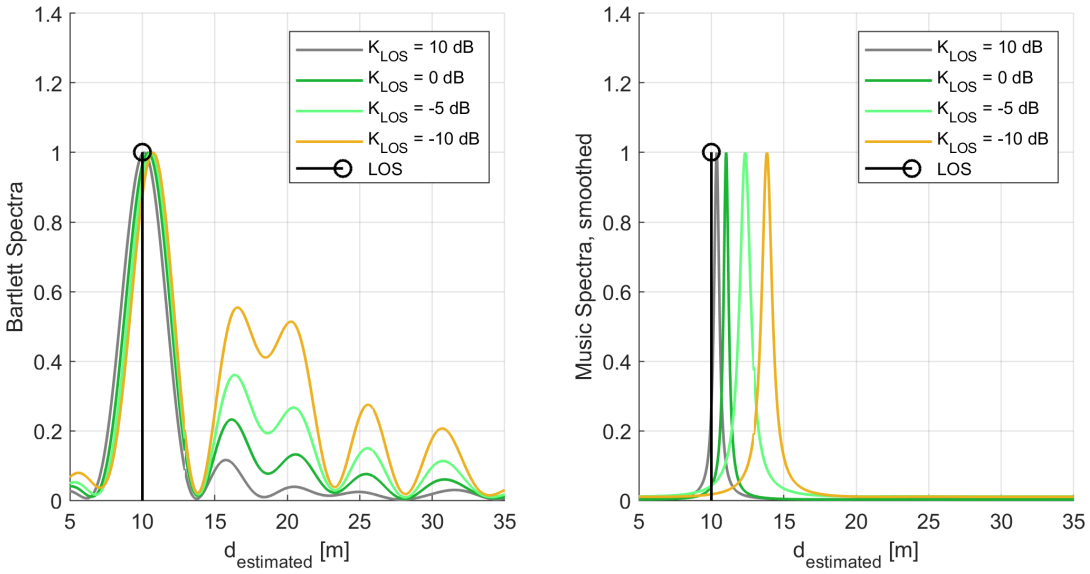

(a) Bartlett spectra (b) MUSIC spectra

Figure 5.37: LOS component with DM, $N_R = 1$

In figure 5.37(a) we observe different Bartlett spectra, where K_{LOS} corresponds to the signal-to-interference ratio of the DM. In this plot, a random noise realization was chosen and plotted ($N_R = 1$). In figure 5.37(b) the same plot of is presented for spectra of MUSIC.
Statistically, more power is evaluated slightly after the LOS component. Therefore, the mean of the estimated result typically appears to be after the LOS component, and we receive a positive bias.

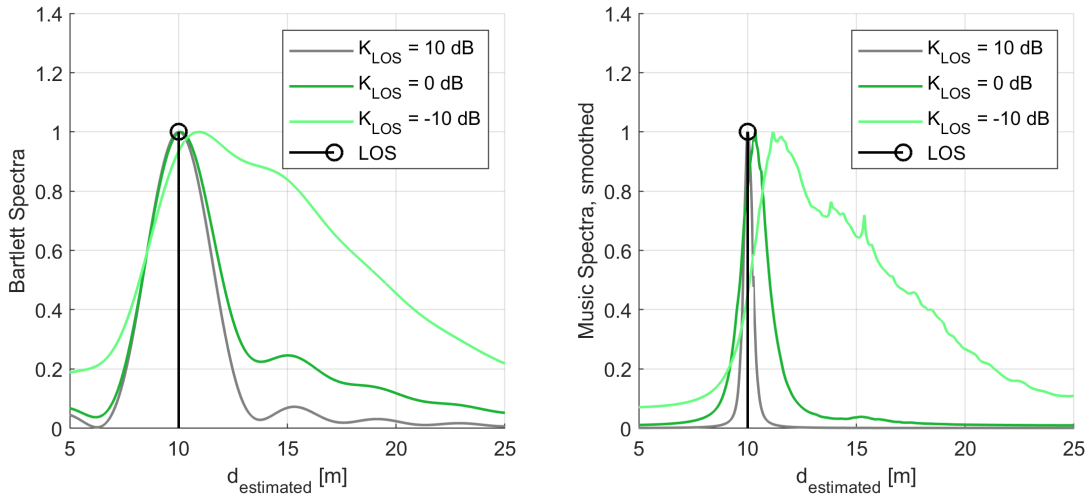

(a) Bartlett spectra, averaged (b) MUSIC spectra, averaged

Figure 5.38: LOS component with DM, $N_R = 10000$

We plot the statistically evaluated spectra in figure 5.38(a) and figure 5.38(b), and observe a bias as well, systematically occuring for the double exponential model.

Lastly, we view the bias and the standard deviation in dependency of the SNR in figure 5.39 and 5.40. In each subfigure, a different K_{LOS} factor is considered.
We clearly observe a stronger bias for lower K_{LOS} factors. The comparison of a K_{LOS} factor of -10, 0 and 10, further shows that the standard deviation increases as well for a small K_{LOS}.

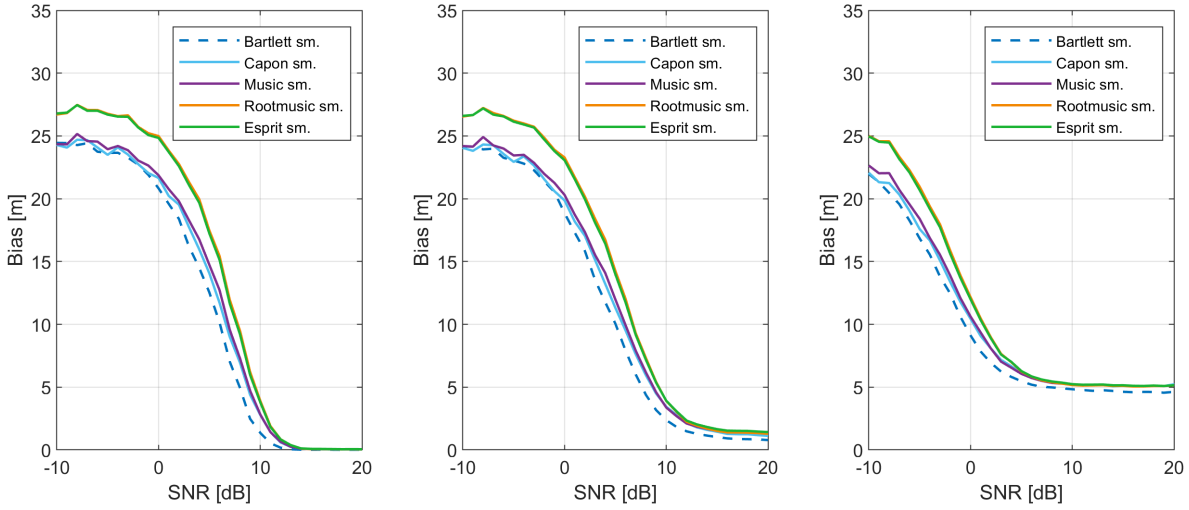

(a) $K_{\mathrm{LOS}} = 10dB$ (b) $K_{\mathrm{LOS}} = 0dB$ (c) $K_{\mathrm{LOS}} = -10dB$

Figure 5.39: Bias, with DM

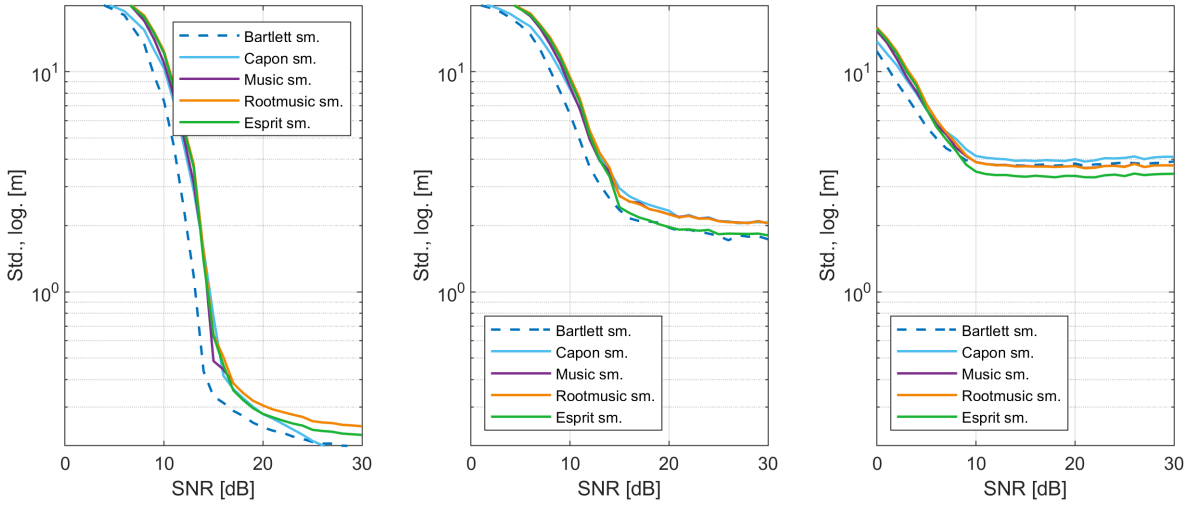

(a) $K_{\mathrm{LOS}} = 10dB$ (b) $K_{\mathrm{LOS}} = 0dB$ (c) $K_{\mathrm{LOS}} = -10dB$

Figure 5.40: Standard deviation, with DM

6

Testing with measurements

For practical evaluation, measurements of a vector network analyzer (VNA) were used. With VNA measurements, a reliable and consistent dataset of channel impulse responses (CIRs) could be provided. The dataset was used as input and applied on the implemented estimation algorithms.

The measurements setup was as follows: A fixed antenna and a moving antenna were used, with the moving antenna placed at 20 different positions. Antenna 1 was defined to be the stationary sender antenna while antenna 2, the receiver antenna, was moved for each measurement. Both antennas were placed in a height of 1 m. The measurements were done for various distances, with antenna 2 moving along a car on a grid spaced in 0.5 m positions. The car was placed at the x-axis of the defined grid with the aim to evaluate the reflections caused by the vehicle. We consider a LOS scenario with a direct view between antenna 1 and antenna 2, and with reflections of lower gain than the LOS component. The measurement setup is illustrated in figure 6.1.

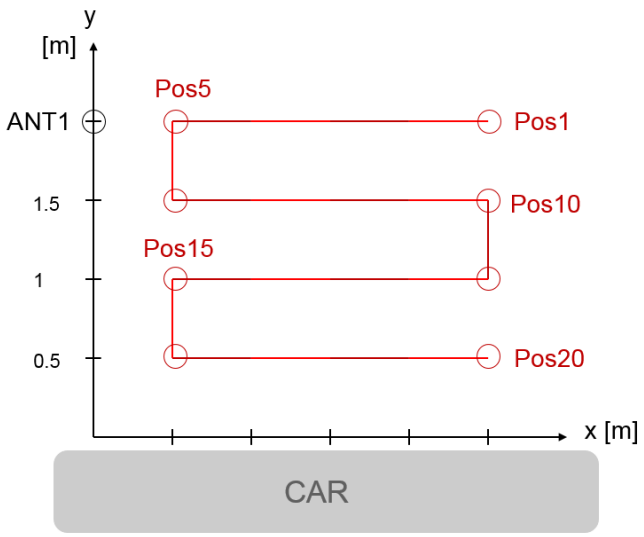

Figure 6.1: Measurement setup

It is important to note that the measurement parameters are different than the parameters used for the simulation.
For the evaluation, the full specifications of the VNA are utilized for the purpose of demonstration of the potential abilities of the estimation methods. Hence the full VNA bandwidth of 409.6 MHz was used. The parameters of the VNA measurements are stated in table 6.1.
However, a further evaluation approach will be discussed in section 6.2. In section 6.2, the bandwidth is reduced to provide consistency with the problem statement and the BT standard.

Parameters	Symbol	Parameters
Bandwidth	B_0	409.6 MHz
Minimum frequency	f_{min}	2.2 GHz
Maximum frequency	f_{max}	2.6096 GHz
Number of frequencies	K	8192
Frequency step	Δf	50 KHz

Table 6.1: Specifications of the VNA ZNB20 (Rohde & Schwarz)

6.1 Evaluation using full VNA specifications

For the evaluation, the number of measurements can be reduced to save computional power. A frequency step Δf of 50 KHz leads to a maximum distance of $\sim$ 5996 m, as

$$d_{max} = \frac{c}{\Delta f} \approx 5996\text{m}, \tag{6.1}$$

which is far from the signal components that we analyze, occuring at distances probably smaller than 10 m. For a comparison of the methods, we choose a number of frequencies $K = 512$ instead, still resolving a maximum distance of $\sim$ 374.7 m.
The parameters of the first evaluation approach are stated in table 6.2.

Parameters	Symbol	Evaluation 1
Bandwidth	B_0	409.6 MHz
Minimum frequency	f_{min}	2.2 GHz
Maximum frequency	f_{max}	2.6096 GHz
Number of frequencies	K	512
Frequency step	Δf	800 KHz
Smoothing factor	K_s	250

Table 6.2: Parameters used for the evaluation of the VNA measurements

The results gained by the different estimation methods are plotted and compared to the true distance of the LOS component.
Additionally, the reflective components are determined as well. The distance corresponding to each reflection was computed analytically using geometric considerations.
We consider two relectors: The car, but also garage floor causes reflections, resulting in a number of five analytically determined reflections in total. The reflection paths are described below:

- First-order reflections
  - Antenna 1 $\rightarrow$ garage floor $\rightarrow$ antenna 2
  - Antenna 1 $\rightarrow$ car $\rightarrow$ antenna 2

- Second-order reflections
  - Antenna 1 → garage floor → car → antenna 2
  - Antenna 1 → car → garage floor → antenna 2
- Third-order reflections
  - Antenna 1 → garage floor → car → garage floor → antenna 2

6.1.1 Positions 1 and 5

For a first evaluation attempt, position 1 and position 5 are chosen. Both positions share the property of the car being positioned in a large distance compared to other measurement positions. This leads to longer time delays and to larger distance between the signal components. Considering position 1, the distance between the antennas to be estimated equals 2.5 m. In contrast, both antennas are close to each other in a distance of 0.5 m considering position 5. However, reflective components have a comparably long path, since the car is positioned in a large distance.

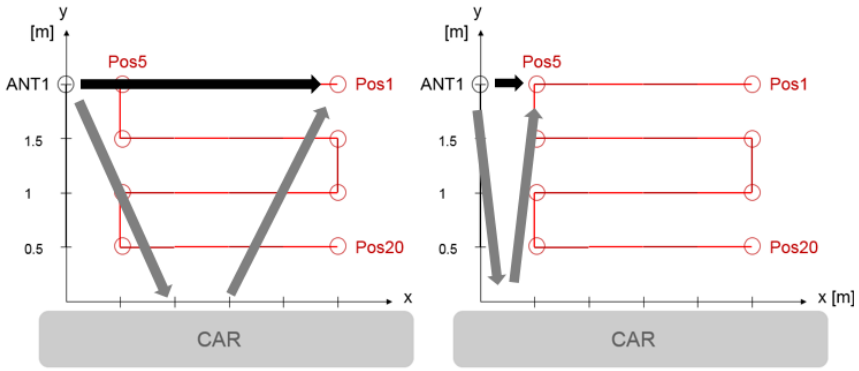

Figure 6.2: Direct path and reflection in position 1 (left) and position 5 (right)

The results of applying estimation algorithms to our measurement data of position 1 and position 5 is plotted in figure 6.3 and figure 6.4.

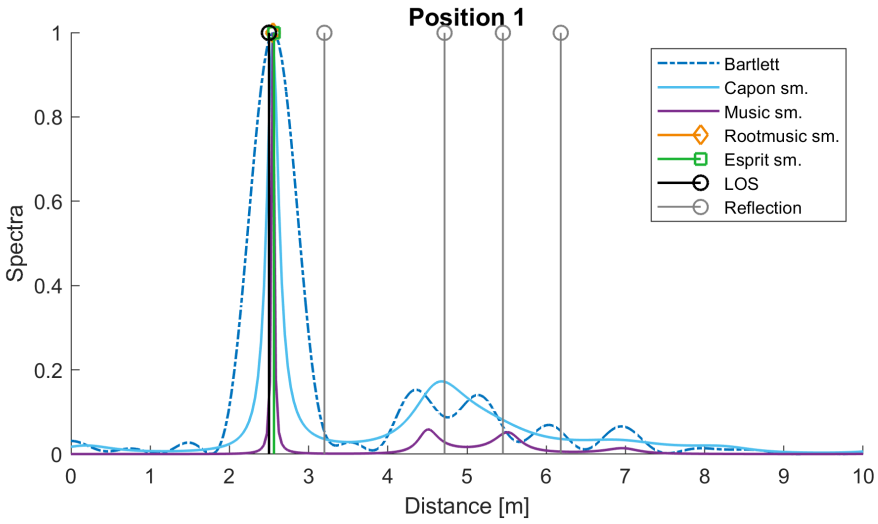

Figure 6.3: Estimation result of position 1

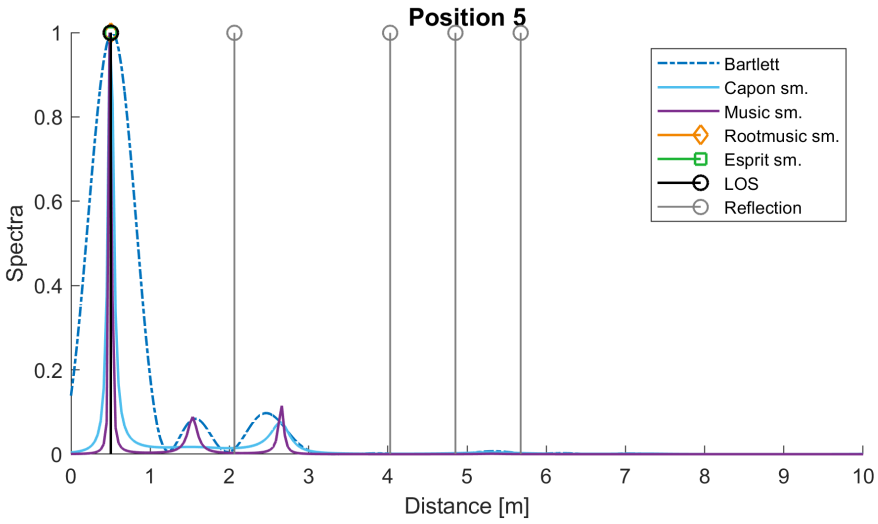

Figure 6.4: Estimation result of position 5

Note that, when connecting the antennas, there was an additional propagation delay from the SMA connectors through the antennas. This additional delay accounted for a discrepancy between true distance and the peak of LOS of 30 cm. It was considered as an offset in the evaluation of the estimation methods.

The larger bandwidth of 409.6 MHz results in a narrower main lobe considering beamforming approaches, in contrast to simulation results in chapter 5. It allows a better separation of the signal components compared to the lower bandwidth used before.
In figure 6.3 we see, that the Bartlett spectrum forms separate beams corresponding to the reflective components. In figure 6.4 the reflective components are further apart from the LOS component, and they are not visible in the spectra.
Furthermore, the results in table 6.3 show a bias of about 0.05 m for each considered estimation method for position 1. The bias is caused by the first reflection, which occurs in a comparably small distance to the LOS component. For position 5, we observe a bias of only 0.01 to 0.02 m in table 6.3.

True distance	Position 1 2.5 m	Position 5 0.5 m
Estimated distance Bartlett	2.5486 m	0.5246 m
Estimated distance Capon	2.5486 m	0.4871 m
Estimated distance MUSIC	2.5486 m	0.4871 m
Estimated distance Root-MUSIC	2.5485 m	0.5004 m
Estimated distance ESPRIT	2.5589 m	0.4988 m

Table 6.3: Estimation results from position 1 and position 5

6.1.2 Positions 16 and 20

In contrast, position 16 and 20 are positions in a small distance to the car, and reflections occur closely-spaced. The estimation results of both positions are plotted in the figures 6.5 to 6.8. For a better overview, beamforming and model-based methods and are plotted separately.

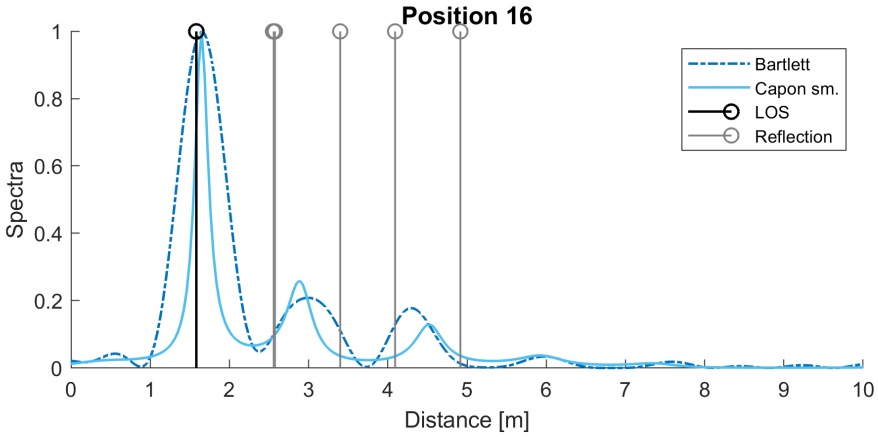

Figure 6.5: Bartlett and Capon, evaluated for position 16

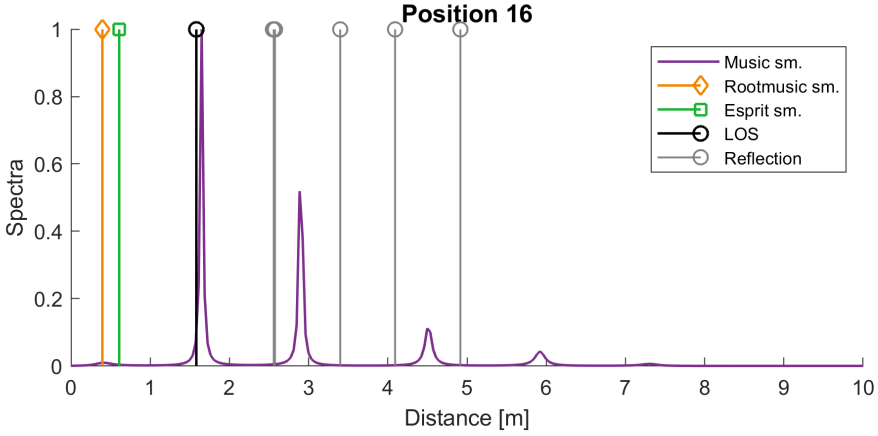

Figure 6.6: MUSIC, Root-MUSIC and ESPRIT, position 16

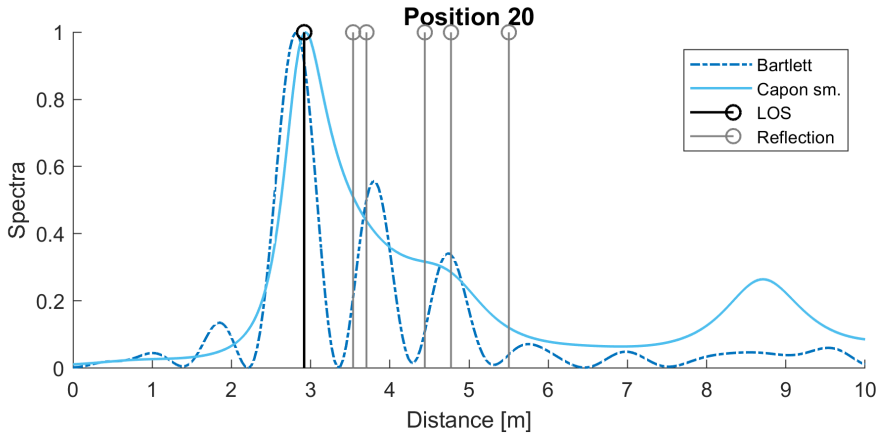

Figure 6.7: Bartlett and Capon, evaluated for position 20

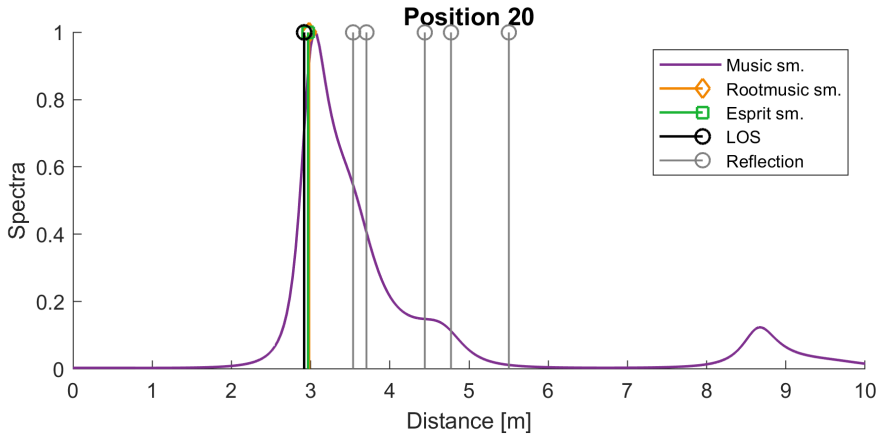

Figure 6.8: MUSIC, Root-MUSIC and ESPRIT, position 20

In figure 6.5, we observe satisfying results considering the spectra of both beamforming approaches. However, the parametric methods in figure 6.6 fail to estimate the LOS components in position 16. A large bias is observed for Root-MUSIC and ESPRIT, however, also MUSIC detects a peak in the pseudospectrum at 0.7121 m. This is seen from the estimation results in table 6.4.
In this case, the estimation error is caused by the impact of the chosen model order, and will be discussed in the following section.

Estimation method	Estimation result	True distance	Estimation error
Bartlett	1.5490 m	1.5811 m	0.0679 m
Capon	1.5490 m	1.5811 m	0.3079 m
MUSIC	0.4121 m	1.5811 m	-1.169 m
Root-MUSIC	0.3968 m	1.5811 m	-1.1843 m
ESPRIT	0.6057 m	1.5811 m	-0.9754 m

Table 6.4: Estimation results of position 16

At position 20, we observe a particularly small estimation error for the Capon method, for Root-MUSIC and ESPRIT.

Additionally, we observe side lobes before the LOS component in the Bartlett spectrum, at about 1.312 m and 2.136 m.
However, the peak finding technique introduced in section 5.5.1 is applied, and both side lobes are ignored, as their gain does not exceed the threshold. Since the second side lobe is rather dominant with an amplitude being 13.51 % of the main lobe, we can conclude a satisfying performance of the peak finding approach.
The estimation results are summed up in table 6.5.

Estimation method	Estimation result	True distance	Estimation error
Bartlett	2.8110 m	2.9155 m	-0.1045 m
Capon	2.9234 m	2.9155 m	0.0079 m
MUSIC	3.0359 m	2.9155 m	0.1204 m
Root-MUSIC	2.9811 m	2.9155 m	0.0656 m
ESPRIT	2.9708 m	2.9155 m	0.0553 m

Table 6.5: Estimation results of position 20

6.1.3 The choice of the model order

For the evaluation of model-based approaches, the model order must be chosen. Considering the number of 5 analytically determined reflections in section 6.1, we gain a number of $M = 6$ signal components with the LOS component.
Therefore, a model order of 6 is chosen. However, for position 1 and position 5, the second-order reflections appear to be equal, so that $d_4 = d_5$.

	LOS component	1st order reflections		2nd order reflections		3rd order refl.
Pos.	d_1	d_2	d_3	d_4	d_5	d_6
1	2.5 m	3.2 m	4.72 m	5.45 m	5.45 m	6.18 m
5	0.5 m	2.06 m	4.03 m	4.86 m	4.86 m	5.68 m
16	1.58 m	2.55 m	2.57 m	3.4 m	4.09 m	4.92 m
20	2.92 m	3.54 m	3.70 m	4.44 m	4.77 m	5.5m

Table 6.6: Analytically determined signal components

Position	Chosen Model order
1	5
5	5
16	6
20	6

Table 6.7: Chosen Model order

Since $d_4 = d_5$ for position 1 and 5, a model order of 5 was chosen for the evaluations of both positions. Considering position 16, the first two reflections d_2 and d_3 are appearently very similar, which might be the reason for the biased results for all model-based methods in figure 6.6, also listed in table 6.4. For the evaluation of position 16 and 20, a model order of 6 was chosen. However, as the model order is unknown in real life situations, we wish to evaluate different choices of the model orders.
Indeed, model-based methods often result in a large estimation error if a wrong model order is chosen. For instance, a model order of 5 is chosen for position 1 in figure 6.3. However, increasing the model order to 6 and 7 already results in a large bias. This is seen in the figures 6.9 to figure 6.11, where the results for a chosen model order of 5, 6 and 7 are plotted.

Chosen model order	True distance	Estimated distance		
		MUSIC	Root-MUSIC	ESPRIT
5	2.5 m	2.5486 m	2.5485 m	2.5589 m
6	2.5 m	0.4873 m	0.504 m	1.9854 m
7	2.5 m	0.5247 m	0.5088 m	0.6356 m

Table 6.8: Estimation results of position 1 depending on the choice of the model order

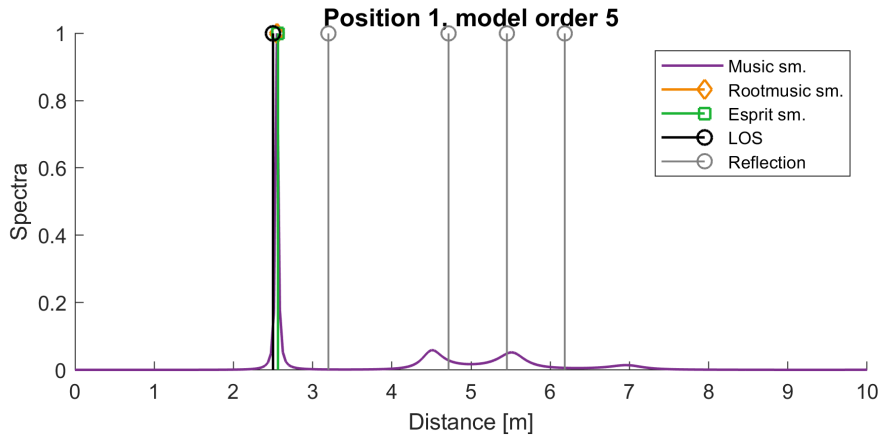

Figure 6.9: Estimation result of position 1, with a chosen model order of 5

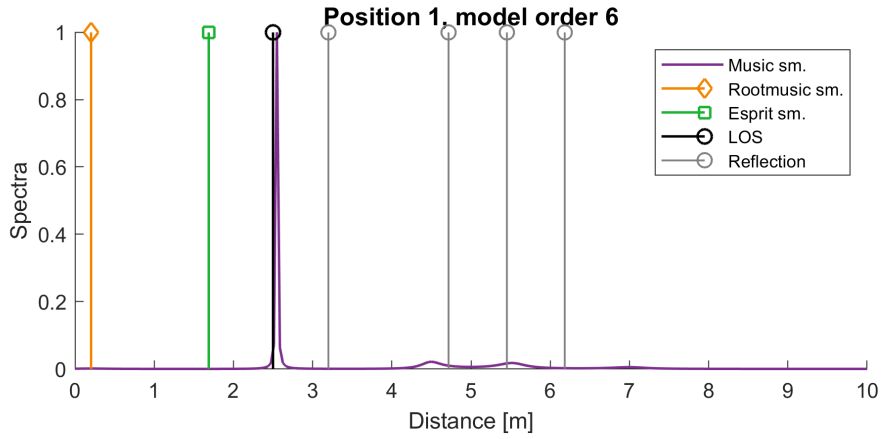

Figure 6.10: Estimation result of position 1, with a chosen model order of 6

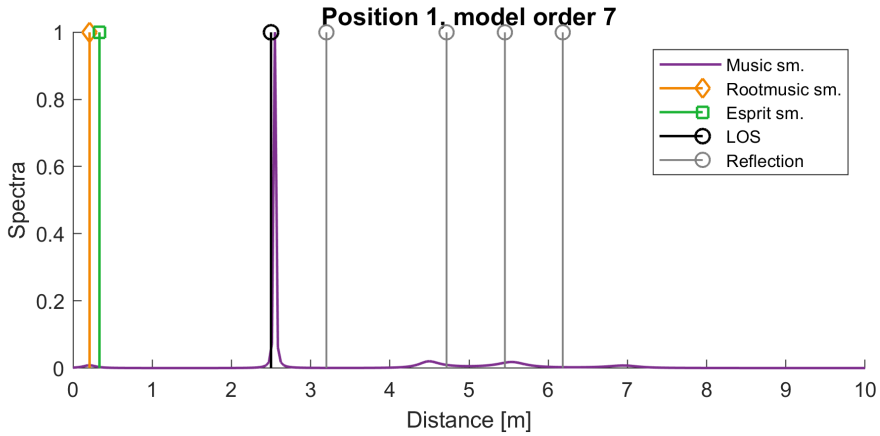

Figure 6.11: Estimation result of position 1, with a chosen model order of 7

6.1.4 Estimation error in dependency of the model order

For a better insight, the estimation error of model-based methods is evaluated in dependency of the chosen model order.
In figure 6.12 the estimation error $\widehat{e}_{d_1}$

$$\widehat{e}_{d_1} = \mathbb{E}\left[\widehat{d_1} - d_1\right] \tag{6.2}$$

is plotted as a function of the model order for the positions 1, 16 and 20. The model order is chosen from 1 to 19.

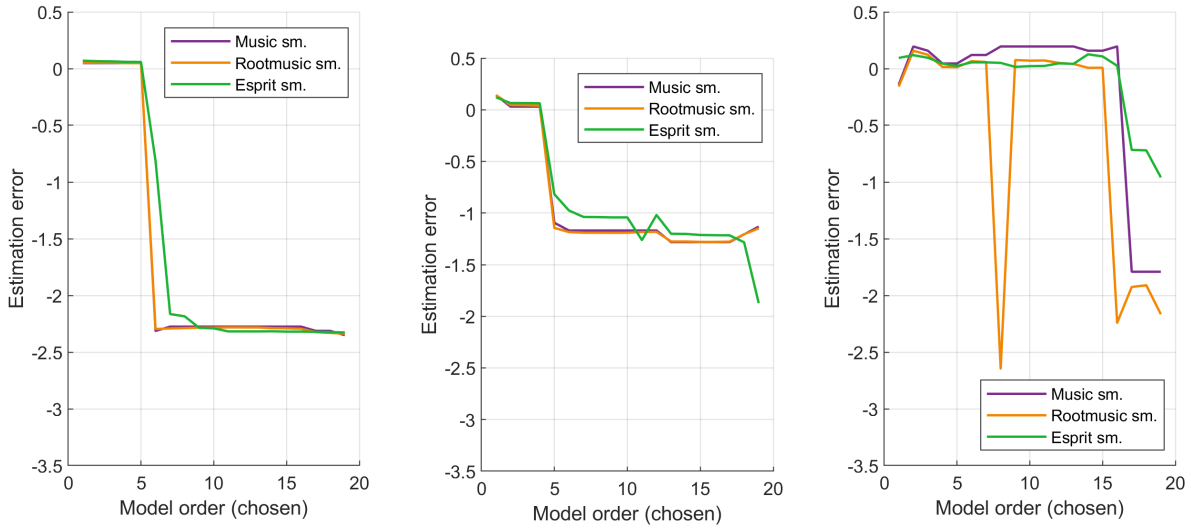

(a) Position 1 (b) Position 16 (c) Position 20

Figure 6.12: Bias of MUSIC, Root-MUSIC and ESPRIT

In the figures 6.13(a) to 6.13(c), the estimation error is evaluated for all 20 positions. We wish to find out, whether a trend can be observed for different choices of the model order. For each model-based method, MUSIC, Root-MUSIC and ESPRIT, the 20 positions are presented

together in a plot as a function of the model order.
In figure 6.13(d), the estimation error is further averaged over the 20 evaluated positions with the aim to compare the three model-based approaches to each other.

In figure 6.13(d), we clearly observe the smallest error for each method for model orders ≤ 5. However, in the figures 6.13(a) to 6.13(c) we also see that the estimation error for various model orders and different positions fluctuates strongly between 0.2 m and about -2.5 m. Slightly less fluctuations are observed for the MUSIC method.

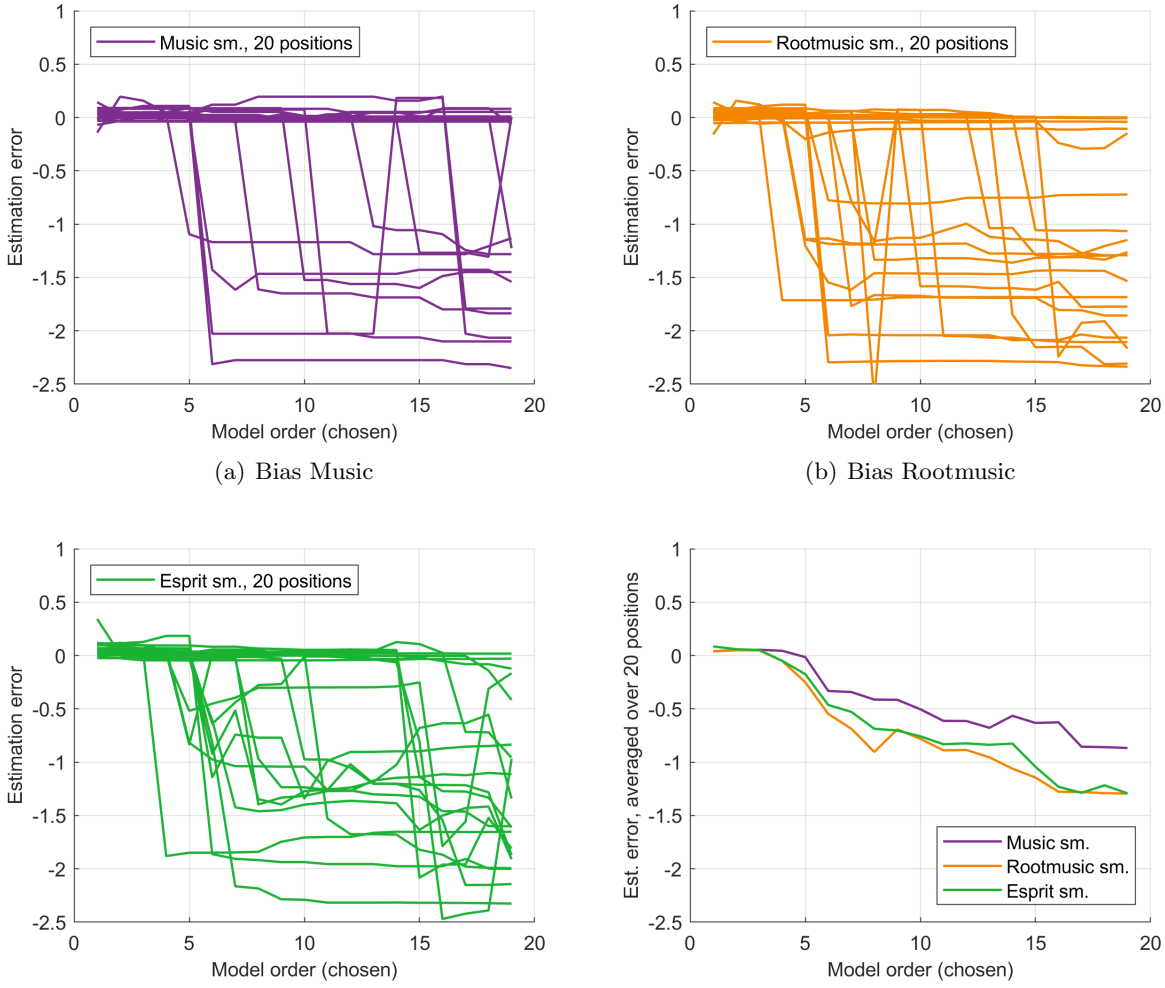

(a) Bias Music

(b) Bias Rootmusic

(c) Bias Esprit

(d) Bias averaged over 20 positions

Figure 6.13: Bias for 20 position for each method (a) - (c) and averaged over 20 positions (d)

6.2 Evaluation using BT specifications

Another evaluation approach is to use specifications equal to the simulations in chapter 5 to gain results corresponding to the BT standard and hence provide consistency with the problem statement.
Therefore, the VNA measurement data is sampled at a lower sampling rate, so that the bandwidth and the number of frequencies K correspond to the parameters of the simulation in chapter 5. However, downsampling resulted in a bandwidth of 78.0096 MHz, and K is reduced to 40.

Parameters	Symbol	Evaluation 2
Bandwidth	B_0	78.0096 MHz
Frequency range	f_{min} - f_{max}	2.3658 GHz - 2.4438 GHz
Number of frequencies	K	40
Frequency step	Δf	1.95024 MHz
Smoothing factor	Ls	20

Table 6.9: Parameters used for evaluation of the measurements using BT specifications

We clearly observe the impact of the reduced bandwidth in figure 6.14.
This can be seen specifically when looking at spectrum-forming methods. The main lobe of the Bartlett spectrum is formed much broader, compared to the plots in section 6.1.
Hence the ability to separate closely-spaced signal components is very limited, reflective components are not clearly resolved in the spectra of Bartlett, Capon or MUSIC.
In the figures 6.14(a) to 6.14(d), the results of position 1, 5, 16 an 20 are plotted with the same model orders as stated in table 6.7.

Considering the model-based methods, we compare the result of the estimation error evaluated in dependency of various model orders. In figure 6.15, we observe strong fluctuations, as also seen in section 6.1.
Furthermore, for the reduced bandwith corresponding to the BT standard we note that fluctuations of the error occur already for model orders ≤ 5.

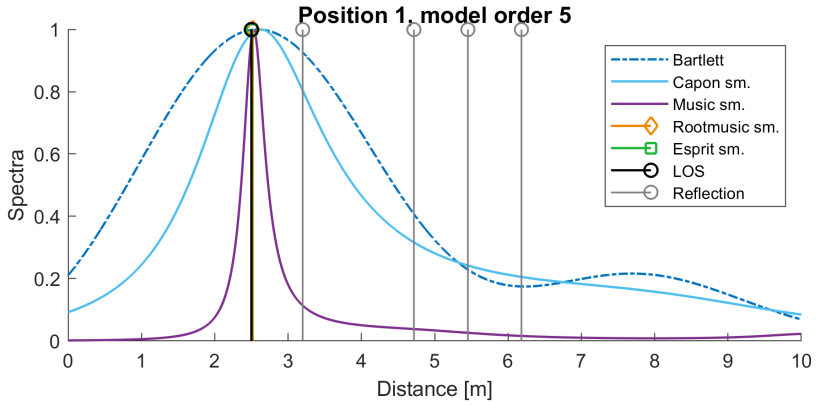

(a) Position 1

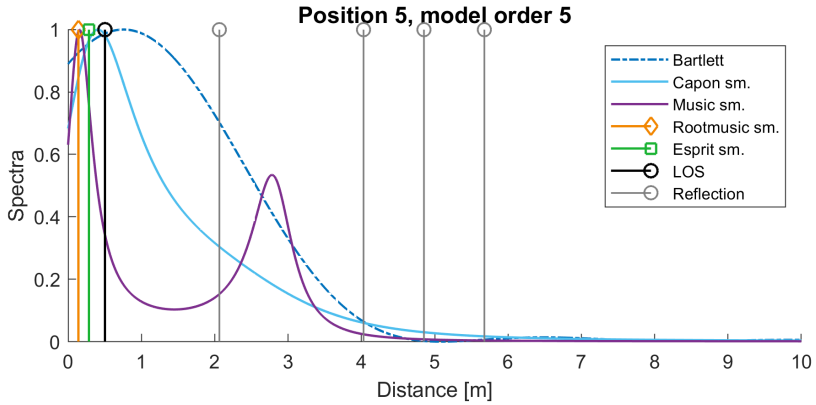

(b) Position 5

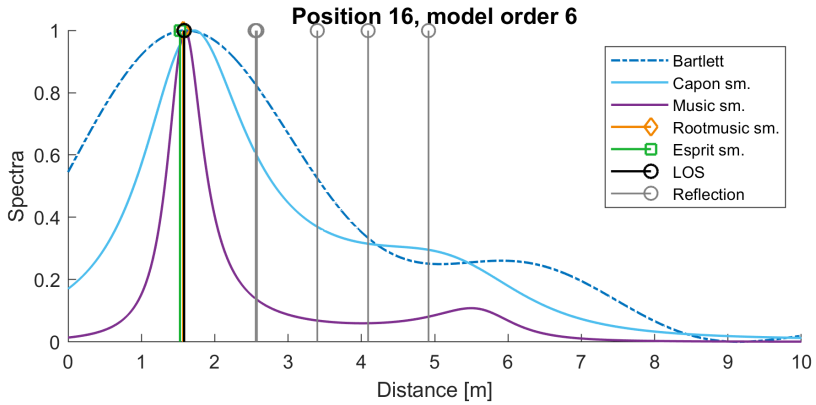

(c) Position 16

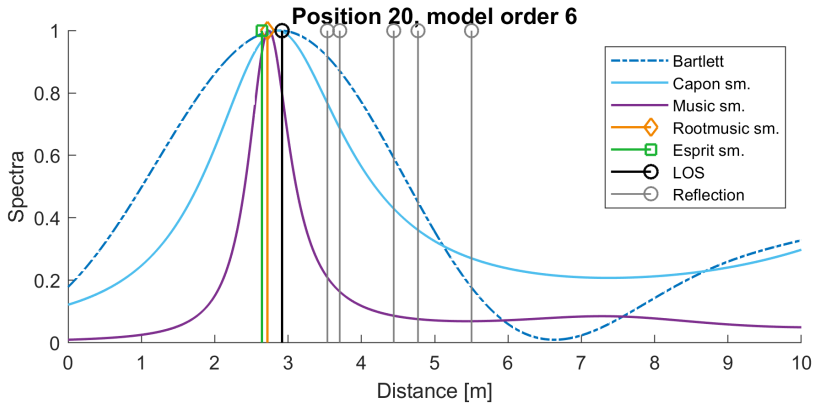

(d) Position 20

Figure 6.14: Estimation results for a bandwidth $B_0 = 78.0096MHz$

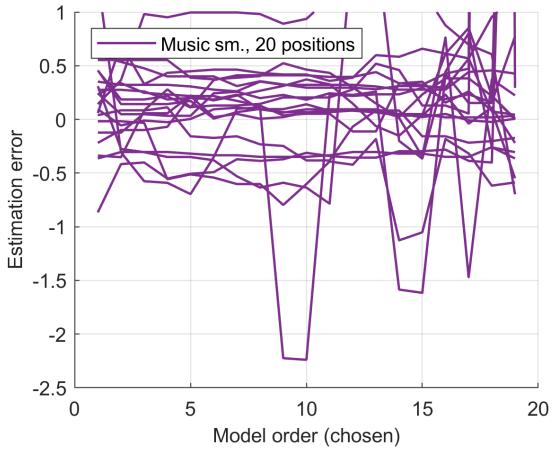

(a) Bias Music

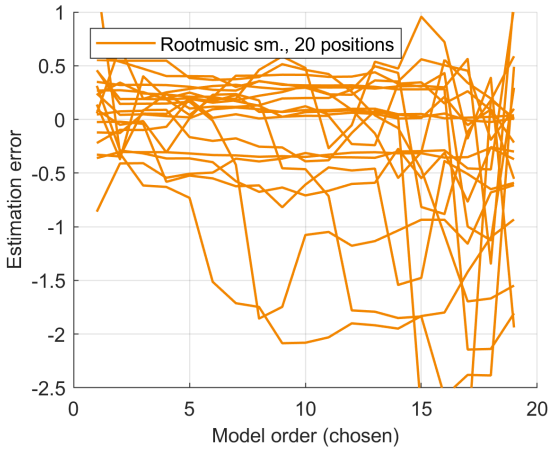

(b) Bias Rootmusic

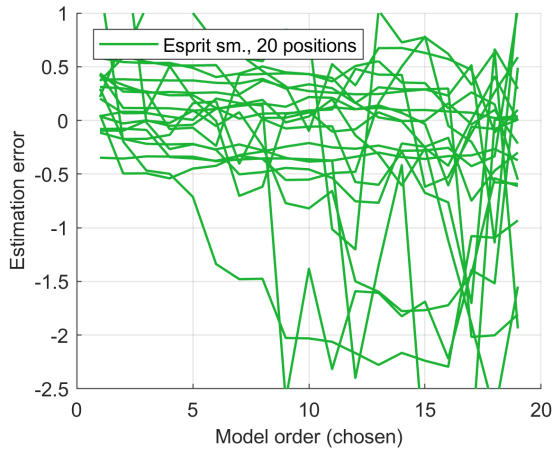

(c) Bias Esprit

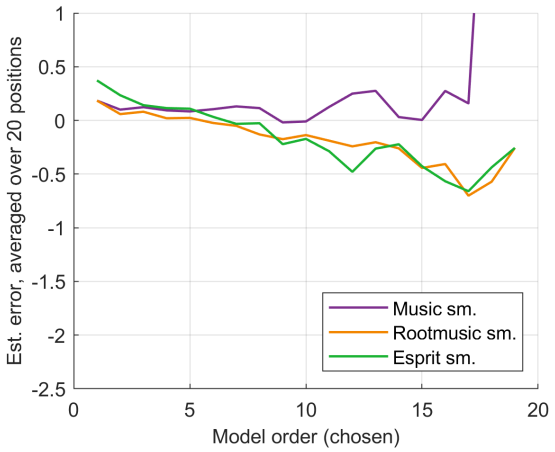

(d) Bias averaged over 20 positions

Figure 6.15: Bias for 20 position for each method (a) - (c) and averaged over 20 positions (d)

7

Conclusion and Outlook

In this thesis, carrier phase-based ranging is evaluated considering range estimation methods known from the field of array signal processing. The aim lies in comparing their applicability specifically given consideration to BT as a potential RF technology. Spectral-based as well as parametric estimation methods are tested in particular simulation scenarios and further validated with VNA measurements.
Primarily, the methods are validated by simulations and compared in terms of different parameters and scenarios of various channel properties. The latter are f.e. reflective components and their distance to the LOS component, or an attenuation gain of the LOS component. Among others, the one-component case, a LOS scenario with a reflective multipath component, an NLOS scenario with an attenuated LOS component, and a DM scenario are discussed.

Several impairments are found to cause substantial limitations of carrier phase-based ranging, significantly so when considering the BT standard.
In spectral-based approaches, such as the Bartlett and the Capon beamformer, the bandwidth remarkably influences the estimation results as soon as MPCs are considered. An impact that is found in the broadness of the main lobe, where broader main lobes emerge from smaller bandwidths.
The BT bandwidth of 78 MHz proved insufficient for the aim of accurate ranging. Since a broad main lobe hinders a spectral-based method to separate closely-spaced signal components, reflections become a noticeable challenge for the Bartlett and the Capon beamformer.
Since signal components superimpose with each other, observations proved that estimation results appear to be biased for components occurring in larger distances of 3 m from each other when applying the Capon method (see figure 5.30). The Bartlett spectrum has a broader main lobe and remains biased for even larger distances $d_{\Delta 12}$.
An important point to note is that smoothing should not be applied for the Bartlett beamformer, since it reduces the bandwidth and expands the main lobe even further. The Capon beamformer necessitates smoothing for $N = 1$, and the choice of the smoothing factor requires consideration. An appropriately smoothed array size K_s was empirically found to be 1/2 to 5/8 of the original array size K in section 5.3.4.

In model-based methods, the MUSIC method shows a similar tendency to closely-spaced signal components. The narrow main lobe of the pseudospectrum and MUSIC's ability to suppress noise in the pseudospectrum prove unbiasedness on average for the MUSIC method for distances between signal components as small as 2.5 m. However, note that this is a large distance in terms of accurate ranging considering various reflections of the surrounding, yet Root-MUSIC and ESPRIT outperform MUSIC, and seem to remain unbiased up to 1.3 m in figure 5.30.

Besides the bandwidth, another system parameter which requires attention due to the possibility of a leakage, is the distance step size Δd. For the true distance must accord with the grid of spectral-based methods or leakage can occur, it is important to aim for a sufficiently small step size. Even though model-based methods avoid the effect, interpolation is another

approach which helps to increase the sample rate for beamformers as well (see section 5.2.1.1). The parameter K, which illustrates the number of narrow-band frequency measurements, does not impact the distance step size nor the beam size.

However, it is not only the broadness of the main lobe, but also the side lobes that tend to complicate the estimation for spectral-based methods. Superposition with noise can especially lead to inadvertent beams in the spectrum. Particularly for low SNR, dominant side lobes tend to falsify estimation results. Considering the mentioned impairments of the system parameters, beamforming methods are most limited in their applicability.

Considering attenuation and scenarios like that of the backpocket case in section 5.5, requires us to search for the first peak instead of the maximum peak, and implementing a peak searching approach becomes essential for Bartlett and Capon, as well as for the MUSIC method. The MUSIC method worked best in cases of low LOS gains. Since MUSIC is a sub-spaced approach and works by splitting the covariance matrix into a signal and noise subspace, the method benefits from suppressing the noise in its pseudospectrum. Unlike the Bartlett method, where the Bartlett spectrum shows side lobes naturally for band-limited functions, as this method corresponds to a squared Fourier transform.
Both Bartlett and Capon algorithm often reveal dominant side lobes in their spectrum dependent on the SNR; something that makes it rather difficult to employ a peak finding technique that differentiates an attenuated LOS component from strong side lobes.

The observations accomplished using these simulations are rated dependent on their performance for different SNR values. To obtain reliable estimation results, it is desirable to find a method which is unbiased for a low SNR, and ideally shows a low standard deviation. Note that for this validation, there exemplarily was a 2 m distance between signal components chosen in section 5.3. However, the model order was chosen correctly for the purpose of simulation, whereas in real life situations the model order is unknown.
It was observed that the Bartlett beamformer remains biased even for a high SNR as it is simply fails to separate the signal components, but also the Capon method is found unbiased only for SNR values higher than 45 dB. MUSIC performs better and becomes unbiased for an SNR of about 37 dB. Note that an SNR of 37 dB is still rather high considering hardware implementation. Root-MUSIC and ESPRIT are already found unbiased for an SNR of 29 dB, assuming the model order was chosen correctly.
The ML estimator performs best and gains unbiased results at SNR values as low as 26 dB. Note that the ML estimator is used as a reference here, as its grid-based implementation utilized in this work is not applicable in hardware. Since this thesis aims at comparing estimations methods, it is desirable to avoid influences from optimization algorithms and thus focus on grid-based evaluation. However, considering the ML estimator, grid-based evaluation is found computationally not feasible for two or more signal components. Nevertheless, for further analyses, it is indeed reasonable to evaluate the ML estimator with an emphasis on approaches considering optimization algorithms or sampling methods [13].
Taking into consideration the standard deviation, the before mentioned rating was confirmed. The standard deviation of the Bartlett beamformer reaches a certain point of 0.76 m in figure 5.25 and does not improve with increasing SNR values. Under the parametric methods, we see that ESPRIT shows a slightly lower standard deviation than Root-MUSIC and MUSIC.

The evaluation of estimation methods using simulation has shown that model-based methods have noteworthy advantages. Their main benefit is their ability to achieve better ranging accuracy by leveraging the intrinsic structure of the covariance matrix. However, an evaluation of the considered estimation approaches using VNA measurements in section 6.1.3 unveils the importance of a suitable choice of the model order.

Observations in chapter 6 prove that a model order chosen slightly too high can cause a large estimation error for MUSIC, Root-MUSIC and ESPRIT. An evaluation of 20 measurement positions reveal a high fluctuation of the estimation error, depending on the choice of the model order. The results in figure 6.13 and 6.15 point to the necessity to consider further optimization algorithms for the estimation of the model order [13], [14], [15, p. 225], as to enable a robust performance of model-based estimation methods.

8 Appendix and Bibliography

8.1 Acronyms

PKES Passive Keyless Entry and Start

RF radio frequency

BT Bluetooth

IFT Inverser Fourier Transform

FT Fourier transform

IDFT Inverse Discrete Fourier Transformation

CW continuous-wave

ToF time of flight

AWGN Additive White Gaussian Noise

AWCGN additive white circular-symmetric complex Gaussian noise

CIR channel impulse response

CIRs channel impulse responses

VNA vector network analyzer

CRLB Cramer-Rao lower bound

LOS Line-of-sight

ML maximum-likelihood

MPCs multi path components

MPC multi path component

SNR Signal-To-Noise Ratio

SPSC Signal Processing and Speech Communications Laboratory

DPS Delay Power Spectrum

PDP Power Delay Profile

DM Diffuse Multipath

Bibliography

[1] T. J. Waraksa, K. D. Fraley, R. E. Kiefer, D. G. Douglas, and G. L. H., "Passive keyless entry system," *US Patent*, no. 4942393, 07 1990.

[2] H. Krim and M. Viberg, "Two decades of array signal processing," *IEEE Signal Processing Magazin*, 07 1996.

[3] A. Bensky, *Wireless Positioning Technologies and Applications, Second Edition*. 685 Canton Street, Norwood, MA: Artech House, 2016.

[4] M. R. J. and R. A. Bishel, "A two-frequency radar for vehicle automatic lateral control," *IEEE Transactions on Vehicular Technology*, vol. 31, no. 1, pp. 32–39, 02 1982.

[5] D. H. Johnson and D. E. Dudgeon, *Array Signal Processing: Concepts and Techniques*. Prentice Hall, 02 1993.

[6] C. W. Therrien, *Discrete Random Signals and Statistical Signal Processing*. Englewood Cliffs, NJ, USA: Prentice-Hall, Inc., 1992.

[7] S. M. Kay, *Fundamentals of Statistical Signal Processing: Estimation Theory*. Prentice Hall, 1993, vol. 1.

[8] P. Stoica and R. Moses, *Spectral Analyses of Signals*. Upper Saddle River, NJ, USA: Prentice Hall, 2005.

[9] J. G. Proakis and M. Salehi, *Communication Systems Engineering, Second Edition*. Upper Saddle River, NJ, USA: Prentice-Hall, Inc., 2002.

[10] "Symmetry pattern of a persymmetric 5x5 matrix," https://commons.wikimedia.org/wiki/File:Matrix_symmetry_qtl2.svg, 05 2014, accessed: 2020-05-15.

[11] J. Karedal, S. Wyne, P. Almers, F. Tufvesson, and A. Molisch, "A measurement-based statistical model for industrial ultra-wideband channels," *IEEE Trans. Wireless Commun.*, vol. 6, no. 8, 08 2007.

[12] T. Wilding, S. Grebien, U. Mühlmann, and K. Witrisal, "Accuracy bounds for array-based positioning in dense multipath channels," *Sensors*, vol. 18, no. 12, 2018.

[13] N. Arkind and B. Nadler, "Parametric joint detection-estimation of the number of sources in array processing," 12 2009.

[14] B. Nadler and L. Kontorovich, "Model selection for sinusoids in noise: Statistical analysis and a new penalty term," *IEEE Transactions on Signal Processing*, vol. 20, no. 20, 05 2011.

[15] S. M. Kay, *Fundamentals of Statistical Signal Processing: Detection Theory*. Prentice Hall, 1998, vol. 2.

[16] M. H. Hayes, *Statistical Digital Signal Processing and Modeling*. John Wiley and Sons, Inc., 1996.

[17] M. Woolley, "Bluetooth direction finding," *IEEE Wireless Communications and Networking Conference (WCNC)*, 03 2019.

[18] P. Zand, J. Romme, J. Govers, F. Pasveer, and G. Dolmans, "A high-accuracy phase-based ranging solution with bluetooth low energy (ble)," *IEEE Wireless Communications and*

Networking Conference (WCNC), 2019.

[19] T.-J. Shan, M. Wax, and T. Kailath, "On spatial smoothing for direction-of-arrival estimation of coherent signals," *IEEE Transactions on Acoustics, Speech, and Signal Processing*, vol. ASSP-33, no. 4, 08 1985.

[20] D. Dardari, A. Conti, U. Ferner, A. Giorgetti, and M. Z. Win, "Ranging with ultrawide bandwidth signals in multipath environments," *Proceedings of the IEEE*, vol. 97, no. 2, 02 2009.

[21] A. F. Molisch, *Wireless Communications*. Wiley - IEEE, 11 2010.